Cosmogenic Radioisotopes in the Double Chooz Far Detector

Dissertation

der Mathematisch-Naturwissenschaftlichen Fakultät
der Eberhard Karls Universität Tübingen
zur Erlangung des Grades eines Doktors
der Naturwissenschaften
(Dr. rer. nat.)

vorgelegt von
Lee Francis Fedor Stokes
geboren in Athen/Griechenland

Tübingen
2015

Gedruckt mit Genehmigung der Mathematisch-Naturwissenschaftlichen Fakultät der Eberhard Karls Universität Tübingen.

Tag der mündlichen Qualifikation:	23. 10. 2015
Dekan:	Prof. Dr. Wolfgang Rosenstiel
1. Berichterstatter:	Prof. Dr. Tobias Lachenmaier
2. Berichterstatter:	Prof. Dr. Josef Jochum

Abstract

This thesis reports the first yield measurements of cosmogenic radioisotopes produced in the Double Chooz far detector.
Double Chooz is a reactor anti-neutrino experiment whose principle purpose is the measurement of the neutrino oscillation parameter $\sin^2(2\theta_{13})$. The far detector is perfectly located to observe an anti-neutrino deficit due to oscillation. A deficit is observed for two samples of inverse beta decay interactions where the delayed neutron is captured on either Gd or H. The latter is less sensitive to $\sin^2(2\theta_{13})$ but provides a threefold increase in statistics. Novel background reduction techniques have seen the signal to background ratio increase by a factor of ten for the H channel. One of the remaining backgrounds imitates the inverse beta decay signal through its double coincidence. This is the cosmogenic β-n emitter whose contamination in the inverse beta decay sample is explained in detail. Its measurment is important as it dominates the background uncertainty budget and methods increasing its precision are explained.
The β-n emitters are a sub-sample of ^{9}Li and ^{8}He decays which are not the only cosmogenically produced radioisotopes in the Double Chooz far detector. Cosmic muons which pass through the detector create hadronic and electromagnetic showers which interact predominantly with ^{12}C atoms present in the organic liquid scintillator to produce many others. An introduction into the cosmogenic radioisotopes produced is given along with the yield measurements of ^{12}B, ^{12}N, ^{9}Li, ^{8}He, ^{8}B and ^{8}Li. Complementary measurements have been published by KamLAND and Borexino at their detector depths of 2700 m.w.e and 3800 m.w.e respectively. The comparably shallow overburden at the Double Chooz far detector of 300 m.w.e gives a handle on the relationship between the depth and corresponding cosmogenic yield. The three yield measurements of each cosmogenic radioisotope are fitted with $Y = Y_0\langle E_\mu\rangle^\alpha$, where the mean muon energy $\langle E_\mu\rangle$ is used instead of the depth, to estimate the power law exponent α for four radioisotopes. This is the first multi-experiment determination of α using liquid scintillators. The α measurement for ^{9}Li, one of the β-n emitters, will allow the estimation of this important background for current and future experiments at other depths.

Zusammenfassung

In dieser Dissertation werden die ersten Messungen der Ausbeute von Radioisotopen, welche im Double Chooz Ferndetektor durch Myonen induziert wurden, berichtet.
Die Hauptaufgabe des Double Chooz Reaktor-Antineutrino Experimentes besteht darin den Mischungswinkel θ_{13} zu messen. Der Ferndetektor befindet sich dazu im optimalen Abstand um das durch die Neutrinooszillationen verursachte Defizit an Antineutrinos zu beobachten. Bei den inversen Betazerfällen wird ein Defizit gemessen, wobei das Neutron entweder am Gadolinium oder Wasserstoff eingefangen wird. Der Einfang an Wasserstoff bietet weniger Sensitivität auf den gesuchten Parameter $\sin^2(2\theta_{13})$, liefert däfur aber eine dreifach höhere Statistik. Neue Techniken zur Untergrundreduktion ermöglichten eine Verbesserung das Signal zu Untergrund-Verhältnis für den Wasserstoff-Kanal um einen Faktor zehn. Myon-induzierte β-n-Emitter imitieren das Signal des inversen Betazerfalls jedoch durch eine doppelte Koinzidenz. Dieser Arbeit beschreibt Messung sowie Methoden zur genauen Bestimmung des Anteils dieser Ereignisse, da die β-n-Emitter den grössten Beitrag zur Unsicherheit über den Untergrund darstellen.
Bei den β-n-Emitter handelt es sich um eine Untergruppe der ^{9}Li und ^{8}He-Zerfälle. Weitere Myon-induzierte Radioisotope im Double Chooz Ferndetektor werden durch Kosmische Myonen erzeugt. Diese passieren den Detektor und erzeugen hadronische und elektromagnetische Schauer, welche hauptsächlich mit den ^{12}C Atomen reagieren welche sich im organischen, flüssigen Szintillator befinden.
Es wird eine Übersicht über die Produktion der kosmischen Radioisotope und die dazugehörigen, gemessenen Ausbeuten an ^{12}B, ^{12}N, ^{9}Li, ^{8}He, ^{8}B, ^{8}Li gegeben, sowie über komplementäre Messungen die von der KamLAND sowie Borexino Kollaboration veröffentlicht wurden. Diese wurden in einer Tiefe von 2700 m.w.e bzw 3800 m.w.e durchgeführt. Die relativ kleine Abschirmung vom 300 m.w.e des Double Chooz Ferndetektors erlaubt es einen Zusammenhang zwischen der Tiefe und der dazugehörigen Abschirmung der Ausbeute herzustellen. Die drei Messungen der Ausbeute für jedes kosmogene Radioisotop wurden mit $Y = Y_0\langle E_\mu\rangle^\alpha$ gefittet, wobei die mittlere Myon-Energie anstelle der Tiefe verwendet wurde, um den Exponenten α für vier Radioisotope zu evaluieren. Hierbei handelt es sich um die erste Analyse, unter Verwendung der Daten von

mehreren Experimenten, des α-Parameters mit Hilfe von Flüssigszintillatoren. Die Bestimmung des α-Parameters für ^{9}Li, einem der β-n-Emitter, wird die Determinierung dieses wichtigen Untergrundbeitrags für laufende und zukünftige Experimente in anderen Tiefen ermöglichen.

Table of contents

List of figures

List of tables

Nomenclature

Acronyms / Abbreviations

ANN Artificial Neural Network

BG Background

BML Binned Maximum Likelihood

COM Center of Mass

CU Charge Units

CV Central Value

DC Double Chooz

EDF Électricité de France

EP Entry Point

FEE Front End Electronics

FN Fast Neutron

FV Fiducial Volume

GC Gamma Catcher

Gd Gadolinium

H Hydrogen

HV High Voltage

IBD Inverse Beta Decay

ID Inner Detector

IP Impact Parameter

IV Inner Veto

IVV Inner Vessel Veto

LDP Lateral Distance Profile

LN Light Noise

LNL Light Non-Linearity

ly Light Yield

MC Monte Carlo

NT Neutrino Target

OV Outer Veto

PE Photoelectron

PMNS Pontecorvo-Maki-Nakagava-Sakata

PMT Photomultiplier Tube

PS Pulse Shape

QNL Charge Non-Linearity

RMS Root Mean Square

RoSS Readout System Simulation

RRM Reactor Rate Modulation

SM Stopping Muon

TB Trigger Board

TMB Trigger Master Board

XP Exit Point

Part I

Neutrino Physics and Detection

Chapter 1

Neutrino Oscillations

1.1 A Brief History of Neutrino Oscillations

The idea of a neutrino was first proposed in 1930 by Wolfgang Pauli in a letter [1] to Geigner and Meitner who were participating in a nuclear conference in Tübingen [2]. His search for an "electrically neutral" particle with spin 1/2, which he originally labelled a neutron, was his desperate attempt to understand the lack of momentum conservation in β-decays.
In 1946 Bruno Pontecorvo proposed the detection of neutrinos using Inverse Beta Decay (IBD) [3]:

$$\overline{\nu} + p \rightarrow e^{+} + n \tag{1.1}$$

This technique was used in 1956 by Reines and Cowan [4] to observe neutrinos[1] for the first time using a liquid scintillator target and reactor anti-neutrinos. Since then neutrinos were found to have many intriguing properties. In 1957 it was found that parity was violated in the weak interaction [5] and one year later it was shown by Goldhaber that neutrinos are left handed particles [6]. Although Pontecorvo had already proposed the idea of oscillations, it wasn't until the discovery of two types of neutrinos, ν_e and ν_μ in 1962 [7] that led him to write a paper describing neutrino oscillation between the two. In the same paper, Pontecorvo mentions the implications that this would have on the solar neutrino flux, where neutrino oscillation would result in a deficit of ν_e's compared to those produced when taking the inverse square law into account. This was later shown in the Davis Jr. solar neutrino experiment using IBD on tetrachloroethylene C_2Cl_4 as follows [8]:

$$\nu + {}^{37}\mathrm{Cl} \rightarrow e^{-} + {}^{37}\mathrm{Ar} \tag{1.2}$$

[1] At this time it wasn't known that there existed anti-neutrinos as well as neutrinos.

where this radio-chemical technique was first proposed by Pontecorvo in 1946. The Davis Jr. experiment reported a deficit of roughly two thirds of the number of ν_e's predicted by the Standard Solar Model (SSM), which was at the time referred to as the "solar neutrino problem". The solar neutrino problem was confirmed first by the Kamiokande-II experiment in 1989, using neutrino-elastic scattering [9] and later by the GALLEX [10] and SAGE [11] experiments, both detecting neutrinos by IBD on ^{71}Ga as follows:

$$\nu + {}^{71}\mathrm{Ga} \rightarrow e^- + {}^{71}\mathrm{Ge} \tag{1.3}$$

The first evidence of neutrino oscillations from observation of atmospheric neutrinos was from the Super-Kamiokande experiment in 1998 [12]. The existence of the ν_τ by the DONUT collaboration [13] in 2001 confirmed the three lepton flavour families. Since then further evidence for neutrino oscillations has been confirmed by reactor experiments Double Chooz (DC) [14], Daya Bay [15] and RENO [16]; accelerator beams K2K [17], MINOS [18], T2K [19]; solar neutrinos from SNO [20] and Borexino [21].

1.2 Theory of Neutrino Oscillations

In the standard model there are three neutrinos ν_l where $l = e, \mu, \tau$. They have so far only been observed interacting through the three flavour states $|\nu_l\rangle$ via the weak interaction. The evidence for neutrino oscillations described in Section 1.1 implies that they have non-zero mass and that the flavour states are in fact mixtures of the mass states $|\nu_i\rangle$ where $i = 1,2,3$ with mass m_i. The flavour states are related to the mass states as follows[2]:

$$|\nu_l\rangle = \sum_{i=1}^{3} U_{li} |\nu_i\rangle \tag{1.4}$$

where U is the unitary 3×3 Pontecorvo-Maki-Nakagava-Sakata (PMNS) matrix separated according to the three rotations as follows:

$$U_{li} = \begin{pmatrix} 1 & 0 & 0 \\ 0 & \cos\theta_{23} & \sin\theta_{23} \\ 0 & -\sin\theta_{23} & \cos\theta_{23} \end{pmatrix} \cdot \begin{pmatrix} \cos\theta_{13} & 0 & \sin\theta_{13} e^{-i\delta} \\ 0 & 1 & 0 \\ -\sin\theta_{13} e^{i\delta} & 0 & \cos\theta_{13} \end{pmatrix} \cdot \begin{pmatrix} \cos\theta_{12} & \sin\theta_{12} & 0 \\ -\sin\theta_{12} & \cos\theta_{12} & 0 \\ 0 & 0 & 1 \end{pmatrix} \tag{1.5}$$

It is composed of three mixing angles θ_{23}, θ_{13} and θ_{12} and a CP violating phase δ, describing the case in which the neutrino is a Dirac particle. If the neutrino is in fact a

[2]The theory behind neutrino oscillations is taken from [2] and [22]

Majorana particle where it is its own anti-particle, the PMNS matrix is modified as follows:

$$U_{li}^{M} = U_{li} e^{i\alpha_i/2} \tag{1.6}$$

where $\alpha_1 = 0$, and α_2 and α_3 are the Majorana phases which have no impact on neutrino oscillations. The probability of detecting a neutrino in the flavour state $|\nu_{l'}\rangle$ after having been produced in the flavour state $|\nu_l\rangle$ is given by:

$$P(\nu_l \to \nu_{l'}) = |A(\nu_l \to \nu_{l'})|^2 = |\sum_{i=1}^{3} U_{l'i} D_i U_{li}^*|^2 \tag{1.7}$$

where $D_i = e^{-iE_i t}$ describes the propagation of ν_i between the source and the detection point and U_{li}^* and $U_{l'i}$ are the amplitudes of finding ν_i in the initial and final flavour state respectively. Equation 1.7 can be expanded to give:

$$P(\nu_l \to \nu_{l'}) = \sum_{i,j} U_{l'i}^* U_{l'j} e^{-i(E_i - E_j)t} U_{l,i} U_{l'j}^* \tag{1.8}$$

Assuming ultra-relativistic neutrinos the substitution $(E_i - E_j)t = \Delta m_{ij}^2 L/2E$ can be made into Equation 1.8 to give:

$$P(\nu_l \to \nu_{l'}) = \sum_{i,j} U_{l'i}^* U_{l'j} e^{-i\frac{\Delta m_{ij}^2 L}{2E}} U_{l,i} U_{l'j}^* \tag{1.9}$$

where $\Delta m_{ij}^2 = m_i^2 - m_j^2$ is the mass squared difference. Expanding Equation 1.9 gives [23]:

$$\begin{aligned} P(\nu_l \to \nu_{l'}) = \delta_{ll'} & \\ & - 4 \sum_{j>i} \Re(U_{l'i}^* U_{l'j} U_{l,i} U_{l'j}^*) \sin^2\left(\frac{\Delta m_{ij}^2 L}{4E}\right) \\ & + 2 \sum_{j>i} \Im(U_{l'i}^* U_{l'j} U_{l,i} U_{l'j}^*) \sin\left(\frac{\Delta m_{ij}^2 L}{2E}\right) \end{aligned} \tag{1.10}$$

$$\tag{1.11}$$

which allows the evaluation of the neutrino oscillation probability between any two flavours after travelling a distance of L from their origin. For anti-neutrinos the oscillation probability is the same except that the sign of the last term changes to become negative. It is clear that if the masses are the same or zero, there will be no oscillation between the flavour states as the second and third terms will vanish and the first term will be one when $l' = l$. Oscillation

probabilities for the channel $l \neq l'$ are called transition probabilities whilst those where $l = l'$ are called survival probabilities. Experiments searching for oscillations where $l = l'$ are called disappearance experiments as they search for a deficit of neutrinos due to oscillation, whilst experiments where $l \neq l'$ are called appearance experiments as they search for an appearance of $\nu_{l'}$ due to oscillation. It is worthwhile noting that although the mass squared difference can be estimated using the oscillation length, it is not possible to get a handle on the individual masses themselves. There are three mass squared difference terms, two of which have similar values and the third which is much larger such that $\Delta m^2_{12} \ll (\Delta m^2_{31} \simeq \Delta m^2_{32})$. Current neutrino experiments are not able to distinguish between the mass order, where $m_1 < m_2 < m_3$ is labelled the Normal Order (NO) and $m_3 < m_1 < m_2$ is the Inverted Order (IO).

A global fit to the experimental results currently available gives the mixing angles, mass squared differences and CP violating phase for both NO and IO as summarised in Table 1.1.

Table 1.1 Neutrino oscillation parameters from a global fit of all experiments. This includes the mixing angles, mass squared differences and delta phase for both NO and IO. The uncertainties give the $\pm 1\sigma$ range and the values are taken from [24]. These results contain the experimental results from the Neutrino 2014 Conference.

Parameter	NO	IO
$\Delta m^2_{21}\ 10^{-5}\,\mathrm{eV}^2$	$7.6^{+0.19}_{-0.18}$	
$\Delta m^2_{31}\ 10^{-3}\,\mathrm{eV}^2$	$2.48^{+0.05}_{-0.07}$	$2.38^{+0.05}_{-0.06}$
$\sin^2\theta_{12}$ ($\theta_{12}\,^\circ$)	0.323 ± 0.016 (34.6 ± 1.0)	
$\sin^2\theta_{23}$ ($\theta_{23}\,^\circ$)	$0.567^{+0.032}_{-0.124}$ ($48.9^{+1.8}_{-7.2}$)	$0.573^{+0.025}_{-0.039}$ ($49.2^{+1.5}_{-2.3}$)
$\sin^2\theta_{13}$ ($\theta_{13}\,^\circ$)	0.226 ± 0.012 ($8.6^{+0.3}_{-0.2}$)	0.229 ± 0.012 (8.7 ± 0.2)
δ/π	$1.41^{+0.55}_{-0.40}$	1.48 ± 0.31

1.3 Measuring θ_{13}

The best way to measure the mixing angle θ_{13} is by observing the disappearance of $\overline{\nu}_e$'s. They are generated in copious amounts, on the order of $10^{20}\,\overline{\nu}_e\,\mathrm{s}^{-1}\,\mathrm{GW}_{\mathrm{th}}^{-1}$ by nuclear reactors which undergo nuclear fission and then β-decay. The survival probability for $\overline{\nu}_e$ is

evaluated using Equation 1.10 to give:

$$\begin{aligned} P(\overline{\nu}_e \to \overline{\nu}_e) = 1 &- 4\cos^2\theta_{12}\cos^2\theta_{13}\sin^2\theta_{13}\sin^2\left(\frac{\Delta m^2_{31}L}{4E}\right) \\ &- 4\sin^2\theta_{12}\cos^2\theta_{13}\sin^2\theta_{13}\sin^2\left(\frac{\Delta m^2_{32}L}{4E}\right) \\ &- 4\cos^2\theta_{12}\cos^2\theta_{13}\sin^2\theta_{12}\cos^2\theta_{13}\sin^2\left(\frac{\Delta m^2_{21}L}{4E}\right) \end{aligned} \tag{1.12}$$

This can be simplified by placing a detector designed to measure θ_{13} close enough to the source that the last term can be neglected, as the oscillation length due to Δm^2_{21} is much larger than from Δm^2_{31}. By making the substitution:

$$\sin^2\left(\frac{\Delta m^2_{ee}L}{4E}\right) \equiv \sin^2\theta_{12}\sin^2\left(\frac{\Delta m^2_{31}L}{4E}\right) + \cos^2\theta_{12}\sin^2\left(\frac{\Delta m^2_{32}L}{4E}\right) \tag{1.13}$$

into Equation 1.12 and re-arranging gives the two flavour oscillation probability:

$$P(\overline{\nu}_e \to \overline{\nu}_e) \cong 1 - \sin^2(2\theta_{13})\sin^2\left(\frac{\Delta m^2_{ee}L}{4E}\right) \tag{1.14}$$

Figure 1.1 shows the $\overline{\nu}_e$ survival probability described by Equation 1.12 with the substitution from Equation 1.13. A neutrino energy of 3 MeV is assumed and the other mixing parameters are taken from Table 1.1, except $\Delta m^2_{ee} = 2.44 \times 10^{-3}\,\text{eV}^2$ which is taken from [14]. The blue line corresponds to $\theta_{13} = 0$ and the red line to $\theta_{13} = 8.6^\circ$. Two oscillation lengths are visible, a long one corresponding to Δm^2_{21} and a shorter one corresponding to the comparatively larger Δm^2_{ee}. The shorter oscillation length is used to measure $\sin^2(\theta_{13})$, which Equation 1.14 shows us governs the amplitude of the oscillation. To measure the mixing angle θ_{13}, the ideal location for a detector to observe the largest deficit of $\overline{\nu}_e$'s is at the first minimum, corresponding to roughly 1 km. To measure a deficit, an experiment would need to know the un-oscillated amount as a comparison. There are two ways in which this can be done, the first predicts the amount of $\overline{\nu}_e$'s by modelling the reactor cores and their fuel composition over time. The second method relies on a second detector, located much closer to the source where there is minimum oscillation. The corresponding measured rate or spectrum can be used as a comparison.

The primary search for θ_{13} was done by the CHOOZ experiment which ran in 1997 and was the predecessor of the Double Chooz (DC) experiment. The detector site and location can be

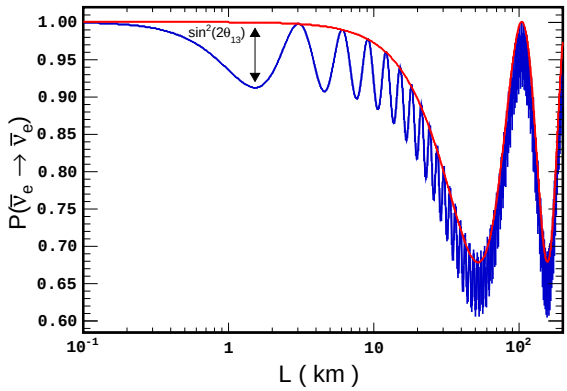

Figure 1.1 The $\overline{\nu}_e$ survival probability described by Equation 1.12 with the substitution from Equation 1.13. The blue line shows the survival probability when θ_{13} is set to zero, the red line shows the probability when θ_{13} is non-zero. The first minimum is the ideal location for a detector to measure the deficit of $\overline{\nu}_e$'s. The neutrino oscillation parameters have been taken from Table 1.1, $\Delta m^2_{ee} = 2.44 \times 10^{-3}\,\text{eV}^2$ is taken from [14] and an average neutrino energy of 3 MeV is assumed.

seen in Figure 1.2a, which is in fact the same site used by the DC far detector. Two twin pressurised-water (PWR) reactors at a distance of roughly 1 km were used as the sources of $\overline{\nu}_e$'s. The CHOOZ experiment contained a 5 ton target filled with 0.09 % Gd-loaded liquid scintillator. The target is contained in an intermediate 17 ton region equipped with 192 eight inch PMTs and finally an optically separate cosmic muon veto equipped with 48 PMTs [25]. A degradation in the transparency of the Gd-loaded liquid scintillator limited the amount of time the experiment could run for to four months. The CHOOZ experiment found no oscillation, and a paper published in 2003 improved the limit to $\sin^2(2\theta_{13}) < 0.1$ for larger values of the mass squared difference, Figure 1.2b shows the exclusion contour plot [26].

The Palo Verde experiment located at the Palo Verde Nuclear Generating Station in Arizona ran from 1998 recording 350 days of $\overline{\nu}_e$ interactions [27]. It detected $\overline{\nu}_e$'s produced by three identical reactors, two of which were located 890 m from the detector and one at 750 m. It also used a Gd-loaded scintillator but contained in 66 acrylic cells. The Palo Verde experiment came to the same conclusion as CHOOZ and found no evidence for neutrino oscillation, setting a limit of $\sin^2(2\theta_{13}) < 0.17$ for $\Delta m^2 > 1.1 \times 10^{-3}\,\text{eV}^2$.

Accelerator experiments are also capable of measuring the θ_{13} mixing angle. These long baseline experiments produce beams of ν_μ and search for the appearance of ν_e. This is trickier than in the case of reactor experiments as the oscillation probability requires knowledge of all the mixing parameters including the unknown phase δ. After CHOOZ and Palo Verde, the T2K accelerator experiment showed hints of a non-zero value of θ_{13} in 2011

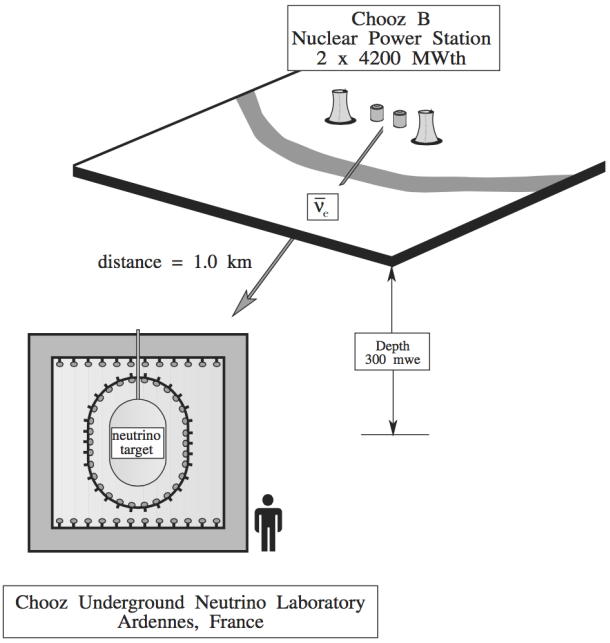

(a) The experimental site of the CHOOZ experiment including the nuclear power station and detector's location and design schematic.

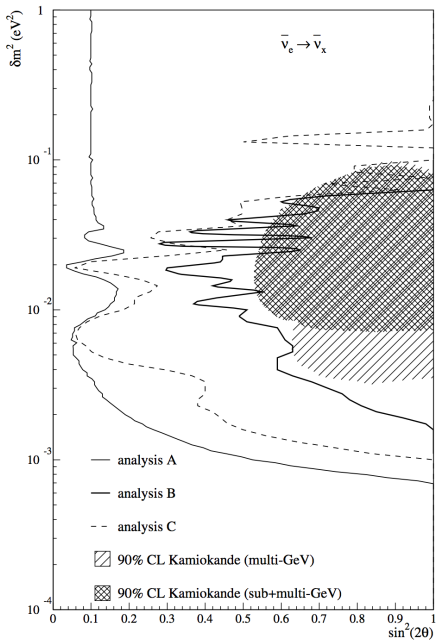

(b) The 90 % exclusion contours from the CHOOZ experiment, which set a limit of roughly $\sin^2(2\theta_{13}) < 0.1$ for a large mass squared difference.

Figure 1.2 The detector site and exclusion plot from the CHOOZ experiment. Source [26].

[28]. A neutrino beam produced at J-PARC was directed 2.5° off-axis to the Super Kamiokande detector located 295 km away. T2K observed six ν_e candidates which is equivalent to a $2.5\,\sigma$ significance over the $\theta_{13} = 0$ hypothesis, where 1.5 ± 0.3 events would be expected. At the end of 2011 DC also reported an indication of $\overline{\nu}_e$ disappearance [29, 30]. After 101 days of running the far detector reported an observed to predicted $\overline{\nu}_e$ ratio of 0.944 ± 0.043. An analysis of both the rate and energy spectrum of the prompt positrons from the IBD reactions gave a measurement of $\sin^2(2\theta_{13}) = 0.086 \pm 0.051$. More information about DC and the latest results are discussed in Chapters 2 and 3.

Finally, further to DC there are two other reactor experiments measuring θ_{13}, Daya Bay and RENO. They both exploit multi-site detectors to cancel systematic uncertainties. The detector and reactor layout of each can be seen in Figure 1.3. All three experiments have a similar design concept in regards to the detectors, where each detector is made of four concentric vessels, starting with a Gd-loaded scintillator target at the centre, a scintillator filled gamma catcher, a buffer containing the PMTs and an optically separated cosmic muon detector. DC is the only experiment to use a liquid scintillator in the muon detector, RENO

and Daya Bay both use a water Čerenkov detector instead. Daya Bay has to date the best

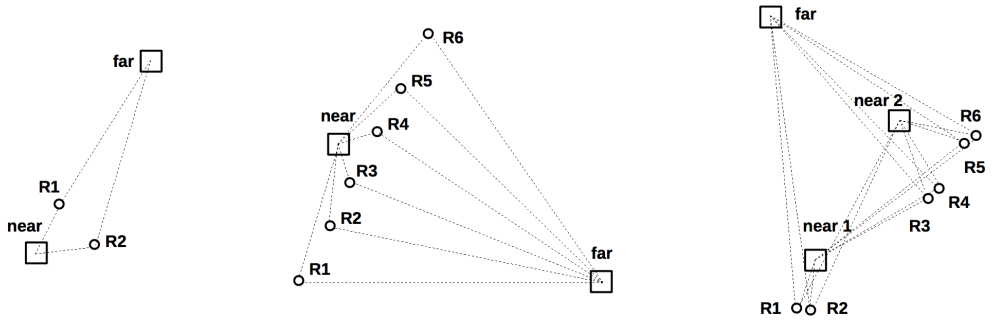

Figure 1.3 The detector (squares) and reactor (circles) layout of the Double Chooz (left), RENO (center) and Daya Bay (right) experiments. The dotted lines correspond to the baselines between reactors and detectors. Source [31].

measurement of $\sin^2(2\theta_{13})$, using six detectors and six $2.9\,\mathrm{GW_{th}}$ reactors, Daya Bay measured $\sin^2(2\theta_{13}) = 0.084 \pm 0.005$ [32]. RENO (Reactor Experiment for Neutrino Oscillation) is located in South Korea, and has two detectors and six reactors. Their best measurement is $\sin^2(2\theta_{13}) = 0.087 \pm 0.011$ [33].

Chapter 2

The Double Chooz Experiment

The Double Chooz (DC) Experiment was proposed in [34] using an improved double detector design described in [35]. It is located in the North of France, close to the border with Belgium and exploits two nuclear reactor cores as sources of $\overline{\nu}_e$'s. It is the successor to the Chooz Experiment [25, 26] which ran in the 90's and placed an upper limit of $\sin^2(2\theta_{13}) < 0.1$ for $\Delta m^2_{\text{CHOOZ}} > 2 \times 10^{-3}\,\text{eV}^2$.
This chapter gives an overview of the Double Chooz detectors along with an explanation of each part. The information is taken from [36, 37].

2.1 Detection Technique

Anti-neutrinos are detected in DC when they interact with free protons in the the detector through IBD. The anti-neutrino and proton interact through the weak force to produce a positron and neutron as follows:

$$\overline{\nu}_e + p \rightarrow e^+ + n \tag{2.1}$$

The positron is observed first and as such is labelled the prompt event. The energy it deposits is equal to its kinetic energy and two 511 keV gammas from its annihilation with an electron. It gives a window to the energy of the neutrino $E_{\overline{\nu}_e}$ through the following relationship:

$$E_{e^+} = \frac{1}{2}\left(\sqrt{m_n^2 - 4m_p\left(-E_{\overline{\nu}_e} + \Delta + \frac{\Delta^2 - m_e^2}{2m_p}\right)} - m_n\right) \tag{2.2}$$

where m_e and E_{e^+} are the positron mass and energy, m_n and m_p are the neutron and proton mass respectively and $\Delta = m_n - m_p$. The neutron needs to thermalise through scattering

before its capture is observed and is often called the delayed event. The main IBD channel is through neutron capture on Gadolinium (Gd) due its high cross section. This capture occurs on one of two possible isotopes releasing an average of four γ's whose sum energy is approximately 8 MeV. The average capture time on Gd is 30 µs. Neutron capture also occurs on Hydrogen releasing a γ with an energy of 2.22 MeV after an average time of 200 µs. This channel has been used in addition to the Gadolinium channel to measure $\sin^2(2\theta_{13})$ in DC.

2.2 Double Chooz Site

In the north of France, the village of Chooz lends its name to the site of a nuclear power station operated by EDF (Électricité de France). The Centrale nucléaire de Chooz has two N4 type reactors called B1 and B2 of which both are capable of producing 4.25 GW of thermal power. After nuclear fission takes place in the reactor cores the fission fragments undergo β^- decay to stabilise. It is the large number of $\overline{\nu}_e$'s created as a by-product that are detected by the the DC detectors. The far detector is located approximately 1050 m from both cores which is the distance sensitive to measuring the θ_{13} mixing angle. If there is only one detector, the far detector has to compare its $\overline{\nu}_e$ rate and spectrum to a prediction. The systematic uncertainties from the predicted $\overline{\nu}_e$ rate come from the reactor flux uncertainty and the neutrino detection systematics. These can be significantly reduced by building an exact replica of the far detector at a distance close enough to the reactors such that an un-oscillated reference spectrum can be measured for comparison. The near detector is located at approximately 400 m from both reactors and has an overburden of 120 m.w.e. The far detector was built in the same pit used by the CHOOZ experiment and has an overburden of 300 m.w.e. It was commissioned first and has been taking data since April 2011, whilst the near detector was commissioned in December 2014 and has been taking data since. As a result the analysis described in this thesis only uses data from the far detector. Figure 2.1 shows the Chooz Nuclear Power Station along with the location of the two detectors and the two reactors.

2.3 Double Chooz Detector

Double Chooz is a liquid scintillator experiment constituting of two detectors whose design can be observed schematically in Figure 2.2. Unless otherwise stated, the design is the same for the far and near detectors. Each detector consists of the Inner Detector (ID), the Inner Veto (IV) and the Outer Veto (OV). The ID along with the IV are together composed of four concentric, cylindrical vessels each of which is filled with a different liquid depending on the

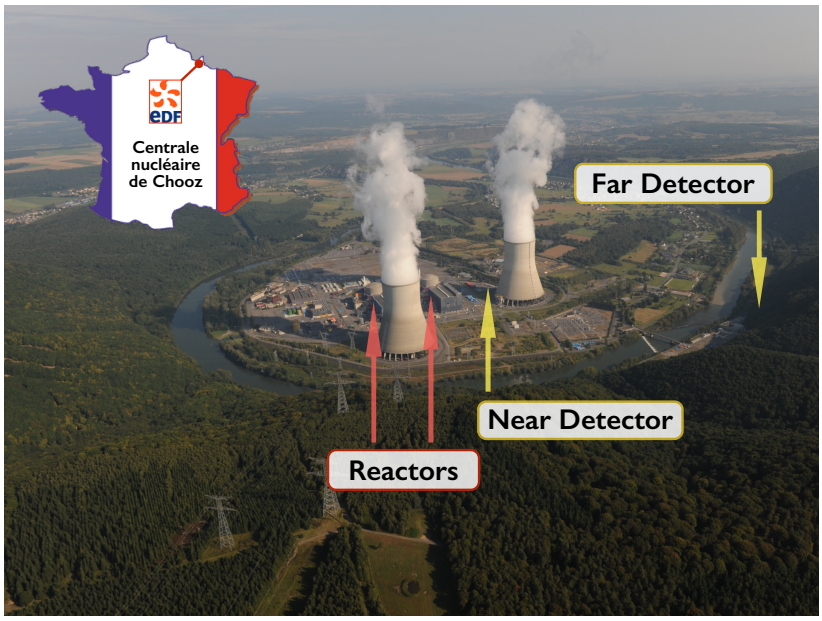

Figure 2.1 The Chooz Nuclear Power Station in Chooz, France, the location of the two Double Chooz detectors and the two reactor cores.

vessel's purpose. A chimney running from the top of the detector downwards through the middle of each vessel gives access to each volume and the liquids within them. Surrounding the whole detector is a demagnetised steel shield with a thickness of 15 cm whose purpose is to suppress externally originating γ's.

2.3.1 Inner Detector

The ID consists of three nested volumes, the centre of which is home to the Neutrino Target (NT), surrounded by the Gamma Catcher (GC), which is in turn surrounded by the Buffer. The two central volumes are housed in cylindrical acrylic vessels whilst the Buffer is contained in a stainless steel tank optically separated from the IV. The liquids were adjusted so that their densities matched $0.804 \pm 0.001\,\mathrm{g\,cm^{-3}}$ at a temperature of 15 °C minimising any stress between the volumes. The liquids were also chosen so that the light yields were similar between the NT and GC to allow for a homogeneous response throughout the two volumes.

2.3.1.1 Neutrino Target

IBD interactions take place on free protons throughout the detector, however the NT is the Fiducial Volume (FV) used to observe IBD interactions whose neutron is captured on Gd. It is the deepest part of the detector filled with a $10.3\,\mathrm{m^3}$ of Gd-loaded liquid scintillator. The

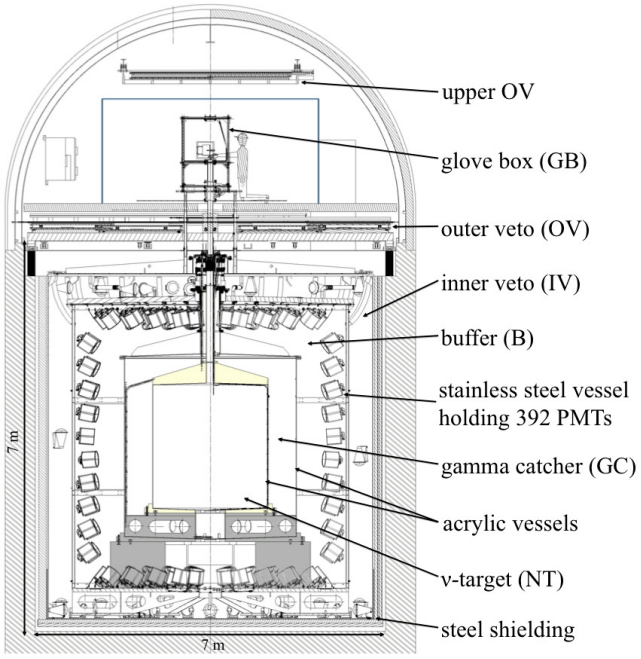

Figure 2.2 The Double Chooz detector schematic. Source [36]

scintillator translates the energy lost by ionising particles into γ's and shifts their wavelengths into a region where the Photomultiplier Tubes (PMTs) are most sensitive. It is contained in an 8 mm thick acrylic vessel transparent to light between the UV and visible spectrum.
The predecessor experiment CHOOZ also used a Gd-loaded scintillator, however, it showed a deterioration in transparency over time [26]. As a result a new type of metal loaded scintillator was developed for the DC experiment [38].
The scintillator is composed of 20 % n-dodecane ($C_{12}H_{26}$) and 80 % o-PXE (C_6H_{18}). The combination of 7 $g\,l^{-1}$ PPO and 20 $mg\,l^{-1}$ of bis-MSB are added which together shift the wavelengths to match the spectral response of the PMTs. Gadolinium is added in the form of Gd-(thd_3) which corresponds to roughly 1 g/l of Gadolinium.
There are two isotopes of Gd which have neutron capture cross sections three orders of magnitude larger than the others. They are ^{155}Gd (6.1×10^4 b) and ^{157}Gd (2.5×10^5 b) which correspond to a total γ emission of 8.54 MeV and 7.94 MeV respectively [39]. These energies are much larger than the γ's occurring naturally in and around the detector, which gives a better signal to background ratio when searching for IBD signals.

2.3.1.2 Gamma Catcher

The GC surrounds the NT with a region 55 cm wide of scintillator corresponding to a volume of 22.5 m^3. The scintillator within this volume is not loaded with Gd to limit the

detected IBD interactions to the NT. Instead it is used to detect any γ's that escape the NT. Its composition is 66 % Mineral Oil, 30 % n-dodecane and 4 % of o-PXE to which the wavelength shifters 2 gl^{-1} of PPO and 20 mgl^{-1} of bis-MSG were added [38]. The GC is contained in an acrylic vessel with a thickness of 12 mm.

2.3.1.3 Buffer

The buffer is a non-scintillating region of the ID filled with 110 m^3 of liquid composed of 53 % medicinal white oil and 47 % of an n-alkane mixture optimised for transparency and minimal scintillation light production. The buffer thickness of 105 cm shields the NT and GC from radioactivity in the PMT glass and rock surrounding the detector. It is housed in a stainless steel vessel to which 390 Hamamatsu R7081 10-inch PMTs are attached, all pointing towards the detector centre. They are surrounded by a cylindrical mu-metal shield acting as protection against magnetic fields [40]. The PMT glass is made from low activity sands using a platinum coated furnace to reduce contamination. Its radioactivity was tested during development and found to be 13, 61 and 3.3 ppb for ^{238}U, ^{232}Th and ^{40}K respectively. The PMT base circuit is housed in an epoxy resin which resulted in light flashes. They are a source of Background (BG) and are given the name Light Noise (LN) in Chapter 3.

2.3.2 Inner Veto

The IV surrounds the ID with a volume 50 cm thick containing 90 m^3 of liquid scintillator. Its composition is a mixture of linear alkyl benzene (LAB) and n-alkanes with 2 gl^{-1} of PPO and 20 mgl^{-1} of bis-MSB. It contains 78 Hamamatsu R 1408 PMTs recycled from the IMB and Super-Kamiokande experiments. Their layout was optimised in regards to maximising the number of detected photoelectrons per MeV deposited as well as high efficiency in rejecting muons and their corresponding correlated BGs using a Monte Carlo (MC) simulation [41]. The PMTs are encapsulated in a stainless steel vessel filled with mineral oil matching the optical properties of the surrounding oil. There is also a mu-metal shield to protect against magnetic fields and a transparent PET window at the front. For both the far and near detectors the walls of the buffer are covered with reflective VM2000 sheets of foil. In the case of the near detector, this is also used to cover the remaining surfaces of the IV. For the far detector, the remaining surfaces were painted with a highly reflective white coating. The IV acts both as an extra shield against externally originating fast neutrons and gammas as well as actively identifying cosmic muons that traverse it.

2.3.3 Outer Veto

The OV is mounted above the whole detector including the stainless steel shielding and is composed of two parts, the lower and upper OV. The lower OV covers an area of 13 m by 7 m with a rectangular hole of dimensions 110 cm by 30 cm at its centre where the chimney is accommodated. It is assembled from modules of 64 scintillator strips mounted in two layers, one above the other, offset by 2.5 cm. There are 32 strips in each layer running perpendicular to each other, one in the x direction and one in the y direction. The upper OV is mounted above the chimney and glove box (used to deploy the calibration sources) to cover the hole in the lower OV. Both the upper and lower OV's provide (x, y) coordinates of muons passing through them.

2.4 Trigger

The trigger system is composed of three Trigger Boards (TBs) and one Trigger Master Board (TMB). Two of the TBs are connected to the ID PMTs which are separated into two groups in an alternating manner, such that they both observe the same amount of the detector. Each Front End Electronics (FEE) module has eight PMTs connected to it and two FEE modules together (16 PMTs) build one input signal to the TB. There is an exception for two FEE modules which are only connected to three PMTs. For each TB there are 13 groups of PMTs where the multiplicity is defined as the number of groups which pass a certain threshold. The multiplicity in combination with the analogue sum of all input channels (195 PMTs) causes a trigger [42]. The trigger threshold corresponds to approximately 350 keV which gives an efficiency of 100 % for the prompt IBD events [36, 37].
In the case of the IV, there is only one trigger board. The PMTs are split into 18 different groups containing 3 to 6 PMTs each. These are separated into topological groups according to the part of the detector that they observe, top, up, lateral, down and bottom to aid event classification. The IV triggers at roughly 10 MeV which is approximately the amount of energy expected when a minimum ionising muon traverses a distance of 8 cm [36].
When the trigger criteria are met by any of the three TBs, a trigger is generated by the TMB and the waveforms of all PMTS are stored for a time period of 256 ns [37].

2.5 Electronics and Data Acquisition

The full readout and data acquisition (DAQ) system of the Double Chooz far detector is shown in Figure 2.3 [36]. Starting at the beginning of the electronics chain we have both the

ID and IV PMTs, each of which uses a single cable for the High Voltage (HV) power supply on the order of ~1.3 kV and to deliver the signal, which is equivalent to 5 mV per PE. The cables pass through a custom made splitter box which decouples the signal from the HV and passes it to the FEEs. The FEEs are responsible for amplifying and optimising the signal as well as delivering summed signals to the trigger system described in Section 2.4. The digitisation of each waveform is performed by the Flash Analogue to Digital Converter (FADC) electronics, collectively referred to as the the ν-FADC. If there is a trigger, a signal is sent to the FADCs which stores the information in the internal memories before it is read out [43].

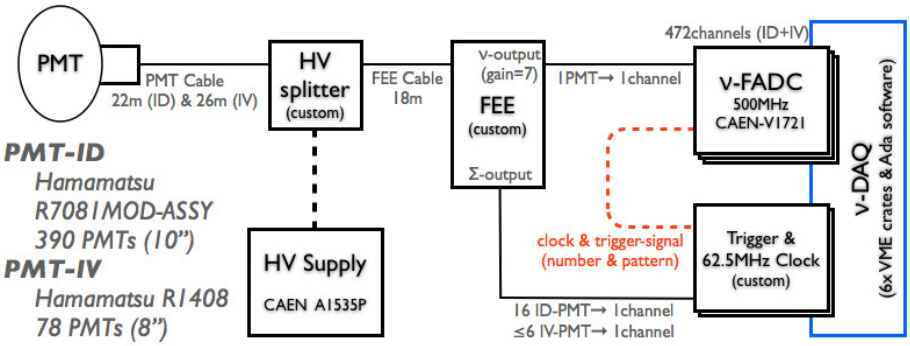

Figure 2.3 A schematic diagram of the Double Chooz data acquisition system. The analogue signals from 468 PMTs are converted into a digital waveform by the FADC and readout by the ν-DAQ. This occurs when the event passes the trigger criteria. Source [36]

2.6 Calibration Systems

The detector is calibrated using light sources, radioactive sources and cosmic muon induced events.

The light source is used to measure the time offset of the PMTs and the electronics gain on a regular basis. The light enters the ID and IV through a multi-wavelength LED-fibre system (LI) where the fibre ends are attached to the PMT cases. In the ID, light with a wavelength of 385, 425 and 470 nm is used whilst the IV uses LEDs with wavelengths of 365 and 470 nm. Their pulse width, light intensity and flash rate can be altered remotely.

Four radioactive sources ^{137}Cs, ^{68}Ge, ^{60}Co and ^{252}Cf sealed in miniature capsules are used for calibration purposes in DC. Due to their encapsulation, only the gammas and neutrons make it into the detector. They are deployed in the NT from the glove box where a motorised pulley and weight system positions the sources anywhere from 1 cm above the bottom of the NT, to the chimney where the source location is known within 1 mm. In the GC the sources

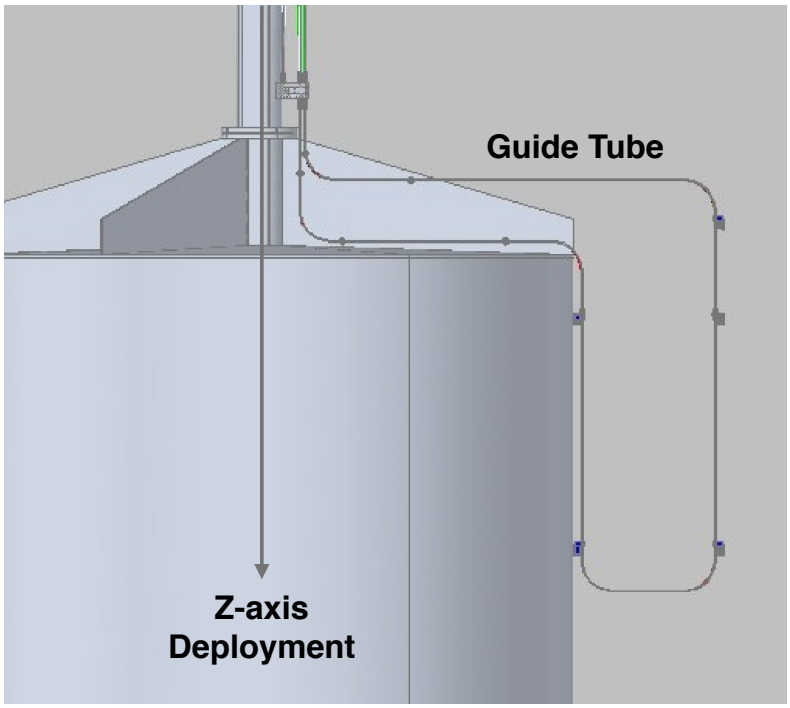

Figure 2.4 Four calibration sources can be deployed either into the NT along the z-axis or into the GC through a hermetically sealed loop. Edited from [44]

are delivered by a motor driven wire through a hermetically sealed loop which passes close to the boundaries of the NT and Buffer. The precision of the source location is known to within 1 cm whilst the perpendicular distance of the loop, when close to the NT is known to a precision of 2 mm.
Events produced by cosmic muons such as spallation neutrons captured on Hydrogen and Gadolinium are used to reconstruct the energy scale. More information about the energy scale and calibration can be found in Section 3.2.4.

Chapter 3

Measuring θ_{13} with the DC Far Detector

The DC experiment was designed with the aim of measuring the neutrino mixing angle θ_{13} using an IBD sample where the delayed neutron is captured on Gadolinium. There is a second possibility, using an IBD sample where the neutron is captured on Hydrogen. This has many challenges as the combination of the low capture energy 2.2 MeV and that the majority of these interactions take place in the GC means that there is a large BG. DC was the first of the reactor anti-neutrino experiments to publish a measurement of θ_{13} using this channel in 2013 [45].
This chapter explains the latest measurements of $\sin^2(2\theta_{13})$ from DC including the analysis techniques involved. It is split into three parts. The first explains the commonalities between the Gd and H-channel analyses. The second describes the measurement of $\sin^2(2\theta_{13})$ through the Gd-channel and the third through the H-channel where the IBD to BG ratio has been improved by a factor of ten. The final section combines the two measurements to give $\sin^2(2\theta_{13}) = 0.090 \pm 0.033$. The results are taken from [14, 36, 46]

3.1 $\overline{\nu}_e$ Prediction

The published measurements of $\sin^2(2\theta_{13})$ by DC to date have all relied on $\overline{\nu}_e$ data from a single, so called "far detector". The near detector, currently finished and taking data, will be used in the future as a reference, un-oscillated spectrum to which the detected rates or spectrum of the far detector can be compared to allow an accurate measurement of θ_{13}. Until then, a dedicated MC was developed whose aim is to create a sample of simulated IBD candidates, which should be representative of the prompt spectrum expected at the far detector in the absence of oscillation. The free parameter $\sin^2(2\theta_{13})$ is varied according to Equation 1.14 to find the best fit between data and MC. As the amount of oscillation is a

function of the energy $E_{\overline{\nu}_e}$ and distance L that the anti-neutrino has travelled from the reactor core R, both variables must be stored by the simulation.
Although experiments measuring θ_{13} use a near detector as the reference spectrum, the oscillated spectrum is made up of $\overline{\nu}_e$'s from multiple reactors with different baselines and MC modelling is required to understand the flux arriving from each.

3.1.1 Reactor Modelling and Instantaneous $\overline{\nu}_e$ Rate

There are two reactor cores, called B1 and B2 at the Chooz-B nuclear power station operated by Electricité de France (EDF). They are Pressurised Water Reactors (PWR) of the N4 type, each of which is capable of producing 4.25 GW_{th} of thermal power. More than 99.7 % of the electron anti-neutrinos are produced by β-decays of fission fragments from the four isotopes ^{235}U, ^{239}Pu, ^{238}U and ^{241}Pu. The energy released by the fission fragments is used to heat a primary loop, which in turn heats a secondary loop where steam rotates turbines, generating a maximum of 1.5 MW_e of electrical power. The thermal power P_{th}^R is recorded in increments of less than a minute, primarily using the temperature in the primary loop. Its uncertainty was evaluated by EDF in detail as it determines the maximum power at which the core can operate. At the nominal full power it is 0.5 % [36].
The instantaneous thermal power divided by the mean energy per fission gives the total number of instantaneous fissions. If the number of β-decays per fission is known, the instantaneous neutrino rate can easily be calculated. The mean energy per fission is given by:

$$\langle E_f \rangle^R = \sum_k \alpha_k^R(t) \langle E_f \rangle_k \tag{3.1}$$

where $\langle E_f \rangle_k$ is the mean energy of the kth isotope, $k = {}^{235}$U, ^{239}Pu, ^{238}U and ^{241}Pu and α_k is the fraction of the kth isotope in the fuel. The mean energy for each isotope is ^{235}U = (201.92 ± 0.46) MeV, ^{239}Pu = (209.99 ± 0.60) MeV, ^{238}U = (205.52 ± 0.96) MeV and ^{241}Pu = (213.60 ± 0.65) MeV given by [47].
A lot of effort has been expended in calculating the evolution of α_k over time. This is not important when calculating $\langle E_f \rangle^R$ in Equation 3.1. There is less than 6% difference between each $\langle E_f \rangle_k$ and a quick back of the envelope calculation shows that $\langle E_f \rangle^R$ only changes by 2 MeV over a full reactor cycle. Instead, the isotope fraction is important in later calculations.
Two reactor simulation codes are used to model the reactor cores, MURE and DRAGON [48–51]. The codes were cross checked against data from the Takahama-3 reactor and found to be consistent with other industry standard codes [52]. Detailed reactor information was used to model the cores which are made up of 205 fuel assemblies. One year corresponds to

roughly one cycle, after which one third of the fuel is replaced. EDF supplies DC with the initial burnup and location of each assembly which allows MURE to simulate the cores over the whole cycle and is cross checked against EDF's own reactor simulation code, APOLLO-2. Figure 3.1b shows a typical evolution for the isotopes' fraction as a function of burnup over a single cycle and corresponds to cycle 12 of reactor B1.

The mean cross section per fission is given by:

$$\langle \sigma_f \rangle = \sum_k \alpha_k \langle \sigma_f \rangle_k = \sum_k \alpha_k \int_0^\infty S_k(E_{\overline{\nu}_e}) \sigma_{\text{IBD}}(E_{\overline{\nu}_e}) \mathrm{d}E_{\overline{\nu}_e} \tag{3.2}$$

where $S_k(E_{\overline{\nu}_e})$ is the anti-neutrino reference spectrum of the kth isotope and σ_{IBD} is the IBD cross section, simplified from [53]:

$$\sigma_{\text{IBD}}(E_{\overline{\nu}_e}) = E_{e^+} K \sqrt{E_{e^+}^2 - m_e^2} \tag{3.3}$$

where m_e is the positron mass, E_{e^+} is the positron energy given by Equation 2.2 and K is the energy independent constant from the matrix element, which is inversely proportional to the neutron lifetime. The reference spectra for ^{235}U, ^{239}Pu and ^{241}Pu are derived from measurements of the β-spectra at the ILL (Institut Laue-Langevin) research centre [54–56]. Figure 3.1a shows all of the anti-neutrino reference spectra converted from the measured β-spectra using the conversion scheme in [57] with corrections from [58]. The anti-neutrino reference spectrum for ^{238}U shown in Figure 3.1a does not come from data but rather calculations using knowledge of the β-decay branches. This ^{238}U spectrum was used by the following DC publications [30, 36, 45]. Since then this reference spectrum has been measured in [59] and is included in the the MC simulations used to measure $\sin^2(2\theta_{13})$ in this chapter, corresponding to the DC publications [14, 46]. The uncertainty on these spectra is approximately 3 %. To reduce the large uncertainties arising from the reference spectra and increase the sensitivity to θ_{13}, the normalisation of the cross section per fission is anchored to a Bugey4 measurement of the cross section per fission $\langle \sigma_f \rangle^{\text{Bugey}}$ [62]. The measurement was taken at the Bugey nuclear power plant 15 m from the reactor core. The mean cross section per fission is given by [36]:

$$\langle \sigma_f \rangle^R = \langle \sigma_f \rangle^{\text{Bugey}} + \sum_k (\alpha_k^R - \alpha_k^{\text{Bugey}}) \langle \sigma_f \rangle_k \tag{3.4}$$

where the uncertainty on the measured cross section $\langle \sigma_f \rangle^{\text{Bugey}}$ is 1.4%. The small difference between the isotope fraction of the Bugey4 measurement and that evaluated for the Chooz reactor cores $(\alpha_k^R - \alpha_k^{\text{Bugey}})$ suppresses the uncertainty arising from the reference spectra.

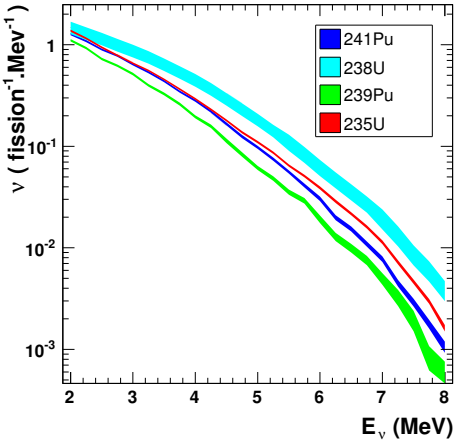

(a) The reference anti-neutrino spectra $S_k(E_{\overline{\nu}_e})$ for each isotope. N.B The ^{238}U spectrum shown is outdated and not used in this chapter. The measured spectrum from [59] is used instead. Source [60]

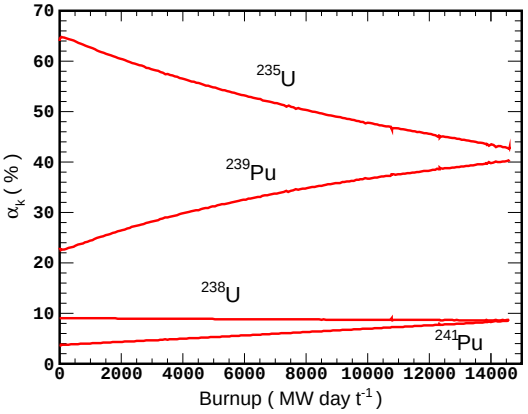

(b) A typical example of the fraction of each isotope in the fuel over a typical cycle as a function of the burnup. The example shown is taken from the B1 core and calculated using the MURE simulation code. Source [61]

Figure 3.1 Reactor core isotope $\overline{\nu}_e$ reference spectra and typical core cycle

Including the Bugey4 cross section reduces the total uncertainty on the anti-neutrino prediction from 2.8 % to 1.7 % [14].
The instantaneous detected neutrino rate is given by [36]:

$$\frac{\mathrm{d}N^R(t)}{\mathrm{d}t} = \sum_{R=1,2} \frac{\varepsilon_{\mathrm{det}} N_p}{4\pi L_R^2} \frac{P_{th}^R(t)}{\langle E_f(t)\rangle^R} \left(\frac{\langle \sigma_f(t)\rangle^R}{\sum_k \alpha_k^R \langle \sigma_f\rangle_k} \sum_k \alpha_k^R \langle \sigma_f\rangle_k \right) \tag{3.5}$$

where N_p corresponds to the number of free protons in the FV and $\varepsilon_{\mathrm{det}}$ is the detection efficiency. There are a number of variables which have a time dependency, the thermal power of each reactor core P_{th}, the mean energy released per fission $\langle E_f\rangle$ defined in Equation 3.1 and the mean cross section per fission $\langle \sigma_f\rangle$ defined in Equation 3.2. To incorporate all the uncertainties arising from Equation 3.5 a covariance matrix is constructed in neutrino energy and converted into reconstructed energy for use in the θ_{13} analysis.

3.1.2 Detector Model

The IBD candidates are generated according to the method described in Section 3.1.1 on a run by run basis to allow for a direct comparison of data to MC. The detector response is modelled using Geant4 [63, 64] which accurately describes the passage of particles through matter and includes a detailed description of the Double Chooz detector geometry. The

Readout System Simulation (RoSS) then recreates the response of the electronics to the particle interactions in the detector, such as PMTs, FEE trigger system and DAQ. Once the effects of the whole detector have been modelled correctly, a direct comparison of data and MC can be made, not only of IBD candidates but also of calibration sources and cosmogenic radioisotope decays[1] which can be used to fine tune the MC parameters.

3.2 Event Reconstruction

3.2.1 Pulse Reconstruction

When a trigger signal is sent from the TMB, an event is recorded for a time period of 256 ns. A pulse reconstruction algorithm is used to determine the start time and signal charge q for each of the 468 (390 ID and 78 IV) readout channels or PMTs.
The baseline (B_{mean}) and Root Mean Square (RMS) (B_{rms}) of each readout channel is determined using pulse triggers with a frequency of 1 Hz. The charge of each pulse is calculated by integrating the waveform over a reduced time window of 112 ns and then subtracting the pedestal which is B_{mean} integrated over the same time. This increases the charge resolution based on the width of single PE signals as up to $\sim$3 MeV each PMT typically only observes one or zero PEs. The relevant 112 ns of the waveform corresponds to the time window with the maximum integral. The charge is then calculated by subtracting the pedestal from the integral which is B_{mean} integrated over the same time window.
The start time of each waveform is given by the time when the pulse reaches 20 % of its maximum and is then corrected for PMT to PMT offsets using the LED-fibre system [36].

3.2.2 Position Reconstruction

The selection of IBD candidates does not rely on position reconstruction, however this information is used in the energy reconstruction and can be useful as a cross check to select samples of events according to their loaction. The reconstruction algorithm relies on a maximum likelihood function which assumes the event is a point-like source of light giving [36]:

$$\mathbf{x} = (x_0, y_0, z_0, t_0, \Phi) \tag{3.6}$$

where (x_0, y_0, z_0) is the event position, t_0 is the event time and (Φ photons/sr) is the light intensity per solid angle. The coordinate system is such that ($x = 0, y = 0, z = 0$) is at the

[1] The generation of cosmogenic radioisotopes is explained in more detail in 7.3.1

centre of the NT. The predicted amount of charge and arrival time of the light at the i-th PMT is given by

$$q_i' = \Phi \varepsilon_i \Omega_i(r_i) A_i \tag{3.7}$$

and

$$t_i' = t_0 + \frac{r_i}{c_n} \tag{3.8}$$

respectively, where ε_i is the quantum efficiency of the PMT, Ω_i is the solid angle subtended by the PMT at a distance r_i from the event vertex, A_i is the light transmission amplitude and c_n is the effective speed of light in the medium. The event likelihood function $\mathscr{L}(\mathbf{x})$ is defined as follows [14]:

$$\mathscr{L}(\mathbf{x}) = \prod_{q_i=0} f_q(0; q_i') \prod_{q_i>0} f_q(q_i; q_i') f_t(t_i; t_i', q_i') \tag{3.9}$$

where q_i and t_i are the observed charge and time respectively for each readout channel i. Assuming a point-like source of light, the probabilities f_q and f_t are calculated given the predicted charge q_i' and time t_i'. $\mathscr{L}(\mathbf{x})$ is maximised to give the best position $\mathbf{x}$ which is equivalent to minimising the negative log-likelihood function:

$$F_V = -\ln \mathscr{L}(\mathbf{x}) = -\sum_i \ln f_q(q_i; \mathbf{x}) - \sum_{q_i>0} \ln f_t(t_i; \mathbf{x}) \tag{3.10}$$

which can also be thought of as the goodness of the event reconstruction. For this reason F_V is used later in the analysis to remove BGs where a point like source is not expected. The performance of the event reconstruction is improved by tuning the effective light attenuation and PMT angular response using source calibration data and the charge and time likelihoods are extracted using laser calibration data. The comparison of data to MC showed better agreement after the tuning.

3.2.3 Muon Reconstruction

The muon path through the detector is reconstructed using information from PMTs in the ID. The first PMT hit is taken as the first guess for the Entry Point (EP). The preliminary Exit Point (XP) is estimated by finding the PMT which has the shortest time difference between it being hit and the time taken for the muon to travel to it from the EP. Using these starting points, the most likely first photon arrival times are computed for all other PMTs. Assuming a perfect Čerenkov/scintillation light cone around the muon track, the difference between the observed and predicted arrival times are minimised by varying EP and XP. A further

correction is made towards the detector centre to partially compensate for a general outward reconstruction drift caused by the non-uniform light production in the buffer and scintillator. Good agreement was found to MC [65].

3.2.4 Energy Reconstruction

Currently, the measurement of $\sin^2(2\theta_{13})$ in DC uses data from the far detector only. As there is no near detector data[2] whose neutrino rate can be directly compared to that of the far detector, DC relies on a prompt IBD spectrum and rate comparison of the data and prediction from MC. This requires a good understanding of the energy reconstruction for both the data and MC. The energy E_{vis} is a measure of a particle's deposited energy and its reconstruction is similar for both data and MC [14]:

$$E_{\text{vis}}^{\text{data}} = N_{\text{pe}} \times f_{\text{u}}^{\text{data}}(\rho, z) \times f_{\text{MeV}}^{\text{data}} \times f_s(E_{\text{vis}}^0, t) \tag{3.11}$$

$$E_{\text{vis}}^{\text{MC}} = N_{\text{pe}} \times f_{\text{u}}^{\text{MC}}(\rho, z) \times f_{\text{MeV}}^{\text{MC}} \times f_{\text{nl}}(E_{\text{vis}}^0) \tag{3.12}$$

The first term in each equation represents the measured charge converted to the number of photoelectrons N_{pe}. This is multiplied by the correction factors f_{u} and f_{MeV} corresponding to the spatial non-uniformity and absolute energy scale. The time stability correction f_s only applies to data and the non-linearity correction f_{nl} only applies to the MC. ρ and z refer to the event position in cylindrical coordinates reconstructed as defined in Section 3.2.2 and t is the time of the event measured in days since the beginning of data taking. E_{vis}^0 represents the energy after the non-uniformity correction is applied and is needed as input to the last terms of Equations 3.11 and 3.12 as they represent a correction which is energy dependent and separate for MC and data.

3.2.4.1 Linearised PE calibration

The number of photoelectrons N_{pe} is given by the sum of every channel i [14]:

$$N_{pe} = \sum_{i}^{390} \frac{q_i}{g_i^m(q_i, t)} \tag{3.13}$$

where m represents either the data or MC, q_i is the charge reconstructed for each channel as described in Section 3.2.1 and g is the gain or charge-to-PE conversion factor.

[2]The near detector has been taking data since December 2014

3.2.4.2 Non-uniformity Calibration

f_u represents a correction to the reconstructed energy as function of the reconstructed position in the detector. The PMTs don't cover 100 % of the ID but they do all point towards the detector centre. Scintillation light from energy depositions in regions further away from the centre are less likely to be detected. As a result, some regions of the detector will be reconstructed with an energy lower than what is observed in the centre, as is shown in 3.2a. This is corrected using non-uniformity correction maps based on the position reconstruction variables ρ and z. Maps for data and MC were created using the neutron capture peak on H such that every event would have the same energy as if it had been observed in the detector centre. The non-uniformity correction map for data was created using cosmic spallation neutrons within 1 ms of a detected muon, shown in Figure 3.2a whilst the map for MC was created using the delayed neutron capture from IBD interactions.

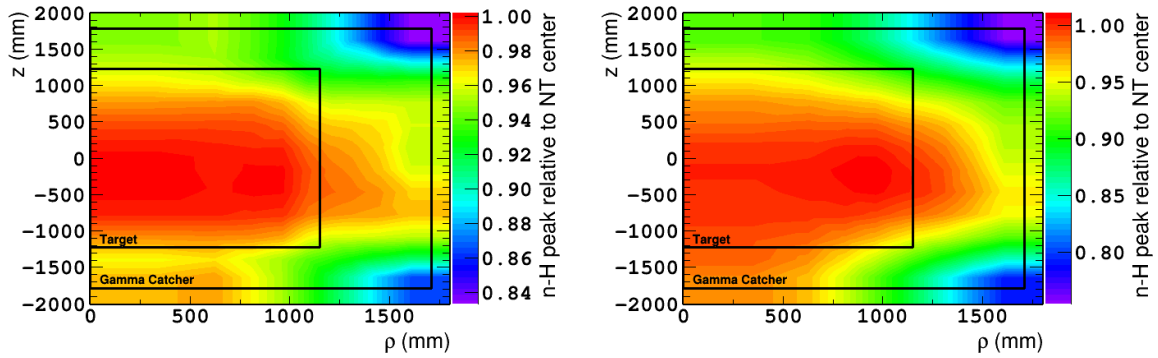

(a) Created and used by data. Source [14]

(b) Created and used by MC. Source [66]

Figure 3.2 The non-uniformity correction maps based on the reconstructed position of the event in teh detector

3.2.4.3 Energy Scale Calibration

The number of photoelectrons N_{pe} in Equations 3.11 and 3.12 is converted into the absolute energy scale in MeV using the conversion factor f_{MeV}, calculated for data and MC. A ^{252}Cf source deployed in the centre of the NT is used to observe neutron capture on hydrogen emitting a γ with a characteristic energy 2.223 MeV. The capture peak as observed in Figure 3.3 is used to measure $(1/f_{MeV})$ and found to be 186.2 p.e. / MeV for data shown in black and 186.6 p.e. / MeV for MC shown in red.

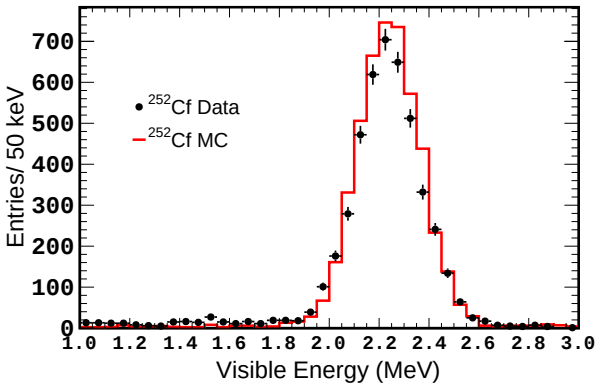

Figure 3.3 The absolute energy scale is calibrated using a ^{252}Cf source at the centre of the NT. The neutron capture peak on hydrogen is used to calculate the conversion factor for PE to MeV. The red line depicts MC and the black points data. Source: [14]

3.2.4.4 Stability Calibration

A time dependent correction function f_s is only applied to data and can be separated into two components. The first is shown to have an energy dependence using three sources of calibration with different energies, spallation neutron capture on Gadolinium (8 MeV) and Hydrogen (2.2 MeV) and α's from the ^{212}Bi-^{212}Po decay chain. Although the α's have an energy of 8.8 MeV, quenching in the scintillator means that only approximately 1 MeV is observed, allowing for calibration at a low energy. To calculate the energy dependence, the RMS of each calibration point was minimised over time and shown to have a linear dependence. The lowest energy point from the α's requires the largest correction, attributed to single PE inefficiency and baseline estimation bias. The H capture peak was then used to calculate the correction as a function of time. The cause of this variation is thought to arise from fluctuations in detector response such as baseline estimation and gain change after power cycles.
The second correction is due to readout and scintillator response drift and is a linear correction as a function of time. This drift was measured using neutron capture on H throughout the NT and GC and found to increase by 0.3 %/year. Figure 3.4 shows the peak variation of all three calibration sources, n-H, n-Gd and α's after the time stability correction is applied.

3.2.4.5 Energy Non-Linearity Calibration

Following the corrections to the energy scale discussed throughout the previous sections, there are still two remaining sources of discrepancy between the data and MC. The first is

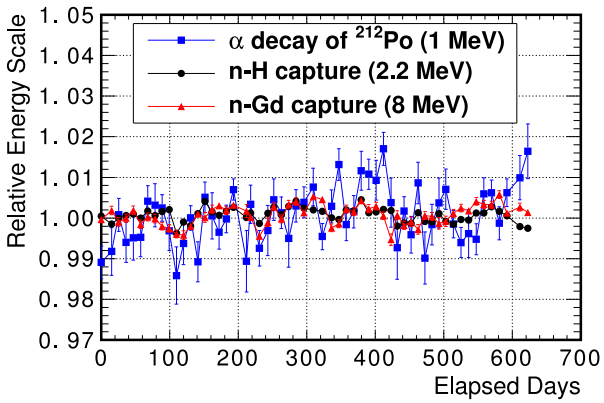

Figure 3.4 The peak variation of the α's (1 MeV) from the ^{212}Bi-^{212}Po decay chain, spallation neutron capture on H (2.2 MeV) and Gd (8 MeV) after the time stability correction is applied. Source [14]

labelled the Charge Non-Linearity (QNL) and the second the Light Non-Linearity (LNL) where both corrections are only applied to the visible energy of the MC.

Charge Non-Linearity: A discrepancy between MC and data was observed using calibration data from all four sources deployed at various locations along the Z-axis of the detector. It was found that there was a visible energy dependent discrepancy when comparing data to MC, which has been labelled the QNL. The correction function applied to the MC is extracted using a ^{252}Cf source deployed at the NT centre. A linear function is fitted between the H and Gd neutron capture peaks and is used to correct the visible energy of the MC using the following function [14]:

$$f_{nl}(E^0_{vis}) = 0.0023 \times E^0_{vis}[\text{MeV}] + 0.9949 \tag{3.14}$$

The QNL is thought to arise from biases in the modelling of the readout systems and charge integration algorithm.

Light Non-Linearity: After the QNL correction is applied, a discrepancy between the single γ energy of all calibration sources between data and MC was still observed on the 1.5 % level at low energies. The black points in Figure 3.5 represent the ratio of the visible energy from data and the QNL corrected visible energy of the MC for four calibration sources as a function of single γ energy. Neutron capture on H emits a single γ with an energy of 2.22 MeV in comparison to neutron capture on Gd which emits a total of 8 MeV but from a number of γ's whose average energy is about 2.2 MeV. This makes a comparison

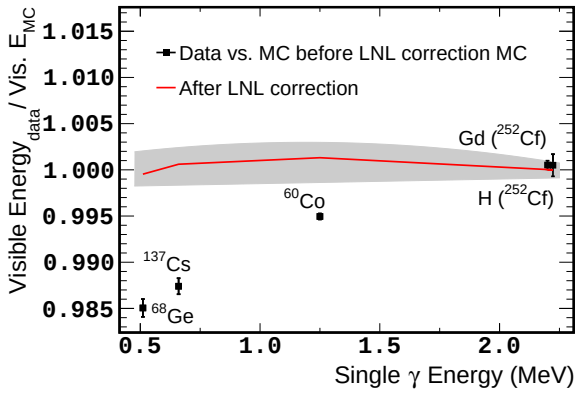

Figure 3.5 The points show the discrepancy for single γ's between MC and data after the QNL correction has been applied. They have been extracted from calibration sources deployed at the centre of the NT. The red line shows the same points after the LNL correction has been applied and the grey band is the associated systematic uncertainty. The γ multiplicity for neutron capture on Gd was evaluated using MC. Source [14]

of the visible energy from neutron capture on Gd normalised to the number of γ's released to H possible. Figure 3.5 shows very little discrepancy between the two implying it is not dependent on the visible energy. As a result the discrepancy is thought to arise from the scintillator modelling in the MC and is therefore particle dependent.

To evaluate the LNL, several combinations of Birk's quenching parameter kB and the light yield of the liquid scintillator were varied within the range of the laboratory measurement and corresponding uncertainty. MC simulations were produced for each pair and those that best matched the data were used to generate positron MC. The positrons were generated with various energies ranging across the whole positron spectrum from IBD interactions. These were compared to positrons created with the default pair of kB and light yield used in the MC where the discrepancy was evaluated as the LNL. As the LNL correction is particle dependent it is only applied in the $\sin^2(2\theta_{13})$ fit explained in 3.7.2.

3.2.4.6 MC Energy Scale Modelling

In Section 3.7.2 the MC energy scale is corrected to best match the data as follows [67]:

$$E_{\text{fit}}^{MC} = a'_{CV} + b'_{CV} \cdot E_{\text{vis}}^{MC} + c'_{CV} \cdot (E_{\text{vis}}^{MC})^2 \tag{3.15}$$

The values for a', b' and c' are determined from the previous sections and called the central values (CV). In the case of the Gd data sample they are:

$$\begin{aligned} a'_{CV} &= -0.0271 \pm 0.0062\text{MeV} \\ b'_{CV} &= 1.0120 \pm 0.0077 \\ c'_{CV} &= -0.0001 \pm 0.0006\text{MeV}^{-1} \end{aligned}$$

with their corresponding correlations:

$$\begin{pmatrix} \rho_{a'a'} & \rho_{a'b'} & \rho_{a'c'} \\ \rho_{b'a'} & \rho_{b'b'} & \rho_{b'c'} \\ \rho_{c'a'} & \rho_{c'b'} & \rho_{c'c'} \end{pmatrix} = \begin{pmatrix} 1 & -0.30387 & 0.00708 \\ -0.30387 & 1 & -0.28553 \\ 0.00708 & -0.28553 & 1 \end{pmatrix}$$

In the case of the H data sample, a different approach wad taken as the LNL had not been evaluated in the GC. However, the same plot shown in Figure 3.5 was created using calibration source data in the GC and showed that the LNL acts in the opposite direction. As a consequence, the approach taken was to assume the LNL was not known for the H MC. This means the LNL correction is not applied to the MC and instead freedom is given to the $\sin^2(2\theta_{13})$ fit to find the CVs itself. The CVs are given only by the QNL:

$$\begin{aligned} a'_{CV} &= 0.000 \pm 0.067\text{MeV} \\ b'_{CV} &= 1.004 \pm 0.022 \\ c'_{CV} &= -0.0001 \pm 0.0006\text{MeV}^{-1} \end{aligned}$$

The errors on the CVs are calculated such that they cover the LNL correction used for the Gd data plus two times the uncertainty on the CV, acting both in and against the correction from unity.

3.2.4.7 Energy Scale Systematic Uncertainty and Resolution

Figure 3.6 shows a comparison of the energy resolution as a function of visible energy for both the data and MC. The plots include calibration sources placed at the centre of the NT and spallation neutron capture on Gd, H and Carbon from the GC. The points are fitted with the following function [14]:

$$\frac{\sigma}{E_{\text{vis}}} = \sqrt{\frac{a^2}{E_{\text{vis}}} + b^2 + \frac{c^2}{E_{\text{vis}}^2}} \tag{3.16}$$

where a, b and c represent the statistical fluctuation, constant term and energy independent width due to electronic noise respectively. The best fit results to the data return $a = 0.077 \pm 0.002\,\mathrm{MeV}^{\frac{1}{2}}$, $b = 0.018 \pm 0.001$ and $c = 0.017 \pm 0.011\,\mathrm{MeV}$ and the best fit results from the MC return $a = 0.077 \pm 0.002\,\mathrm{MeV}^{\frac{1}{2}}$, $b = 0.018 \pm 0.001$ and $c = 0.024 \pm 0.006\,\mathrm{MeV}$. The comparison of these parameters shows consistency between the data and MC.

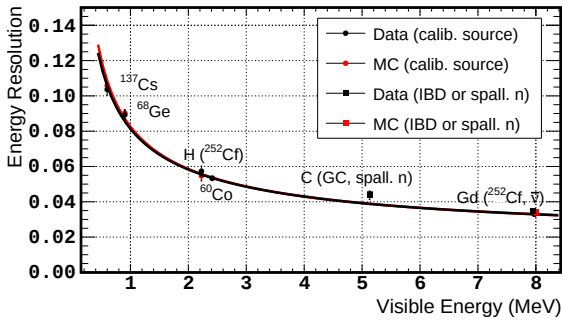

Figure 3.6 A comparison of the data (shown in red) and MC (shown in black). The horizontal axis shows the reconstructed visible energy and the vertical axis the corresponding resolution. Represented are all four calibration sources deployed at the centre of the NT (circular points) and spallation neutron captures on Gd, Carbon and H (square points). The curves are the best fit results when the points are fitted with Equation 3.16. Source: [14]

3.3 IBD Selection

3.3.1 Single Event Selection and Discrimination

At the first stage of event discrimination, any event with a visible energy less than 0.4 MeV is rejected. If an event has $E^{\mu}_{\mathrm{vis}} > 20\,\mathrm{MeV}$ or $E_{\mathrm{IV}} > 16\,\mathrm{MeV}$, where E_{IV} refers to the energy deposited in the IV, then it is classified as a muon. Any such event introduces a dead time where all events within 1 ms are rejected in the Gd analysis [14] and in the case of the H analysis [46] the dead time is extended to 1.25 ms. The dead time removes BGs correlated to the muon such as spallation neutrons which could mimic the IBD signal. It is extended for the H analysis as the average neutron capture time is longer. Any other event is classified as a singles event and may be used in the classification of IBD interactions.

3.3.2 Light Noise

It is known that the bases of the PMTs in the ID occasionally create flashes of light known as Light Noise (LN). A number of analysis techniques have been developed which successfully remove them and are applied to both the H and Gd analyses. They take advantage of their physical properties, for example that their location at the base of a PMT means that the very same PMT will see a large amount of light compared to the others. Events which satisfy at least one of the following criteria are discarded as LN:

1. $q_{\max}/q_{\text{tot}} > 0.12$
2. $\sigma_t > 36\,\text{ns}$ and $\sigma_q > (464 - 8\sigma_t)$ CU (Charge Units)
3. $Q_{\text{dev}} > 3 \times 10^4$ CU

The first selection cut, $q_{\max}/q_{\text{tot}}$ is the PMT with the largest amount of charge $q_{\max}$ divided by the total charge of the event q_{tot}. The second cut refers to the RMS of the PMT hit times σ_t and the RMS of the integrated charge σ_q for each event. The last selection cut is given by $Q_{\text{dev}} = 1/N \times \sum_i^N (q_{\max} - q_i)^2/q_i$ where i is a PMT within a sphere of radius 1 m whose center is the PMT with the largest recorded charge.

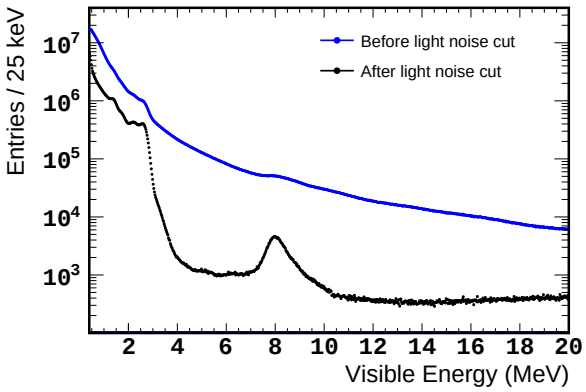

Figure 3.7 The singles spectrum of ID events described in Section 3.3.1 is shown in blue. The spectrum after the LN cuts described in Section 3.3.2 is shown in black. Source: [14]

Figure 3.7 shows the singles spectrum in blue whose selection is described in Section 3.3.1. The spectrum shown in black has had most of the LN BG removed using the selection criteria described in Section 3.3.2. It clearly shows the Gd capture peak and the radioactive contaminants from impurities in the detector such as the 2.6 MeV γ from ^{208}Tl found in the PMT glass.

Table 3.1 Comparison of the neutrino selection criteria for the Gd and H IBD data sets. From [14, 46]

	Gd	H
Prompt visible energy (MeV)	$0.5 < E_p < 20$	$1 < E_p < 20$
Delayed visible energy (MeV)	$4 < E_d < 10$	$1.3 < E_d < 3$
Time difference prompt and delayed (µs)	$0.5 < \Delta T < 150$	$0.5 < \Delta T < 800$
Distance prompt and delayed (cm)	$\Delta R < 100$	$\Delta R < 120$
Isolation cut relative to prompt (µs)	$[-200, +600]$	$[-800, +900]$

3.3.3 Prompt and Delayed Selection

The basic selection criteria for IBD interactions are summarised in Table 3.1 for both the Gd [14] and H [46] analyses. The positron is the first observable event in an IBD interaction and is labelled the prompt event. The prompt energy window starts at 0.5 MeV for the Gd analysis resulting in almost 100 % prompt selection efficiency. In contrast, the prompt energy window for the H analysis begins at 1 MeV to remove γ contamination in the spectrum. This occurs when an IBD interaction takes place in the buffer and only one of the γ's from the positron annihilation enters the GC, creating a peak at 0.511 MeV. The delayed neutron from the same interaction then either enters the GC and is captured or is captured in the buffer and the 2.2 MeV γ enters the GC. As the γ energy can't be directly translated into anti-neutrino energy and the efficiency isn't well understood, it is easier to remove these events by increasing the start of the prompt energy window. The prompt visible energy window extends to 20 MeV ofr both analyses to give a better handle on the BG estimation.

The second observable of the IBD interaction, the delayed event, refers to the neutron capture on either H or Gd. As their capture energies are different, the energy window is correspondingly focused around a separate region for each and as the cross section for neutron capture on Gd is larger than on H, the average neutron capture time is shorter. This results in a larger time window between the prompt and delayed event for H of 800 µs compared to 150 µs for Gd.

The isolation cut stipulates that there should be no other events except for the prompt and delayed event within the time window specified. This is to make sure that a group of neutrons arriving together created by the same parent muon which hasn't been observed by the detector won't be mistakenly identified as an IBD candidate.

Gadolinium Analysis

This is where the Gd and H analyses separate, but they are reunited again at the very end of the chapter. This section explains the techniques used in the measurement of $\sin^2(2\theta_{13})$ through the Gd-channel, although some of the methods apply to the H section as well. The data set corresponds to the time period between April 2011 and January 2013 corresponding to 467.9 days of live time.

3.4 Background Reduction

The double coincidence between the prompt and delayed event removes a large amount of BG. The majority of the remaining BGs are either two events correlated to each other or to the same muon. A number of vetoes have been developed to remove these from the IBD sample and are explained in this section. More information about the BGs themselves can be found in Section 3.5.

3.4.1 Functional Value Veto

The F_{V} explained in Section 3.2.2 is a measure of how well an event is reconstructed or how point-like it is. It can be used to remove events which are not point like such as stopping muons and their decay products Michel electrons. High energy LN events which are reconstructed far from the detector centre also have large values of F_{V}. The F_{V} is defined in Equation 3.10 as the logarithm of the charge. As the charge is proportional to the energy an exponential relationship between energy and F_{V} is expected as follows [46]:

$$E_d = Ae^{F_{\mathrm{V}}/B} \tag{3.17}$$

where E_d is the visible energy of the delayed event and A and B are parameters whose values need to be chosen to effectively reject non IBD like events. Figure 3.8 shows the F_{V} plotted against the visible energy of the delayed events. Events with $E_{\mathrm{vis}} > 0.068 \times \exp(F_{\mathrm{V}}/1.23)$ are rejected by the F_{V} veto and this cut is represented by the blue line. Black data points to the left of the blue line are IBD candidates and the events circled in red to the right of the line are rejected as BG. The band of events closest to the line on the right side represent either stopping muons which haven't been tagged by the IV or OV as they have entered the detector through the chimney or Michel electrons. Events to the right of this band with higher values of F_{V} are thought to be LN.

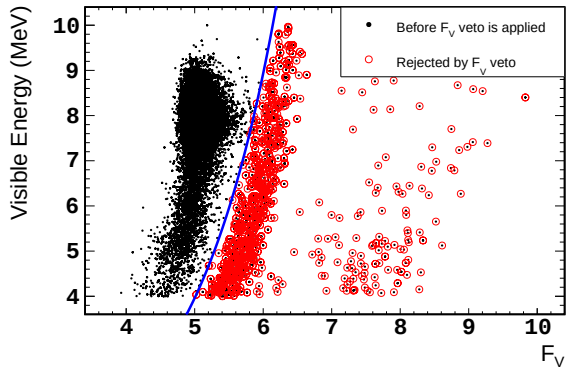

Figure 3.8 Black data points represent the visible energy of delayed events along with their corresponding F_V. The blue line represents the selection boundary, where events to the right of the line are rejected and are circled in red. The rejected events correspond to stopping muon, Michel electrons or LN. Source: [14]

3.4.2 OV Veto

Prompt events which are within 224 ns of an OV hit are rejected as stopping muons.

3.4.3 IV Veto

Muons passing through, close-by or only partly through the detector create secondary particles composed mostly of neutrons. These secondary particles are expected to be correlated to each other by both distance and time. This includes events which occur in the IV but have an energy lower than the muon threshold such as proton recoil from a neutron, a neutron capture or a γ. An artificial neural network was used to reconstruct the position of these events within the IV. A dedicated MC of 1 MeV electrons simulated throughout the IV was used to train the neural network. The distance and time correlation of events in the IV and ID characterised by the following cuts:

- IV PMT multiplicity ≥ 2
- $Q_{\text{IV}} > 400$ CU ≈ 0.2 MeV
- $\Delta d_{\text{ID-IV}} < 3.7$ m
- $0\,\text{ns} < \Delta T_{\text{ID-IV}} < 100\,\text{ns}$

are rejected as BGs. If there is an event in the IV characterised by the first two bullet points, is within 3.7 m and occurs 0 ns to 100 ns before a prompt like event in the ID, it is rejected. This could, for example represent a fast neutron which deposits energy in the IV first, for

example by proton recoil and is then captured or deposits energy via another proton recoil in the ID.

3.4.4 $\mathscr{L}_{Li}$ Veto

The $\mathscr{L}_{Li}$ veto rejects events by calculating the probability, or likelihood $\mathscr{L}_{Li}$ that a prompt event is a β-n emitter. These are radioactive nuclides created by cosmic muons whose characteristic decay chain is a β^- particle followed by the emission of a neutron. This chain of decays can easily mimic the IBD signal and their long decay times 257 ms and 172 ms for ^{9}Li and ^{8}He respectively make them difficult to identify. Using their correlation to a parent muon candidate the $\mathscr{L}_{Li}$ can be calculated leading to effective rejection.
As the number of β-n events is small, the $\mathscr{L}_{Li}$ makes use of another cosmogenic radioisotope that occurs in abundance, ^{12}B. Many variables were considered, however distance between the muon and prompt event and the number of neutrons detected after that muon were found to be the most effective. PDFs were created for both the signal and BG representing the variables just mentioned and using Bayes Theorem:

$$\mathscr{L}_{Li} = P(\beta\text{-n}|\mathbf{x}) = \frac{P(\beta\text{-n})P(\mathbf{x}|\beta\text{-n})}{P(\beta\text{-n})P(\mathbf{x}|\beta\text{-n}) + P(BG)P(\mathbf{x}|BG)} \tag{3.18}$$

where $\mathbf{x}$ denotes the variables included in the likelihood, the distance between the prompt and muon event and the number of neutrons after that muon, and BG refers to the same variables but their relationship to prompt IBD candidates instead. The $\mathscr{L}_{Li}$ is calculated for all muon-prompt pairs for a time window of 700 ms prior to the prompt event. The pair with the highest $\mathscr{L}_{Li}$ is stored and if it satisfies $\mathscr{L}_{Li} > 0.4$ the event is rejected [68].

3.4.5 Summary of the Vetoes

Figure 3.9 depicts the IBD candidates before (grey triangles) and after (black circles) all the vetoes have been applied. The top plots shows the prompt event visible energy spectra, the middle the delayed visible energy spectra and the bottom plot shows the time correlation between the two. The histograms shown in colour reflect the events rejected by each veto. The F_{V} shown in pink rejects predominantly stopping muons and Michel electrons. This is reflected in the flat prompt and delayed visible energy spectra and in the time correlation plot where the lifetime of the distribution is much smaller than for neutron capture as the decay time for a muon is 2.2 µs. The OV shown in blue follows a similar distribution in the three plots as it also rejects stopping muons.

The IVV shown in red has a flat distribution in the prompt visible spectrum, but the delayed visible spectrum contains a flat distribution from proton recoil with an addition peak due to the capture of thermalised fast neutrons. The time distribution shows a correlation between the prompt and delayed events on a much shorter time scale than IBD interactions.
The $\mathscr{L}_{Li}$ veto shown in green has the characteristic β-spectrum in the prompt visible energy. The delayed energy spectrum and time distribution show no difference to the IBD interactions.
The IBD sample shown in black is much cleaner as a result of all the vetoes, the prompt positron spectrum is more dominant as is the neutron capture peak in the delayed spectrum showing the effectiveness of the vetoes.
The inefficiencies to the IBD candidates introduced by the F_{V} veto, OV veto and IV Veto (IVV) are 0.06 ± 0.11 %, 0.058 ± 0.001 % and 0.035 ± 0.014 % respectively. The inefficiency introduced by the $\mathscr{L}_{Li}$ veto 0.504 ± 0.018 % [14] is almost a tenth of that compared to the previous publication 4.8 % [36].

3.5 Background Measurements

3.5.1 Accidentals

Accidentals are two single events, uncorrelated to each other, but which by chance happen to pass the IBD selection criteria. These could be from naturally occurring radioisotopes, ^{12}B decays, proton recoils or neutron captures. Their contribution to the IBD sample can be estimated by creating 2000 off-time windows [69], following the same prompt selection criteria but offset by 1 s. This large number of windows allows a reduction in the statistical error of the prompt spectrum used in the $\sin^2(2\theta_{13})$ fit in Section 3.7.2 and in the calculation of the accidentals rate. The accidentals prompt spectrum is shown in Figure 3.10 where each energy bin is given in terms of the rate per day. The accidentals rate is measured to be $0.0701 \pm 0.0003(\mathrm{stat}) \pm 0.0026(\mathrm{syst})\,\mathrm{day}^{-1}$ and is the most precisely known of all the BGs.

3.5.2 Fast Neutrons and Stopping Muons

This section describes BGs where the prompt and delayed events are either correlated to each other or to the same muon. A cosmic muon passing through or close to the detector creates many secondary particles, of which a large number are spallation neutrons. Neutrons created in this way tend to have large energies before they thermalise, giving them their name Fast Neutrons (FN). Within the detector, neutrons can knock into protons and pass on some of their momentum, labelled recoil protons. Recoil protons pass the prompt selection

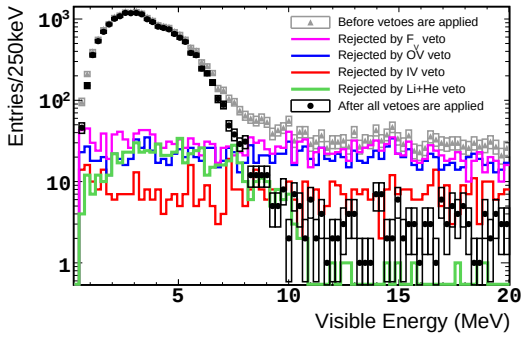

(a) Prompt visible energy

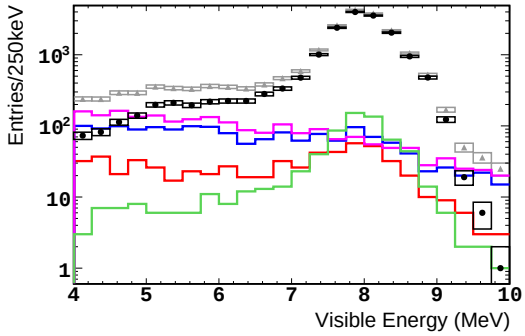

(b) Delayed visible energy

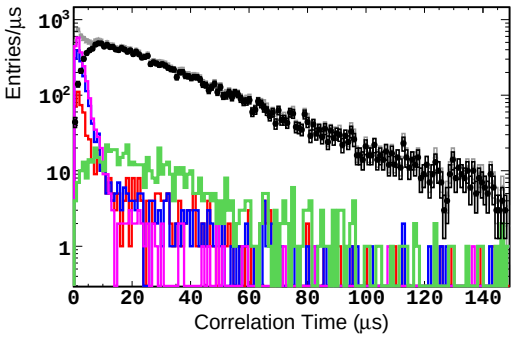

(c) Time difference between the prompt and delayed events

Figure 3.9 The three plots show the IBD candidates before (grey triangular points) and after (black circular points) the vetoes described in Section 3.4 have been applied. Each separate colour represents the events rejected by each veto method. Source: [14]

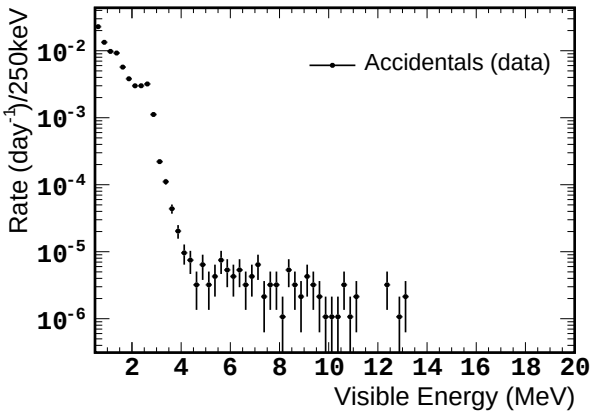

Figure 3.10 The prompt spectrum for accidental events. A large number of windows recreating the prompt selection criteria and offset from each IBD candidate by 1 s were used to create the spectrum and estimate the accidentals rate. Corrections were made for IBD inefficiencies and the vetoes mentioned in Section 3.4. Source: [14]

criteria whilst either the same neutron or another created by the same muon which has since thermalised is captured and observed as the delayed event.
Muons which stop in the detector are not always detected if they enter through the chimney. If they subsequently decay into a Michel electron, this double coincidence can be mistaken for an IBD candidate. The majority of these events are rejected using the F_{V} veto described in Section 3.4 and all that remains is the FN background. The method of measuring their shape and rate is easily explained with the aid of Figure 3.11 which shows the prompt spectra for three separate selections. The black data points show the IBD candidates. The red data points show the events rejected by the IVV used to evaluate the spectral shape of the FNs. They are fitted with a linear function and found to have a slope of -0.02 ± 0.11 events/MeV^2. The third sample of events has the same selection criteria as the IBD candidates but with the prompt energy window extended from 20 MeV to 30 MeV represented by hollow circles. These points are used to estimate the FN rate of $0.604 \pm 0.051\,\mathrm{day}^{-1}$.

3.5.3 Cosmogenic Radioisotopes

Cosmogenic radioisotopes are created by cosmic muons passing through or near to the detector. The cosmogenic BG described in this section refers to radioisotopes which undergo two decays, a β-decay followed by a neutron emission. These β-n emitters have a double coincidence which can mimic the IBD signal and their relatively long lifetimes of 257 ms and 172 ms for ^{9}Li and ^{8}He respectively in comparison to the Gd muon veto time of 1 ms, makes them difficult to veto.

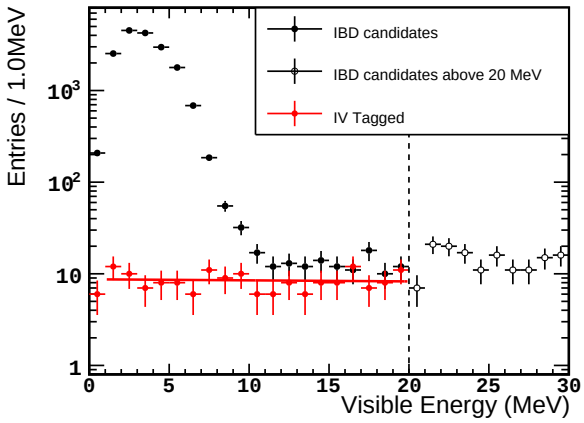

Figure 3.11 The prompt energy spectra for three samples of events. The IBD candidates from data (black points), the events rejected by the IVV (red points) used to estimate their shape from the best fit (red line) with a slope of -0.02 ± 0.11 events/MeV^2. Events above 20 MeV (hollow points) are IBD candidates but with the prompt energy extended to 30 MeV and are used to measure the FN BG rate. Source: [14]

The β-n BG rate is estimated using the $\Delta T_{p\text{-}\mu}$ distribution of all prompt and muon pairs extending backwards for a period of 20 s. This works well in the situations where there is a large signal to BG ratio such as muons with a visible energy greater than 600 MeV. However, muons at the lower end of the visible energy spectrum have a small signal to BG ratio and the fit can return large errors. To minimise this effect, the distance correlation between the muon and the prompt β-decay can be exploited, although first the efficiency of such a distance cut needs to be evaluated. This can be done by taking a relatively pure sample of β-n emitters, using only muons with $E^{\mu}_{\text{vis}} > 600\,\text{MeV}$[3] and performing a BG subtraction to get the Lateral Distance Profile (LDP) of β-n prompt events to the parent muon. This can be achieved by fitting the LDP to a toy MC including the geometrical effects of the detector, the characteristic distance of β-n prompt events to the muon λ_{Li}, smearing of the muon reconstruction σ_{μ} and smearing of the prompt vertex reconstruction which is fixed at $\sigma_{\text{X}} = 10\,\text{cm}$. The fit returns $\lambda_{\text{Li}} = 42 \pm 4\,\text{cm}$ and $\sigma_{\mu} = 15 \pm 4\,\text{cm}$. These two parameters can be used to recreate the expected LDPs for different muon visible energies which can be used to estimate the efficiency of a given distance cut. The total rate after correcting for the distance cut is $2.2^{+0.35}_{-0.27}\,\text{day}^{-1}$.
To constrain the BG rate further, a Li-enriched sample is obtained using the following cuts:

1. $E^{\mu}_{\text{vis}} > 300\,\text{MeV}$ and more than one neutron within 1 ms

[3]The muon visible energy is the same as E_{vis} but without the non-uniformity correction

2. $E^{\mu}_{\text{vis}} > 500\,\text{MeV}$, $d < 0.75\,\text{m}$ and no neutrons

The fit to the the Li-enriched sample returns a β-n rate of $2.05 \pm 0.13\,\text{day}^{-1}$. Combining this with the previous rate gives a constrained rate of $2.08^{+0.41}_{-0.15}\,\text{day}^{-1}$. This includes systematic uncertainties from the binning, uncertainty on the ^{8}He fraction and toy MC parameters.
The rate mentioned in the previous sample contains the β-n rate from the whole IBD sample set, but doesn't take into account the BG removed using the $\mathscr{L}_{Li}$ veto. The rate of β-n events rejected by the $\mathscr{L}_{Li}$ veto is evaluated to be $1.12 \pm 0.05\,\text{day}^{-1}$. Subtracting this from the total rate gives the remaining β-n BG rate of $0.97^{+0.41}_{-0.16}\,\text{day}^{-1}$.
The prompt spectrum is obtained by taking the events rejected by the $\mathscr{L}_{Li}$ veto and performing a BG subtraction. The spectrum can be seen in Figure 3.12 from data as black data points together with the ^{9}Li predicted spectrum from MC and its uncertainty normalised to the number of events in red.

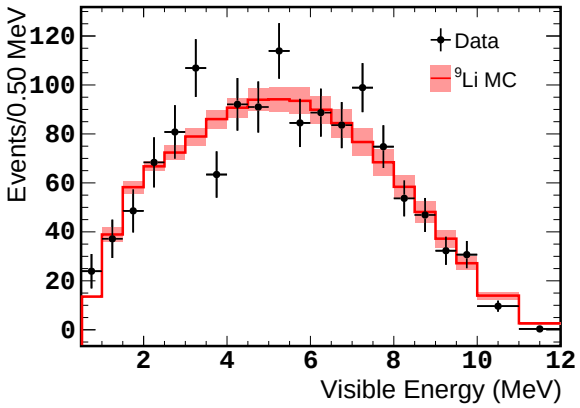

Figure 3.12 The prompt energy spectrum of the β-n emitters used in the $\sin^2(2\theta_{13})$ fit. The red line shows the ^{9}Li spectrum prediction from MC scaled to the number of events and the red band shows the uncertainty. Source: [14]

3.6 IBD Inefficiency

The vetoes described in Section 3.4 introduce an inefficiency into the IBD data sample which needs to be evaluated so that it can be applied to the MC generated IBD sample. In addition, inefficiencies brought about by detection and selection are measured and compared to MC to cross check if there is any discrepancy between the two. Table 3.2 summarises the MC correction factors. The muon veto corrects for the 1 ms dead time introduced after every muon. The IBD selection efficiency corrects for differences due to $\Delta T, \Delta R$, delayed E_{vis}

Table 3.2 The MC IBD correction factors and their uncertainties due to selection, detection and veto inefficiencies. From [14]

	MC correction	Uncertainty (%)
Muon Veto	0.955	< 0.1
IBD selection	0.989	0.2
FV, OV, IV vetoes	0.998	0.1
$\mathscr{L}_{\mathrm{Li}}$ veto	0.995	0.02
Gd fraction	0.975	0.4
Spill in/out	1.000	0.3
Proton number	1.000	0.3
Total	0.915	0.6

selection cuts, LN and isolation cuts. The next two values correct for inefficiencies from the BG reduction vetoes. Not all of the neutrons in the IBD sample are captured on Gd, some are captured on H and this depends on the Gd concentration in the NT and the correct modelling in the MC. The difference between the data and MC is demonstrated by the fifth line in the table. Spill in/out is caused by IBD neutrons crossing the NT and GC boundary, where the net current is into the NT as neutrons tend to travel further in the GC before being captured. Finally, the proton number is the uncertainty on the number of free protons available to interact with $\overline{\nu}_e$'s. The total MC correction factor is 0.915 ± 0.006.

3.7 Neutrino Oscillation Analysis for θ_{13}

3.7.1 Reactor Rate Modulation

A direct comparison of the expected $\overline{\nu}_e$ rate R^{exp} to the observed rate R^{obs} can be used to determine θ_{13}. The data taking period is separated into seven different amounts of reactor thermal power (P_{th}) characterised by:

1. Two reactors off (2-off)
2. One reactor on and one reactor off (1-on)
3. Two reactors on (2-on)

where periods 1. and 2. are each separated into three further bins according to the total P_{th} from both reactors. A linear correlation is expected between R^{obs} and R^{exp} as the average P_{th}

of each bin increases according to following relation [70]:

$$R^{\text{obs}} = B + R^{\text{exp}} = B + (1 - \sin^2(2\theta_{13})\eta_{\text{osc}})R^{\nu} \tag{3.19}$$

where R^{ν} is the expected rate of anti-neutrinos if there is no oscillation and η_{osc} is the average disappearance coefficient $\langle \sin^2(\Delta m^2 L/4E) \rangle$. As the disappearance coefficient is a function of the distance L between each reactor and the detector, whose average varies depending on which reactor is running with which P_{th}, a dedicated simulation is run to evaluate the coefficient for each of the data points. Fitting the data points with the relation described in Equation 3.19 allows a direct measurement of $\sin^2(2\theta_{13})$ and the BG.
Three sources of systematic uncertainty are included in the fit as nuisance parameters. The IBD detection efficiency $\sigma_d = 0.6\%$, as described in Section 3.6. The uncertainty due to residual $\overline{\nu}_e$'s produced after a reactor has been turned off but whilst β-decays are still taking place is $\sigma_{\nu} = 30\%$. Lastly, the prediction of the reactor flux in the reactor on data σ_r which depends on the reactor power, ranging from 1.76 % at maximum to 1.91 % when one or both reactors are not operating at maximum power.
The χ^2 of the Reactor Rate Modulation (RRM) fit is defined as follows [14]:

$$\chi^2_{RRM} = \chi^2_{\text{on}} + \chi^2_{\text{off}} + \chi^2_{\text{bg}} + \frac{\varepsilon^2_{\text{d}}}{\sigma^2_{\text{d}}} + \frac{\varepsilon^2_{\text{r}}}{\sigma^2_{\text{r}}} + \frac{\varepsilon^2_{\nu}}{\sigma^2_{\nu}} \tag{3.20}$$

$$\chi^2_{\text{on}} = \sum_{i=1}^{6} \frac{(R^{\text{obs}}_i - R^{\text{exp}}_i - B)^2}{(\sigma^{\text{stat}}_i)^2} \tag{3.21}$$

$$\chi^2_{\text{off}} = 2\left[N^{\text{obs}}_{\text{off}} \ln\left(\frac{N^{\text{obs}}_{\text{off}}}{N^{\text{exp}}_{\text{off}}} \right) + N^{\text{exp}}_{\text{off}} - N^{\text{obs}}_{\text{off}} \right] \tag{3.22}$$

$$\chi^2_{\text{bg}} = \frac{(B - B^{\text{exp}})^2}{\sigma^2_{\text{bg}}} \tag{3.23}$$

where R^{exp} is allowed to vary according to the systematic uncertainties described by ε_x and included in the last three terms in Equation 3.20. χ^2_{off} represents the period of data taking where both reactors were off and $N^{\text{exp}}_{\text{off}}$ and $N^{\text{obs}}_{\text{off}}$ correspond to the expected and observed number of IBD candidates respectively during that time period. As the statistics for the 2-off period are low, the error on N^{obs} is considered to follow the Poisson distribution and χ^2_{off} is described using the binned Poisson likelihood function. χ^2_{bg} represents the sum of the three BG rates and their uncertainties σ_{bg} measured in Section 3.5 to give $B = 1.64^{+0.41}_{-0.17}$ day^{-1}.
A χ^2 scan was carried out to find the minimum with respect to the systematic uncertainty parameters and the BG rate to gave the best fit for $\sin^2(2\theta_{13}) = 0.90^{+0.034}_{-0.035}$. The uncertainty is defined as $\chi^2 < \chi^2_{\text{min}} + 1$ with $\chi^2_{\text{min}}/d.o.f = 4.2/6$. The BG rate at the minimum χ^2 was

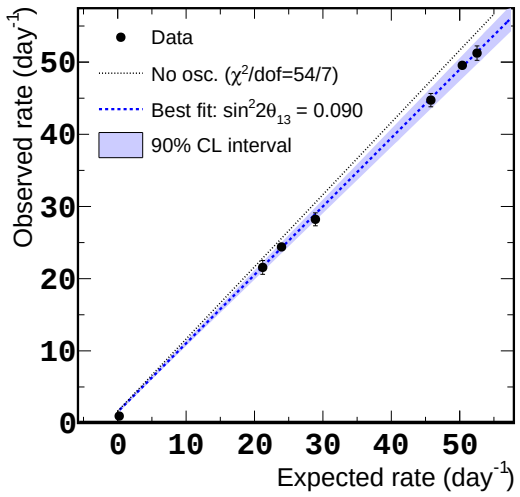

(a) The black data points represent the observed $\overline{\nu}_e$ rate against the expected rate where the data has been separated into seven bins according to the total reactor thermal power from the two reactors. The black dashed line represents the expectation if there is no oscillation and the blue dashed line represents the best RRM fit results. In this plot the BG was constrained according to the measured rates and uncertainty.

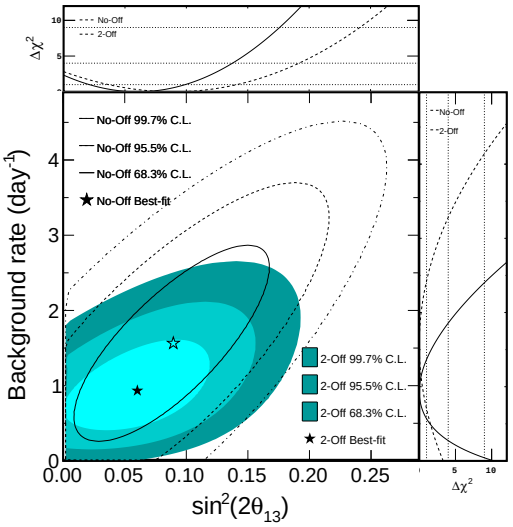

(b) The values for $\sin^2(2\theta_{13})$ and B at the minimum χ^2_{RRM} along with their corresponding 68.3, 95.5 and 99.7 % confidence limits with (coloured contours) and without (black lines) the reactor off data. In both cases the BG was unconstrained.

Figure 3.13 Results from the RRM fit. Source: [14]

$B = 1.56^{+0.18}_{-0.16}$ day^{-1}. Figure 3.13a shows the observed rate against the expected rate described by the best fit value of $\sin^2(2\theta_{13})$ along with the result in the no-oscillation scenario.

To check the validity of the results the total χ^2 is minimised using different configurations. First, the BG constraint is removed by taking away the χ^2_{bg} term from the fit. The minimum was found at $\chi^2/d.o.f = 1.9/5$, $\sin^2(2\theta_{13}) = 0.060 \pm 0.039$ and $B = 0.93^{+0.43}_{-0.36}$ day^{-1}. In the final configuration, the reactor off term χ^2_{off} was removed, along with the BG constraint to show the impact of the reactor off data to the precision of the $\sin^2(2\theta_{13})$ measurement. The best fit returned $\chi^2/d.o.f = 1.3/4$, $\sin^2(2\theta_{13}) = 0.089 \pm 0.052$ and $B = 1.56 \pm 0.86$ day^{-1}. Figure 3.13b shows the $\sin^2(2\theta_{13})$ and B plane with the two results just mentioned. Also shown are the 68.3, 95.5 and 99.7 % confidence limits with (coloured contours) and without (black lines) the reactor off data. The precision on $\sin^2(2\theta_{13})$ is significantly improved using the constraint from the reactor off data, something unique to the DC experiment.

3.7.2 Rate and Shape

The prompt E_{vis} of the IBD coincidence is directly related to E_ν/L and as such its spectral information can also be included in the $\sin^2(2\theta_{13})$ fit. Normally the spectral shape and rate of each bin gathered from the far detector can be compared to a reference spectrum taken using a detector with a smaller baseline L and as a result a smaller $P(\overline{\nu}_e \to \overline{\nu}_{\mu,\tau})$. For the publication currently being discussed only far detector data was available. As a result, the un-oscillated reference spectra is given by MC whose generation is described in Section 3.1. A direct comparison of the data and MC prompt spectra, which is generated without oscillation can be done in the fit construction where varying $\sin^2(2\theta_{13})$ will change the prompt spectral shape. The χ^2 is constructed as follows [67]:

$$
\begin{aligned}
\chi^2 = & \sum_{i=1}^{40}\sum_{j=1}^{40}(N_i^{\text{obs}} - N_i^{\text{exp}})M_{ij}^{-1}(N_j^{\text{obs}} - N_j^{\text{exp}}) \\
& + \frac{(\Delta m^2 - \Delta m^2_{ee})^2}{\sigma^2_{ee}} + \frac{(\alpha_r - 1)^2}{\sigma_r^2} \\
& + \frac{(\alpha_{\beta\text{-n}} - 1)^2}{\sigma^2_{\beta\text{-n}}} + \frac{(\alpha_{\text{FN+SM}} - 1)^2}{\sigma^2_{\text{FN+SM}}} + \frac{(\alpha_{\text{acc}} - 1)^2}{\sigma^2_{\text{acc}}} \\
& + \left(a' - a'_{CV}, b' - b'_{CV}, c' - c'_{CV}\right)
\begin{pmatrix}
\sigma^2_{a'} & \rho_{a'b'}\sigma_{a'}\sigma_{b'} & \rho_{a'c'}\sigma_{a'}\sigma_{c'} \\
\rho_{a'b'}\sigma_{a'}\sigma_{b'} & \sigma^2_{b'} & \rho_{b'c'}\sigma_{b'}\sigma_{c'} \\
\rho_{a'c'}\sigma_{a'}\sigma_{c'} & \rho_{b'c'}\sigma_{b'}\sigma_{c'} & \sigma^2_{c'}
\end{pmatrix}^{-1}
\begin{pmatrix}
a' - a'_{CV} \\ b' - b'_{CV} \\ c' - b'_{CV}
\end{pmatrix} \\
& + 2\left[N_{\text{off}}^{\text{obs}} \ln\left(\frac{N_{\text{off}}^{\text{obs}}}{N_{\text{off}}^{\text{exp}}}\right) + N_{\text{off}}^{\text{exp}} - N_{\text{off}}^{\text{obs}}\right]
\end{aligned}
\tag{3.24}
$$

where in the first term N_i^{obs} and N_i^{exp} refers to the observed and expected number of events respectively in the ith energy bin, of which there are 40 ranging from 0.5 MeV to 20 MeV. The expected number of events in bin i is defined as follows:

$$
\begin{aligned}
N_i^{\text{exp}} = & \sum_{R=1,2} N_i^{\overline{\nu},R}(\sin^2 2\theta_{13}, \Delta m^2, a', b', c') \\
& + N_i^{\beta\text{-n}}(\alpha_{\beta\text{-n}}) \\
& + N_i^{\text{FN+SM}}(\alpha_{\text{FN+SM}}) \\
& + N_i^{\text{acc}}(\alpha_{\text{acc}})
\end{aligned}
$$

where $N_i^{\overline{\nu},R}$ is the prediction from the MC taken as the sum over both reactors R and includes the spectral components from the BG prediction $N_i^{BG}(\alpha_{BG})$ where BG corresponds to the β-n, fast neutron and stopping muon (FN+SM) and accidental (acc) BG. The BG components are also a function of α_{BG}, included in the nuisance parameters which make up the second, third and fourth lines of Equation 3.24. Nuisance parameters allow the input parameters to vary, such as BG rates, according to their estimated uncertainty. As the input value deviates from its estimated value, the nuisance parameter goes from contributing zero to increasing the χ^2 by a factor proportional to the deviation and controlled by its measured uncertainty. However, the net result could be an improvement in the total χ^2 due to the corresponding change in N^{exp}.

The first nuisance parameter corresponds to the uncertainty on the mass squared difference $\Delta m^2 = 2.44^{+0.09}_{-0.10} \times 10^{-3}\,\text{eV}^2$, which assumes normal hierarchy and is derived from the MINOS measurement [71]. The second nuisance parameter refers to the number of residual $\overline{\nu}_e$'s during the period where both reactors were off ($1.57 \pm 0.4\,\text{day}^{-1}$) and the following three refer to the BGs already mentioned. The final nuisance parameter corresponds to the energy scale. The last term in Equation 3.24 corresponds to the data taking period where both reactors were off. As the corresponding amount of time, 7.24 days, is small, so too is the number of events. This means that the uncertainty may not follow a Gaussian distribution and as such a log-likelihood approach based on the Poisson distribution is used.

M_{ij} corresponds to the sum of covariance matrices representing the spectral uncertainties and is comprised of:

$$M_{ij} = M_{ij}^{\text{stat}} + M_{ij}^{\text{flux}} + M_{ij}^{\text{eff}} + M_{ij}^{\beta\text{-n(shape)}} + M_{ij}^{\text{acc(stat)}} \tag{3.25}$$

where M_{ij}^{stat} and $M_{ij}^{\text{acc(stat)}}$ are diagonal matrices corresponding to the statistical uncertainty from the IBD candidates and the statistical component of the accidental BG rate uncertainty. M^{flux} contains the uncertainty on the reactor $\overline{\nu}_e$ flux, $M_{ij}^{\text{eff}} = \sigma_{\text{eff}}^2 N_i^{\text{exp}} N_j^{\text{exp}}$ accounts for the uncertainty on the MC normalisation where $\sigma_{eff} = 0.6\%$ and $M_{ij}^{\beta\text{-n(shape)}}$ accounts for the shape uncertainty on the β-n spectrum.

A scan of χ^2 was carried out with respect to $\sin^2(2\theta_{13})$ and the other eight fit parameters. The minimum was found at $\chi^2_{\text{min}}/d.o.f = 52.2/40$ with $\sin^2(2\theta_{13}) = 0.090^{+0.032}_{-0.029}$ where the error is defined by the range $\chi^2 < \chi^2_{\text{min}} + 1.0$. Assuming inverted hierarchy where $|\Delta m^2| = 2.38^{+0.09}_{-0.10} \times 10^{-3}\,\text{eV}^2$ the best fit was found at $\sin^2(2\theta_{13}) = 0.092^{+0.033}_{-0.029}$ with $\chi^2_{\text{min}}/d.o.f = 52.2/40$. Figure 3.14 shows the prompt energy spectrum of the IBD candidates, along with the the BG components, the predicted spectrum oscillated according to the best fit value of $\sin^2(2\theta_{13})$ shown in red and the un-oscillated prediction shown in

blue. Figure 3.15 shows the ratio of the BG subtracted data and the best fit prediction to the no-oscillation prediction. The deficit of events below 4 MeV shows that a loss in the number of anti-neutrinos due to oscillation effects is present. The excess between 4 MeV and 6 MeV is thought to arise from the modelling of the decay branches in the reactor, however its impact on the measurement of $\sin^2(2\theta_{13})$ is minimal as the best fit value matches that from the RRM analysis in Section 3.7.1 and the cross checks described next.

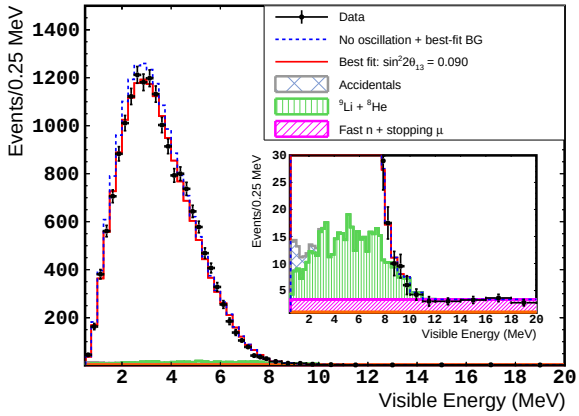

Figure 3.14 The prompt energy spectrum of the IBD candidates (black points) with the $\overline{\nu}_e$ prediction in the absence of oscillation (blue dashed line) and the results of the best fit oscillated spectrum (red line). Also shown are the three dominant BG spectra, accidentals (grey cross-hatched), fast n and stopping μ (pink slanted hatching) and β-n (green vertical lines). Source [14]

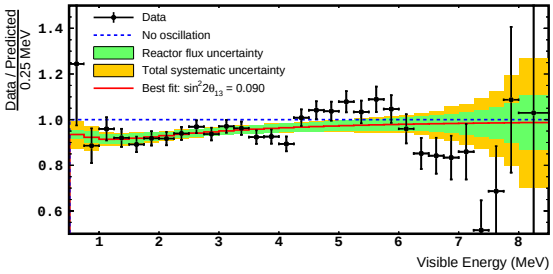

Figure 3.15 The black data points depict the ratio of the BG subtracted data with the no-oscillation prediction. The red line shows the ratio of the best fit spectrum with the no-oscillation prediction and the no-oscillation prediction itself is shown as a blue dashed line at unity. The green area represents the uncertainty due to the reactor flux and the yellow area the total systematic uncertainty. Source [14]

To cross check the validity of the results, the BG rates for the β-n and the correlated BGs were left unconstrained in the fit and the minimum value of $\chi^2 = 46.9/38$ was found at

$\sin^2(2\theta_{13}) = 0.088^{+0.030}_{-0.031}$ giving a β-n rate of $0.49^{+0.16}_{-0.14}\text{day}^{-1}$ and a correlated BG rate of $0.541^{+0.052}_{-0.048}\text{day}^{-1}$ where the errors on the BG rates are defined by the range $\chi^2 < \chi^2_{\text{min}} + 1$. A further cross check was carried out by ignoring any energy information and only comparing the total observed rate to the prediction, called the rate only fit, giving a best fit value of $\sin^2(2\theta_{13}) = 0.090^{+0.036}_{-0.037}$. All measurements of $\sin^2(2\theta_{13})$ are consistent with one another.

Hydrogen Analysis

Following on from the θ_{13} analysis using delayed neutron capture on Gd, the same data taking period was used to obtain a statistically separate sample of IBD candidates by searching for delayed neutron capture on H[46]. Although there are many similarities in the analysis techniques applied, there are also some new methods such as the pulse shape analysis and an artificial neural network which have increased the signal to BG ratio of IBD candidates by a factor of ten in comparison to a previous publication [45]. The live time in this analysis is 462.72 days and is smaller than the Gd analysis as the muon dead time is longer.

3.8 Background Reduction

3.8.1 Artificial Neural Network

Both the Gd IBD selection described earlier in this chapter and a previous publication of the θ_{13} analysis using a sample of H IBD candidates optimised cuts based on individual variables [45]. Instead, a multivariate approach can be used where multiple variables are used simultaneously to distinguish between IBD and BG events, which in this case consists mainly of accidentals. This was achieved by training an Artificial Neural Network (ANN) with a sample of IBD candidates generated statistically independently of the sample used for the θ_{13} analysis and a pure sample of accidental events selected using an off-time window. The three variables used in the ANN were the time difference between the prompt and delayed events ΔT, the distance between them ΔR and the delayed visible energy E_d. Figure 3.16a shows the output value from the ANN based on the three input variables, where the accidental BG is shown as a red line, the blue line represents the signal MC, the black line represents data and the black points represent the data after subtraction of the accidentals. Moving upwards from the lowest ANN output value of -1.2, the ANN initially selects mostly accidentals and then predominantly IBD candidates. An ANN output value cut of

ANN≥ -0.23 was applied to the IBD data giving a signal efficiency of 80 % and a signal to accidental BG ratio of 9.2. This is a great improvement compared to the previous publication [46] where the ratio was 0.91 with an efficiency of 85 %. Figure 3.16b shows the prompt

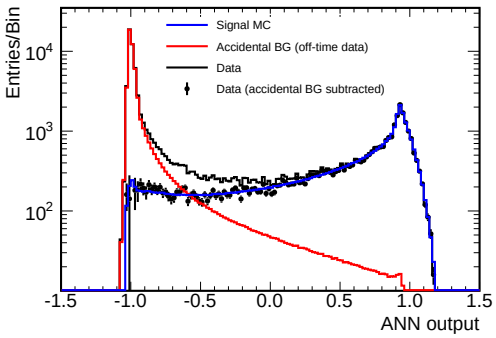

(a) The output value from the ANN based on the three input variables, where the accidental BG is shown as a red line, the blue line represents the signal MC, the black line represents data and the black points represent the data after subtraction of the accidentals. Larger values of the ANN output are more likely to be an IBD event.

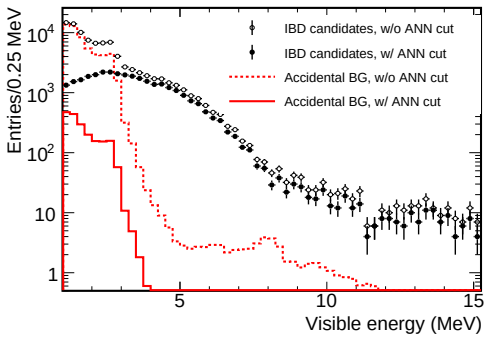

(b) The prompt energy spectrum of the IBD candidates from data without the ANN cut (black hollow circles), with the data (black filled circles) and the accidental BG without the ANN cut (red dashed line) and with the ANN cut (red line). A clear reduction in accidentals is observed in the IBD sample.

Figure 3.16 The plot on the left shows the IBD MC, accidentals, and data with and without BG subtraction as a function of the ANN output. The plot on the right shows the visible energy spectra with and without the ANN cut. Source: [46]

energy spectrum of the IBD candidates from data without the ANN cut (black hollow circles), with the data (black filled circles) and the accidental BG without the ANN cut (red dashed line) and with the ANN cut (red line). An obvious reduction of accidental events within the IBD data sample is observed.

3.8.2 IV Veto

The IVV uses the same principle described in Section 3.4.3 but with a few adaptations to suit the H data. In the Gd analysis, the IVV was only applied to the prompt event, in the H analysis it is applied to both the prompt and the delayed events which are removed if they pass the following criteria:

- IV PMT multiplicity ≥ 2
- $Q_{\mathrm{IV}} > 400$ CU ≈ 0.2 MeV

- $\Delta d_{\text{ID-IV}} < 4\,\text{m}$
- $0\,\text{ns} < \Delta T_{\text{ID-IV}} < 90\,\text{ns}$

Compared to the IVV used in the Gd analysis the distance has been increased from 3.7 m and the time difference shortened to 90 ns.

3.8.3 Functional Value Veto

The principle behind the F_{V} BG rejection has already been described in Section 3.8.3. Equation 3.17 describes the cut used and the parameters A and B need to be re-evaluated using the H IBD sample. The value for B, or the slope of the line is taken such that it has the same slope as a pure sample of Michel electrons, selected using prompt event coincidence with the OV. This gives a value of $B = 2.0125$. The value of A was found by systematically varying it, beginning at zero, and calculating the IBD inefficiency for each cut. To maximise BG rejection, the minimum for the IBD inefficiency divided by the number of rejected stopping muons is found at $A = 0.2755$.

3.8.4 Multiplicity Pulse Shape

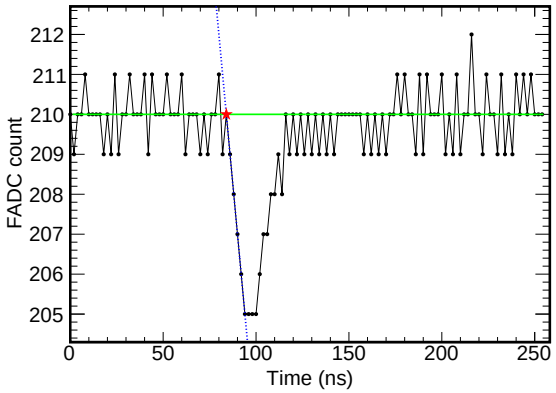

Figure 3.17 A typical PMT waveform and estimation of its start time. The pedestal is shown here as a green line, the blue line is a fit to the leading edge and their intersection, shown by the red star is the pulse start time. Source [46]

The PMT waveforms can be used to identify FN interactions. A few PMTs may observe FN induced proton recoil before the main cluster of pulses from the FN interaction are observed. Figure 3.17 shows the start time identification of each waveform. The green line represents the pedestal evaluated using non event like triggers and a signal is identified when the FADC

count drops below the pedestal by two FADC units. A linear fit is performed to the leading edge, shown in the figure by the blue line and the interception between them, shown by a red star is used as the pulse start time. The Pulse Shape (PS) is defined as the distribution of the start times for all PMTs. The start times are corrected for the time of flight from the event's reconstructed position and variations between PMTs for the time the signal takes to traverse the cable.
The PS is fitted with a Gaussian centred around the mean m_{PS} with a characteristic width σ_{PS}. The initial position, or shift value of the PS is calculated as the point $\mathrm{PS}_{shift} = m_{\mathrm{PS}} - 1.8 \cdot \sigma_{\mathrm{PS}}$. Examples of different PS distributions are shown in Figure 3.18 where PS_{shift} is shown as a red line alongside the best fit Gaussian. Figure 3.18a shows a typical IBD candidate and Figure 3.18b shows a typical FN interaction with a larger PS shift. Figure 3.18c shows a bound state of a positron and electron called ortho-positronium. The first peak corresponds to the ionisation energy and the second to the annihilation of the two γ's which is fixed at 1.022 MeV. Prompt events with $E_{\mathrm{vis}} > 3\,\mathrm{MeV}$ and $\mathrm{PS}_{shift} > 5\,\mathrm{ns}$ are rejected as FNs. Prompt events with $1.2 < E_{\mathrm{vis}} < 3\,\mathrm{MeV}$ and $\mathrm{PS}_{shift} > 5\,\mathrm{ns}$ which aren't identified as ortho-positronium are also rejected as FN. These cuts were found to have an IBD selection efficiency of 100 % and reduced the FN BG by 25 %.

3.9 IBD Inefficiency

As already described in Section 3.9, the correction factors shown in Table 3.3 are applied to the MC sample bringing it in line with the data. Most of the corrections have already been explained, however there are two extra values listed for the inefficiency which correct for the MPS and ANN cuts. The *n* detection combines the H fraction, spill in/out and neutron selection factors into one. An explanation of the $\mathscr{L}_{\mathrm{Li}}$ veto IBD inefficiency estimation can be found in Section 4.6.2. The final MC correction factor is 0.929 ± 0.01.

3.10 Background Measurements

3.10.1 Accidentals

Accidentals occur when two uncorrelated events, both pass the prompt and delayed selection criteria. As the neutron capture energy on H is much lower than Gd, the accidental rate is much larger in the H sample. This also means that fewer off-time windows are needed to estimate the rate and prompt spectrum. Two hundred windows were offset by 1 s and corrections are made to the rate to account for the finite run length, muon veto and

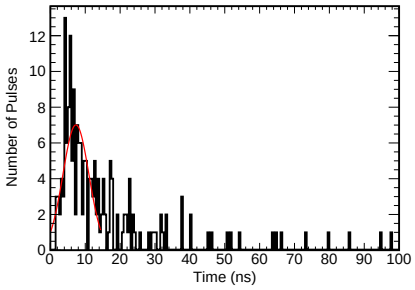

(a) The PS of an IBD candidate.

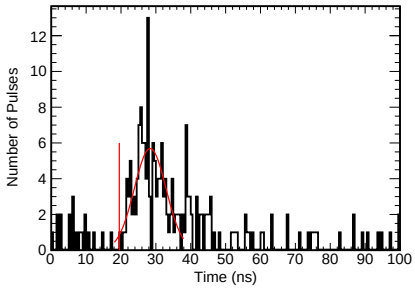

(b) The PS of proton recoils from FN and subsequent neutron capture.

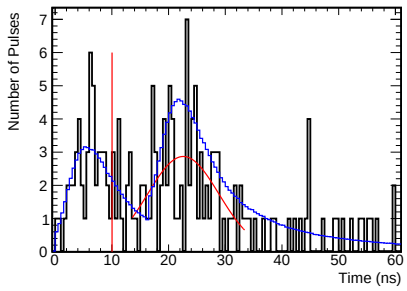

(c) The PS of an ortho-positronium IBD event.

Figure 3.18 Examples of PS from different events used to reject FNs from the IBD sample. Source [46]

multiplicity which affect the on-time windows differently then the off-time windows. This leaves an accidental BG rate of $4.334 \pm 0.007(stat) \pm 0.008(syst)\,\text{day}^{-1}$.

3.10.2 Cosmogenic Isotopes

The β-n BG rate is $2.58^{+0.57}_{-0.32}\,\text{day}^{-1}$ before applying the $\mathscr{L}_{\text{Li}}$ veto. The rate attributed to the $\mathscr{L}_{\text{Li}}$ veto is $1.63 \pm 0.06\,\text{day}^{-1}$, leaving a final β-n rate of $0.95^{+0.57}_{-0.33}\,\text{day}^{-1}$.
A detailed explanation of the analysis can be found in Chapter 4.

3.10.3 Correlated Background

The FN component of the correlated BG is obtained by separating the shape and the rate measurement. The shape of the FNs is evaluated by selecting a pure sample using an adapted IVV selection. The IVV is modified to remove any accidental events which may contaminate the FN spectrum. This is achieved by increasing the minimum IV charge, and decreasing the

Table 3.3 The IBD through neutron capture on Hydrogen MC correction factors and their uncertainties due to selection, detection and veto inefficiencies. From [46]

	MC correction	Uncertainty (%)
Muon veto	0.9400	< 0.01
LN cuts	0.9994	< 0.01
ANN cut	1.0000	0.220
Multiplicity cut	0.9788	< 0.01
Li+He veto	0.9949	0.012
FV veto	0.9995	0.015
OV veto	0.9994	< 0.01
IV veto	1.0000	0.169
MPS cut	1.0000	0.100
n detection	1.0000	0.42
Proton number	1.0022	0.950
Total	0.929	1.0

maximum time difference and the range of distances allowed between the two. The FN spectrum is obtained using the following cuts on the prompt IBD candidates:

- IV PMT multiplicity ≥ 2
- $Q_{\text{IV}} > 6 \cdot 2200\,\text{CU} \approx 6\,\text{MeV}$
- $1.1\,\text{m} < \Delta d_{\text{ID-IV}} < 3.5\,\text{m}$
- $0\,\text{ns} < \Delta T_{\text{ID-IV}} < 60\,\text{ns}$

The prompt energy spectrum is extended up to 60 MeV to allow for an analysis of the spectral shape. Unlike the Gd analysis, the best fit came from an exponential plus flat component described by $N = p_0 \cdot \exp(-p_1 \cdot E_{vis}) + p_2$ where $p_0 = 12.52$, $p_1 = 0.42$ and $p_2 = 0.79$. The spectrum between 20 MeV and 60 MeV is estimated to be a pure FN sample and is used to calculate the tagging efficiency of the FN selection criteria just described. The tagging efficiency was measured by comparing the number of tagged FN events to the number of IBD events in this prompt energy region giving $23.6 \pm 1.5\%$. The spectral shape is corrected using this efficiency to give a total FN rate of $1.55 \pm 0.15\,\text{day}^{-1}$. Figure 3.19 shows the prompt spectrum of the IBD candidates as black points. The red points represent the FN background component whose shape is from the IVV selection mentioned here and has been corrected to compensate for the tagging efficiency. The red line shows the best fit function.

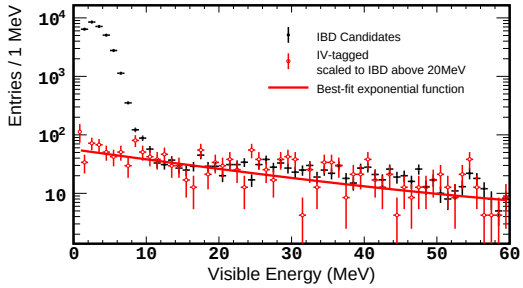

Figure 3.19 The prompt spectrum of the IBD candidates is shown by black points. The red points represent the FN BG component whose shape is from the IVV selection mentioned in this section, corrected for the tagging efficiency. The red line shows the best fit function. Source [46]

The SM contamination in the IBD sample was evaluating using the PS of events. SMs are falsely reconstructed below their actual position in the chimney. If the PS time of flight is corrected using a position in the chimney instead of the position given by the standard position reconstruction algorithm, the PS of SMs resemble those from a source deployment of ^{60}Co. A comparison of the likelihood using the normal PS to one corrected as if it were in the chimney allows a pure sample of SMs to be selected from the IBD sample, giving an estimated SM rate of $0.02\,\mathrm{day}^{-1}$. This is included in the FN rate.

3.11 Neutrino Oscillation Analysis for θ_{13}

The publication of the Gd results showed a peak in the prompt IBD spectrum between 4 MeV and 6 MeV. The cause of this excess has not been fully understood. So instead of relying on a *Rate+Shape* fit for the measurement of $\sin^2(2\theta_{13})$, a method less sensitive to this excess is used which only compares the rate, the RRM. The *Rate+Shape* fit described later is used as a cross check of the RRM measurement.

3.11.1 Reactor Rate Modulation

The RRM analysis for the H IBD sample follows the same procedure as the Gd analysis in Section 3.7.1. The χ^2_{RRM} is defined in Equation 3.20 and the systematic uncertainties are the same for the H and the Gd analysis. The sum of the accidentals, cosmogenic isotopes and correlated BG described in Section 3.10 give the total $B = 6.83^{+0.59}_{-0.36}\,\mathrm{day}^{-1}$. The minimum χ^2_{RRM} with respect to $\sin^2(2\theta_{13})$, the three systematic uncertainty parameters and the constrained BG was found at $\sin^2(2\theta_{13}) = 0.098^{+0.038}_{-0.039}$ and $B = 7.29 \pm 0.48\,\mathrm{day}^{-1}$ with

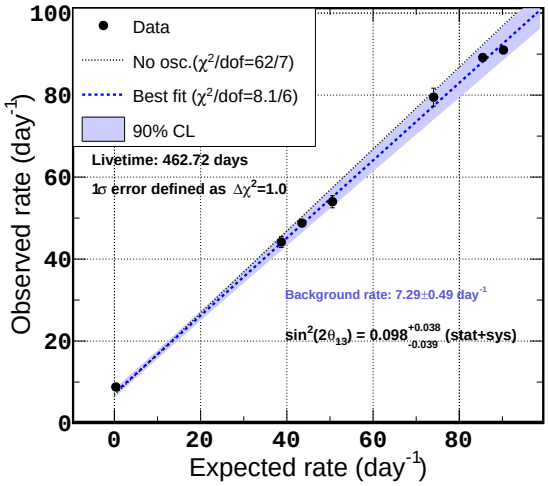

(a) The black data points represent the observed $\overline{\nu}_e$ rate against the expected rate where the data has been separated into seven periods according to the total reactor thermal power from the two reactors. The black dashed line represents the expectation if there is no oscillation and the blue dashed line represents the best RRM fit results. In this plot the BG was constrained according to the measured rates and uncertainty.

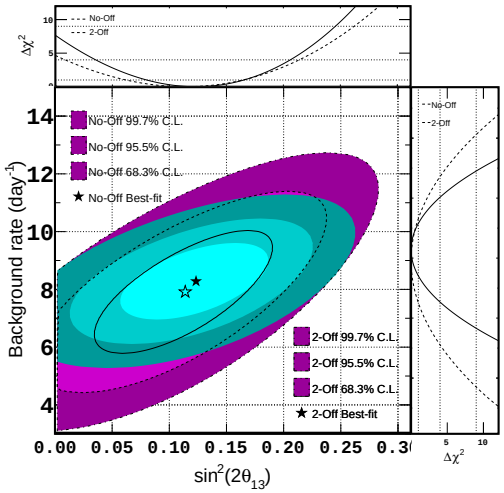

(b) The values for $\sin^2(2\theta_{13})$ and B at the minimum χ^2_{RRM} along with their corresponding 68.3, 95.5 and 99.7 % confidence limits with (coloured contours) and without (black lines) the reactor off data. In both cases the BG was unconstrained.

Figure 3.20 Results from the RRM fit. Source [46]

$\chi^2_{\text{min}}/d.o.f = 8.1/6$ where the uncertainty is defined in the region $\chi^2_{RRM} < \chi^2_{\text{min}} + 1$. Figure 3.20a shows R^{obs} against R^{exp} along with the no-oscillation hypothesis.

The RRM fit is carried out without constraining the total BG rate, in effect leaving B as a free parameter. A global scan is carried out with respect to $\sin^2(2\theta_{13})$ and B minimising χ^2 at each point with respect to the three systematic uncertainty parameters. The minimum was found at $\chi^2_{\text{min}}/d.o.f = 8.1/5$ where $\sin^2(2\theta_{13}) = 0.123^{+0.042}_{-0.043}$ and $B = 8.28 \pm 0.87\,\text{day}^{-1}$ consistent with the BG constrained result. Figure 3.20b shows a comparison of the best fit results for $\sin^2(2\theta_{13})$ when the BG is unconstrained with and without the 2-reactor off term.

3.11.2 Rate and Shape

The *Rate+Shape* analysis follows the same approach described in Section 3.7.2 with the χ^2_{R+S} defined in Equation 3.24. In the H analysis 38 bins are used instead of 40 due to an increase in the minimum visible energy required for the prompt event from 0.5 MeV to 1 MeV. The number of residual $\overline{\nu}_e$'s in the two reactora off period is 2.34 ± 0.7 events. The

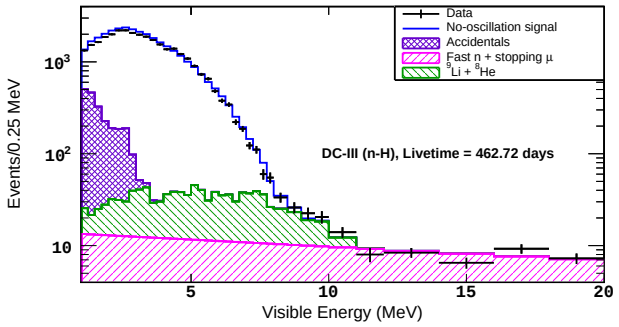

Figure 3.21 The prompt energy spectrum of the IBD candidates from data (black points) along with the no-oscillation prediction from MC (solid blue line). The BG contributions from the accidentals (purple cross hatching), β-n (green slanted hatching) and the correlated BG (pink slanted hatching) are also shown. Source [46]

χ^2_{R+S} is minimised with respect to $\sin^2(2\theta_{13})$ and the eight fit parameters. The best fit value is $\sin^2(2\theta_{13}) = 0.124^{+0.030}_{-0.036}$ with $\chi^2_{\text{min}}/d.o.f = 69.5/38$ where the uncertainty is defined by the region $\chi^2 < \chi^2_{\text{min}} + 1$. The large value for the χ^2_{R+S} is given by the spectral distortion between 4.25-5.75 MeV. If the six energy bins and their correlations corresponding to this region are removed from the fit a χ^2_{R+S} of 30.7/32 is found.

Gadolinium and Hydrogen Combined

3.11.3 Reactor Rate Modulation

A combined fit of the Gd and H IBD candidates is carried out, where following on from the H analysis the RRM approach is applied. The shape, or energy dependence is not included in the fit due to the spectrum distortion observed in both data sets. Full correlation was assumed between the uncertainties of the reactor flux and residual neutrinos in the two reactor off periods between the data sets. The BG estimates used in the fit were assumed to be fully uncorrelated, assuming correlation between them showed a negligible difference in the best fit result. The best fit was found at $\sin^2(2\theta_{13}) = 0.090 \pm 0.033$ with $\chi^2_{\text{min}}/d.o.f = 12/13$. Figure 3.23a shows R^{obs} against R^{exp} as black points for both the Gd (triangle) and H (circle) IBD candidates with the best fit result shown as a black dashed line. Figure 3.23b shows the best fit value for $\sin^2(2\theta_{13})$ and the constrained BG with the corresponding 68.3, 95.5 and 99.7 % confidence limits.

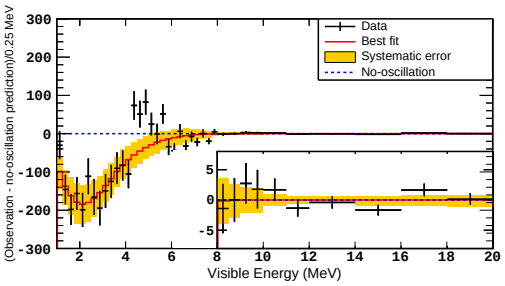

(a) The difference between the prompt energy spectra of the IBDs from data and the no-oscillation hypothesis. The deficit due to oscillation and excess at roughly 5 MeV are visible.

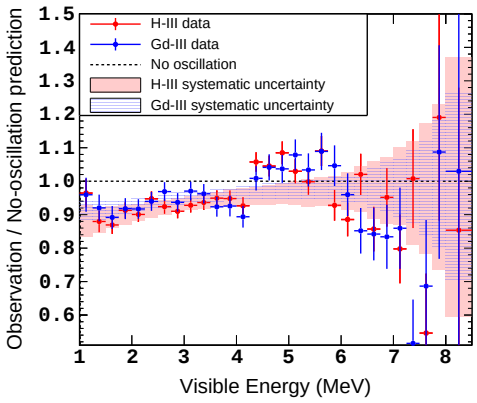

(b) The ratio of the prompt visible energy from data and the no-oscillation hypothesis. The H data is represented by red points whilst the Gd is represented by blue points. The excess at 5 MeV is visible in both.

Figure 3.22 A comparison of the prompt visible energy spectra between data and the no-oscillation hypothesis. Source [46]

3.12 Summary

The data set from April 2011 to January 2013 has been used to measure $\sin^2(2\theta_{13})$ using IBD candidates where the neutron is captured on either Gd or H. The measurement using the H-channel only of $\sin^2(2\theta_{13}) = 0.098^{+0.038}_{-0.039}$ is remarkable compared to the measurement using the Gd-channel of $\sin^2(2\theta_{13}) = 0.90^{+0.034}_{-0.035}$. The uncertainties are only slightly worse, which is impressive because DC was designed as a precision detector of the Gd-channel. Even more impressive is the BG reduction in the H-channel compared to the previous publication where the ANN has reduced the accidentals rate from $73.45 \pm 0.16\,\text{day}^{-1}$ to $4.33 \pm 0.01\,\text{day}^{-1}$. Novel BG reduction techniques such as this, and the PS have improved the signal to BG ratio by a factor of ten. As the near detector is currently taking data, a measurement of $\sin^2(2\theta_{13})$ using both detectors will take place in the near future significantly improving the uncertainty. The signal from the H sample is now clean enough that it can be combined with Gd data set using both detectors to further increase the statistics and measurement of $\sin^2(2\theta_{13})$.

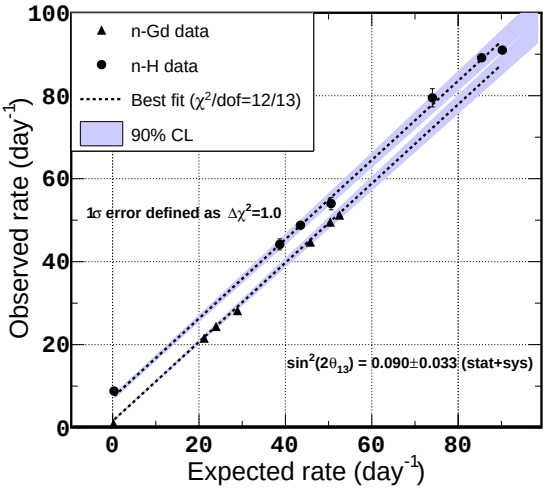

(a) The black points for Gd (triangles) and H (circles) represent the observed versus expected $\overline{\nu}_e$ rate where the data has been separated into seven periods according to the total reactor thermal power from the two reactors. The black dashed line represents the expectation if there is no-oscillation and the blue dashed line represents the best RRM fit results.

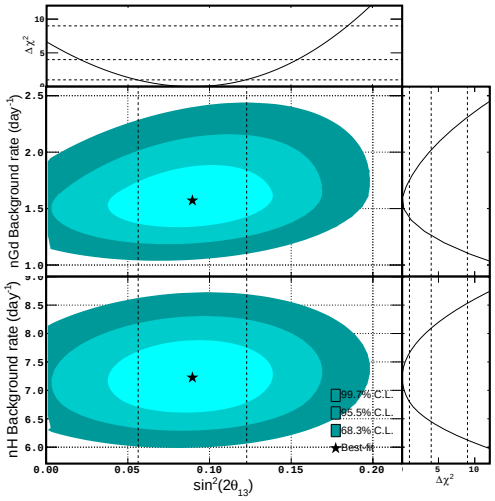

(b) The values for $\sin^2(2\theta_{13})$ and B at the minimum χ^2_{RRM} along with their corresponding 68.3, 95.5 and 99.7 % confidence limits with (coloured contours) and without (black lines) for both the Gd and H data samples.

Figure 3.23 Results from the combined Gd and H RRM fit where the BG has been constrained to the measured values and uncertainties. Source [46]

Part II

Cosmogenic Background Measurement

Chapter 4

Cosmogenic β-n Background Measurement in the Hydrogen IBD Sample

Chapter 3 describes the analysis approach to measuring the value of $\sin^2(2\theta_{13})$ using two IBD samples from delayed neutron capture on Hydrogen and Gadolinium. Great care has been taken to estimate the BG rates and their corresponding uncertainties contaminating these samples as they are important input parameters to the $\sin^2(2\theta_{13})$ fit. This chapter explains the methods used to estimate the rate of β-n emitters remaining in the IBD Hydrogen capture sample. β-n emitters are only observed when ^{9}Li and ^{8}He, produced through cosmic muon spallation, decay to excited states of the daughter nucleus. The total rate $\mathscr{R}_{\beta n}^{\text{tot}}$ is calculated first, after which the number of events removed by the $\mathscr{L}_{\text{Li}}$ veto $\mathscr{R}_{\beta n}^{\text{veto}}$ is subtracted to give the final rate $\mathscr{R}_{\beta n}^{\text{fit}}$ used as input to the $\sin^2(2\theta_{13})$ fit explained in Section 3.11. I have taken inspiration from the methods used to estimate the β-n rate in the Gadolinium channel described in Chapter 3.5.3 and [14].

4.1 Introduction

The cosmogenic isotopes ^{9}Li and ^{8}He are both created by muon spallation on ^{12}C nuclei present in the organic liquid scintillator, where the main creation processes are $^{12}\text{C}(\pi^-,{}^3\text{He})^9\text{Li}$ and $^{12}\text{C}(\pi^-,n3p)^8\text{He}$ [72]. ^{9}Li and ^{8}He are together often called β-n emitters as even though they always undergo β-decay, on the occasion that this isn't directly to the ground state of the daughter nucleus, a neutron is subsequently emitted, happening for

49.5 % and 16 % of the ^{9}Li and ^{8}He decays respectively[1]. This double coincidence imitates the IBD signal and the only distinguishing feature, except for the overall difference in prompt spectral shape, is the correlation in distance and time to the parent muon.
As the lifetimes of ^{9}Li and ^{8}He, 257 ms and 172 ms respectively are long in comparison to the average time between two muons in the ID, roughly 63 ms, it is not feasible to apply a simple dead time with a length on the order of a few lifetimes after each muon. Instead, the β-n contamination in the IBD sample is estimated using the distribution of differences in time between the prompt event and the muon, where the uncertainty on this measurement is reduced using knowledge of the distance distribution between the two.

4.2 Time Distribution Fit Function

The β-n rate is estimated using the time distribution of all prompt IBD candidates and prior muons, where the time difference between the two is denoted by $\Delta T_{p\text{-}\mu}$. $\mathscr{R}_{\beta\mathrm{n}}$ is used to refer to the β-n rate estimate from a fit to a single $\Delta T_{p\text{-}\mu}$ distribution or histogram. The expected distribution is the sum of two exponentials following the lifetimes of the cosmogenic isotopes ^{9}Li and ^{8}He, a constant BG component proportional to the muon rate and a correction factor due to the finite run length. To allow for an accurate estimate of the BG component in the $\Delta T_{p\text{-}\mu}$ distribution and therefore $\mathscr{R}_{\beta\mathrm{n}}$, all muons up to 20 s prior to the prompt event are included. The fit function is expressed in the following equation:

$$f(\Delta T_{p\text{-}\mu}) = \Delta B \cdot \left(\left(\mathscr{R}_{\beta\mathrm{n}} T_L \cdot \sum_{c}^{^{9}\mathrm{Li},^{8}\mathrm{He}} \frac{F_c}{CF_c} \frac{1}{\tau_c} \cdot e^{-\frac{\Delta T_{p\text{-}\mu}}{\tau_c}} \right) + R_\mu \cdot N_{\mathrm{IBD}} \right) \cdot \left(1 - \frac{\Delta T_{p\text{-}\mu}}{R_L} \right) \quad (4.1)$$

where ΔB is the bin width of the histogram to which the function is fitted, $\mathscr{R}_{\beta\mathrm{n}}$ is the β-n rate per day, T_L is the live time, CF is the correction factor, F_c is the ^{9}Li or ^{8}He fraction of the total where $F_{\mathrm{Li}} + F_{\mathrm{He}} = 1$, τ_c is the lifetime, R_μ is the muon rate per second, N_{IBD} number of IBD candidates and R_L is the run length which in Double Chooz is an hour.
There are only two free parameters in the fit, the β-n rate and the muon rate. The rest are user defined constants given by T_L = 462.72 days, R_L = 36×10^5 ms, $\tau_{\mathrm{Li}} = 257\,\mathrm{ms}$, $\tau_{\mathrm{He}} = 172\,\mathrm{ms}$ and $N_{\mathrm{IBD}} = 32830$ events. For the majority of the analysis, $\Delta B = 20\,\mathrm{ms}$, $F_{\mathrm{He}} = 0$ and the final two variables $ST = 1.25\,\mathrm{ms}$ and $ET = \infty$ which are used to calculate CF_c described in Section 4.2.3. Sometimes it is necessary when assessing the systematics to change parameters such as F_{He} and ΔB, which is why they have been included in the equation.

[1] For more information including the decay schemes see Chapter 6

4.2.1 Muon Rate Background

The flat BG component in Equation 4.1 is proportional to the muon rate. It is related to the number of entries in each bin, which we call C in the following manner:

$$C = R_\mu \Delta B \cdot N_{\text{IBD}} \tag{4.2}$$

The extra normalisation factor is because each $\Delta T_{p\text{-}\mu}$ histogram is filled a total of N_{IBD} times.

4.2.2 Number of Events in an Exponential Function

When an exponential function with a fixed lifetime is fitted to a histogram, the only free parameter is the normalisation constant, which we can call a given by $y = a \cdot e^{-\frac{t}{\tau}}$. a can be translated into the total number of events contained within the exponential by integrating the function from zero to infinity as follows:

$$\begin{aligned} N_c &= \int_0^\infty a \cdot e^{-\frac{t}{\tau_c}} \, \mathrm{d}t \\ &= a \cdot \tau_c \end{aligned} \tag{4.3}$$

where for simplification $\Delta T_{p\text{-}\mu}$ has been substituted with t and N_c is the number of decays corresponding to the cosmogenic isotope c. Equation 4.3 can be re-arranged so that $a = N_c/\tau_c$ and substituting $N_c = T_L \cdot \mathscr{R}_c$ to return the rate rather then the number of events gives the components in Equation 4.1.

4.2.3 Time Window Correction Factor

If CF_c is excluded from Equation 4.1, then it gives the total rate of β-n events for the period from zero to infinity as defined in Equation 4.3. CF_c corrects for the number of events required within a specific time window. In general it used to remove the number of β-n events which aren't observed due to the muon dead time. CF_c is given by the ratio of the exponent integral over the time window required to that of the whole period:

$$\begin{aligned} CF_c &= \frac{\int_{ST}^{ET} e^{-\frac{t}{\tau_c}} \, \mathrm{d}t}{\int_0^\infty e^{-\frac{t}{\tau_c}} \, \mathrm{d}t} \\ &= e^{-\frac{ST}{\tau_c}} - e^{-\frac{ET}{\tau_c}} \end{aligned} \tag{4.4}$$

where ST is the start time and ET is the end time of the window containing the required β-n emitters.

At first glance it seems that CF_c and ΔB are counter-intuitively placed, as the numerator and denominator respectively instead of vice versa. This is a consequence of the fit definition and can be explained as follows. For the exponential parts, the β-n rate would normally be extracted from the fit and then divided by ΔB and multiplied by CF_c. However, as the number of entries in each bin is constant, they have to be included inversely in the fit function to compensate correctly. The bin width needs to considered as for example doubling the bin width, would also on average double the number of events in each bin, falsely inflating the total number of events and therefore rate.

4.2.4 Fit Method

A package developed by CERN called ROOT [73] is used for data analysis including function fitting throughout this chapter. The $\Delta T_{p\text{-}\mu}$ histograms are fitted using the Binned Maximum Likelihood (BML) approach, minimising $-2\ln L$, as the histograms have Poisson statistical uncertainty distributions. A BML fit works better than a χ^2 fit when there are fewer entries in the bins, or when the Poisson distribution becomes non-Gaussian but gives the same results when the number of entries is large as then $-2\ln L \approx \chi^2$. The best fit result is defined by the point where $-2\ln L$ is at a minimum. The uncertainty on the free parameters is purely statistical and calculated using the $-2\ln L$ distribution, where contours of constant $-2\ln L$ cover true values with a certain probability. In the two parameter case the region between the minimum value of $-2\ln L$ plus 1.15 gives the one sigma uncertainty on the parameters [22].

4.3 Correlated Muon-like Events

In the case of the normal IBD analysis, all events within 1.25 ms of a vetoing muon described in Section 3.3.1 as $E^{\mu}_{\text{vis}} > 20\,\text{MeV}$ or $E_{\text{IV}} > 16\,\text{MeV}$ are ignored. This veto removes not only single events such as spallation neutron captures correlated to the muons, but also correlated events with a higher visible energy which fall into the vetoing muon category such as Michel electrons from muon decay and PMT ringing. In evaluating the β-n rate, muons that would normally be removed by vetoing muons need to be included in the analysis, so as not to miss any possible parent muons. At the same time, it is important that events correlated to a muon which pass the muon criteria, but aren't muons, are ignored in the analysis as this will cause double counting of β-n emitters, incorrectly inflating their measurement.

Muon events which have $E^{\mu}_{\text{vis}} > 20\,\text{MeV}$ are labelled μ and events which are defined in the same manner but whose only difference is that they occur after μ's are labelled μ'. To evaluate whether there is any contribution to the muon sample from correlated events, the time difference between μ' and μ denoted by $\Delta T_{\mu'\text{-}\mu}$ for all pairs was observed. Figure 4.1a shows the $\Delta T_{\mu'\text{-}\mu}$ distribution against the visible energy of μ', where the warmer colours represent larger content in the bin. At large $\Delta T_{\mu'\text{-}\mu}$'s, it is apparent that there is a flat distribution implying that in this region μ''s are not correlated to the previous muon. However, moving towards shorter $\Delta T_{\mu'\text{-}\mu}$'s a build up of events above the BG level looks like they could represent correlated events. The events below 55 MeV represent Michel electrons, where the first event μ is a detected stopping muon and μ' is the Michel electron decaying with a characteristic lifetime of 2.2 µs. For μ energies extending up to approximately 230 MeV there seems to be a second type of correlated event with a much shorter lifetime, which is most likely due to PMT ringing. This occurs when muons deposit large amounts of energy in the detector after which fake pulses are observed in the PMTs whose sum signal appears as a muon-like event μ'.

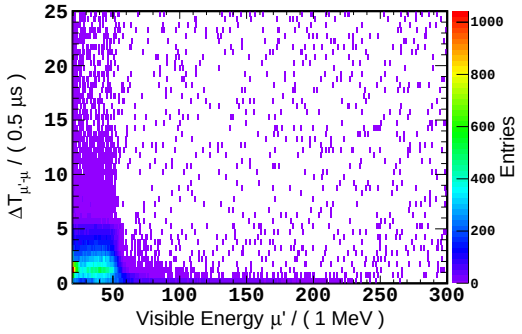

(a) Time difference between all pairs of muons versus the visible energy of the second "muon-like" event μ'. At small $\Delta T_{\mu'\text{-}\mu}$, the region below 55 MeV is dominated by Michel electrons correlated to their parent muon according to their lifetime 2.2 µs. Correlated μ' above this energy and extending to 230 MeV are most likely PMT ringing events caused by the first muon.

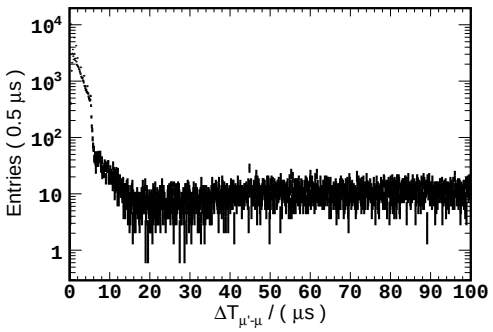

(b) Time difference between all pairs of muons for $\mu' < 250\,\text{MeV}$. The non-flat components at short $\Delta T_{\mu'\text{-}\mu}$ show correlation to the first muon. To remove these from our muon sample, a cut of 20 µs is applied after any muon removing only "muon-like" events with a visible energy less than 250 MeV.

Figure 4.1 Muon-like events μ' such as PMT ringing and Michel electrons are correlated to a previous muon μ. They are removed from the $\mathscr{R}_{\beta\text{n}}$ analysis by applying a dead time of 20 µs for μ' with a visible energy of less than 250 MeV after muons.

To cross check whether the excess at low $\Delta T_{\mu'\text{-}\mu}$ in Figure 4.1a actually represents correlated events, a one dimensional histogram representing $\Delta T_{\mu'\text{-}\mu}$ is shown in Figure 4.1b. Two

exponential components are clearly visible above the flat BG component. The first corresponds to the electrons from muon decay and the second is thought to be caused by PMT ringing. As a result, muon-like events within 20 µs of a muon and with a visible energy of less than 250 MeV are removed from the subsequent analysis.

4.4 Preliminary Total β-n Rate Estimate

To obtain a preliminary estimate for $\mathscr{R}^{\text{tot}}_{\beta\text{n}}$, the IBD candidates are selected using the criteria described in Chapter 3 following the criteria for delayed neutron capture on H. All vetoes are applied as described in the chapter except for the $\mathscr{L}_{\text{Li}}$ veto, whose treatment is dealt with separately in Section 4.6.1. The muons are separated into two groups, IV muons which only deposit energy in the IV selected by $E_{\text{vis}} < 20\,\text{MeV}$ and $E_{\text{IV}} > 16\,\text{MeV}$ and ID muons which deposit energy in the ID $E_{\text{vis}} > 20\,\text{MeV}$. The $\Delta T_{p\text{-}\mu}$ distributions of ID and IV muons are shown in Figure 4.2a and 4.2b respectively, where the standard bin width of 20 ms was used. They are both fitted with Equation 4.1 to estimate the β-n rate. Although the fit is applied to the distribution going back 20 s, only the first 2.5 s are shown. Muons which only pass through the IV were found to produce a $\mathscr{R}_{\beta\text{n}}$ equivalent to zero. This is because only muons which pass close to the fiducial volume are expected to generate ^{9}Li or ^{8}He.
A preliminary $\mathscr{R}^{\text{tot}}_{\beta\text{n}}$ is obtained in Figure 4.2a giving $\mathscr{R}^{\text{tot}}_{\beta\text{n}} = 2.99 \pm 1.16\,\text{day}^{-1}$. Although a good starting point, this gives a large error corresponding to 39 % of the total rate. The next section will deal with reducing this uncertainty.

4.5 Rate Estimate using Distance Distribution

The time correlation between the muon and prompt events is used to evaluate the β-n rate. The correlation between the reconstructed prompt event and closest approach of the reconstructed muon track to it d can be used to increase the signal to BG ratio and as a result reduce the uncertainty. If a cut on d were to be used, the efficiency of such a cut would need to be well known and corrected for. This can be done using the Lateral Distance Profile LDP, which is the d distribution of β-n events including reconstruction and detector geometry effects. It is relatively easy to obtain the LDP for a subset of β-n events such that there is a large signal to BG ratio. This is done by separating the muons according their visible energy, and choosing the sub-sample with $E^{\mu}_{\text{vis}} > 600\,\text{MeV}$ gives the cleanest LDP. It is expected that the LDPs will differ between muons with different values of E^{μ}_{vis} as they have different geometrical effects. To create the LDPs for different sub-samples of muons, the LDP created

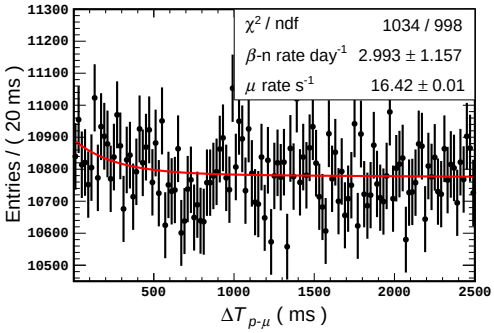

(a) The $\Delta T_{p\text{-}\mu}$ distribution for ID muons. The best fit gives $\mathscr{R}_{\beta\mathrm{n}}^{\mathrm{tot,ID}} = 2.99 \pm 1.16\,\mathrm{day}^{-1}$ and has a large error due to the small amount of β-n emitters compared to the muon rate.

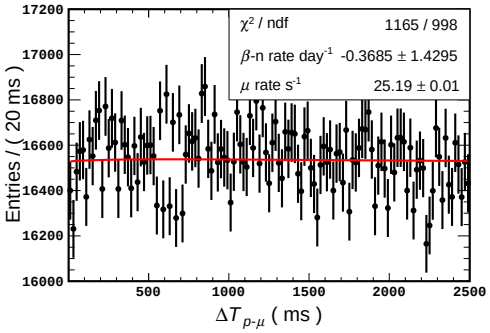

(b) The $\Delta T_{p\text{-}\mu}$ distribution for IV muons. The best fit gives $\mathscr{R}_{\beta\mathrm{n}}^{\mathrm{tot,IV}} = -0.37 \pm 1.43\,\mathrm{day}^{-1}$ which is compatible with zero. The error is larger than for ID muons shown opposite as the muon rate is higher.

Figure 4.2 The β-n rate from all muons estimated using the $\Delta T_{p\text{-}\mu}$ distribution to all IBD candidates, where the $\mathscr{L}_{\mathrm{Li}}$ veto is not applied. The plot on the left shows muons which deposit energy in the ID with $E_{\mathrm{vis}}^{\mu} > 20\,\mathrm{MeV}$. The plot on the right shows all remaining muons which only deposit energy in the IV, satisfying $E_{\mathrm{vis}}^{\mu} < 20\,\mathrm{MeV}$ and $E_{\mathrm{IV}}^{\mu} > 16\,\mathrm{MeV}$. The function described by Equation 4.1 is fitted to the distributions going back 20 s, although only the first 2.5 s are shown.

with $E_{\mathrm{vis}}^{\mu} > 600\,\mathrm{MeV}$ must be understood using a model, which once known can be applied to the other sub-samples to allow d cut efficiency estimation.

4.5.1 Lateral Distance Profile

To obtain the LDP, only muons with $E_{\mathrm{vis}}^{\mu} > 600\,\mathrm{MeV}$ are considered. To separate the β-n events from BG events, composed predominantly of IBDs, two time windows are considered. The first labelled the on-time window is closest to the prompt candidates in time and is filled with d information for $\Delta T_{p\text{-}\mu}$ between 1.25 ms and 500 ms. The on-time window contains a mixture of β-n and BG events and is represented in Figure 4.3a by the black points. A second window, labelled the off-time window contains the d distribution of BG events and as such only uses muons which are more than 2 s away from a prompt event. The IBD candidates from data may contain BG events which might not have the same distribution within the detector as the IBD candidates themselves, for example accidentals are likely to be uniformly distributed over the fiducial volume but IBD candidates, whose neutron capture is on H occur predominantly in the GC. To circumvent the possibility of obtaining a false BG distribution, d was calculating using muons from data and pure IBD candidates from MC. The resulting off-time or BG LDP (BLDP) is shown as a red line in Figure 4.3a and is

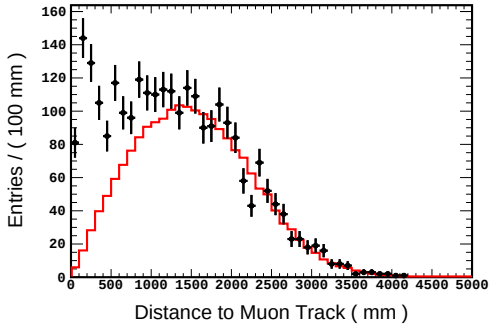

(a) Distance between muons and prompt MC IBD events from an on-time window (black) and off-time window (red). The off-time window was scaled to the number of BG events in the on-time window using a fit to the $\Delta T_{p\text{-}\mu}$ distribution.

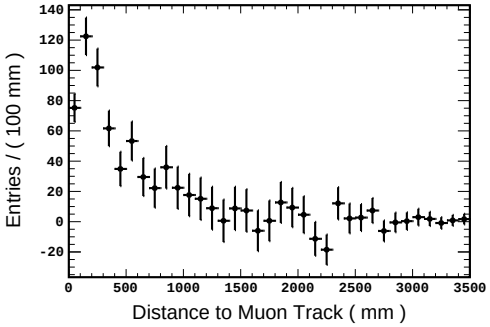

(b) The LDP of β-n events for muons with visible energy > 600 MeV, calculated by taking the difference of the on-time with the off-time windows shown in Figure 4.3a.

Figure 4.3 The Lateral Distance Profile (LDP) for muon and β-n events created using the difference of the on and off-time windows. To increase the signal to BG ratio muons with visible energy > 600 MeV were used. Muons from data but IBD prompt candidates generated by MC were used in the off-time window.

normalised to the estimated number of BG events in the on-time window. The number of BG events is calculated by fitting the $\Delta T_{p\text{-}\mu}$ distribution with Equation 4.1 where the start time and end time are set to 1.25 ms and 500 ms respectively in CF_c. The total number of events in the on-time window is given by $N^{\text{on}} = N^{\text{Li}} + N^{BG}$, from which the BG N^{BG} in the on-time window can be calculated. The off-time window is then normalised to N^{BG}. The difference between the on-time and off-time windows shown in Figure 4.3b is the LDP of β-n emitters for the muon sub-sample with visible energy greater than 600 MeV.

4.5.2 Toy MC Model

The LDP obtained in Section 4.5.1 is a mixture of the true distance distribution from the parent muon, detector geometry effects and reconstruction resolution which need to be disentangled and included in the model. The model described in this section contains two free parameters, λ the characteristic production length and σ_μ the muon reconstruction resolution. A large number of events were generated with different values of these parameters, which after correcting for detector geometry effects are compared to the LDP extracted from data in Section 4.5.1. Once these two parameters are known, the LDPs can be calculated for other muon visible energies which represent muons passing through different

parts of the detector and can be used to estimate the efficiency of a distance cut. This will improve the signal to BG ratio and as a result decrease the uncertainty on $\mathscr{R}_{\beta n}^{tot}$.

4.5.2.1 Real Radial Distribution

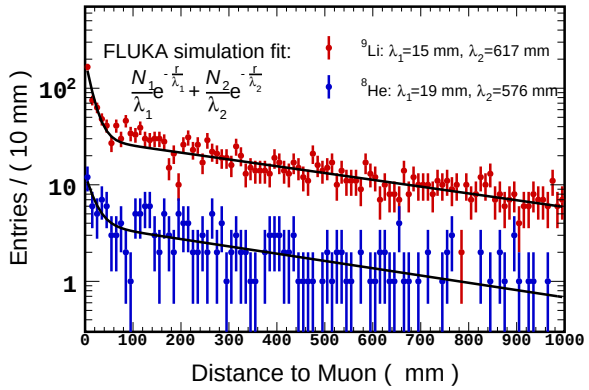

Figure 4.4 FLUKA simulations for the production of ^{9}Li and ^{8}He as a function of the distance from the parent muon. A fit of the function shown in the plot gives $\lambda_{1,\mathrm{Li}} = 15 \pm 3$ mm, $\lambda_{2,\mathrm{Li}} = 617 \pm 24$ mm, $\lambda_{1,\mathrm{He}} = 19 \pm 14$ mm and $\lambda_{2,\mathrm{He}} = 576 \pm 42$ mm. Data from [74]

The real distance r of ^{9}Li and ^{8}He production perpendicular to the parent muon track can be obtained from a FLUKA simulation [75, 76]. Figure 4.4 depicts such a simulation in the Double Chooz far detector where the ^{9}Li distribution is shown in red and ^{8}He in blue. The distributions can be fitted as the sum of two exponentials:

$$\phi(r) = \frac{N_1}{\lambda_1} e^{-\frac{r}{\lambda_1}} + \frac{N_2}{\lambda_2} e^{-\frac{r}{\lambda_2}} \tag{4.5}$$

where N is the umber of events and λ is the production length. Figure 4.4 shows a similar distribution for both isotopes and each has been fitted with Equation 4.5 giving the production lengths $\lambda_1^{\mathrm{Li}} = 15 \pm 3$ mm, $\lambda_{2,\mathrm{Li}} = 617 \pm 24$ mm, $\lambda_{1,\mathrm{He}} = 19 \pm 14$ mm and $\lambda_{2,\mathrm{He}} = 576 \pm 42$ mm. The parameters corresponding to the number of events return $N_{1,\mathrm{Li}} = 256 \pm 24$ events, $N_{2,\mathrm{Li}} = 1836 \pm 135$ events, $N_{1,\mathrm{He}} = 17 \pm 8$ events and $N_{2,\mathrm{He}} = 232 \pm 16$ events. The shorter production length λ_1 is most likely due to photo-nuclear interactions with ^{12}C nuclei, causing them to break apart into neutrons, protons and other daughter nuclei such as ^{9}Li and ^{8}He. The longer production length λ_2 is due to the primary production process through π^- interactions with ^{12}C. The results show that both ^{9}Li and ^{8}He have similar radial distribution profiles and that the longer component dominates in terms of the number of events.. As a result, the model used to recreate the

LDPs will use a single exponential decaying radially from the parent muon where the free parameter will be the characteristic production length λ.

4.5.2.2 Reconstruction Resolution

The muon path and the position of an event are both reconstructed as described in Sections 3.2.3 and 3.2.2 respectively. The reconstruction of these events brings about resolution effects following a Gaussian with the true position located at the mean. For the position reconstruction the width of the Gaussian is fixed to $\sigma_{\mathbf{X}} = 100\,\text{mm}$ from [14] whilst for the muons σ_μ is assumed to be unknown and left as a free parameter in the model. In the toy MC the frame of the parent muon is taken as the origin, such that it is travelling along the z-axis (through the page) and the x and y-axes are parallel to the page. A β-n event is randomly generated at a distance r from the muon, following a characteristic production length λ, in a random direction in the x-y plane. At random, the muon is reconstructed somewhere else in the x-y plane following a Gaussian with width σ_μ in a random direction. The same is done for the β-n event, but from a Gaussian distribution with width $\sigma_{\mathbf{X}}$. The distance between the reconstructed events d is used when comparing to the LDP from data.

4.5.2.3 Detector Geometry Effects

The LDP was created using a sub-sample of muons with $E^{\mu}_{\text{vis}} > 600\,\text{MeV}$ which asks the question whether the LDPs are the same for other muon energies or if there are geometric effects caused by the shape of the detector. The Impact Parameter (IP) is the shortest distance between the reconstructed muon track and the detector center explained schematically in Figure 4.5a where the IP is represented by the red arrow. The muons are separated into seven different sub-samples according to their visible energies and their IP distributions are shown in Figure 4.5b. It is clear that there is an anti-correlation between the visible energy of the muon and IP. Muons with $E^{\mu}_{\text{vis}} > 400\,\text{MeV}$ tend to pass through the target, $300-400\,\text{MeV}$ mainly in the GC and $20-300\,\text{MeV}$ pass through the buffer clipping the GC. β-n emitters are expected to be produced at all locations where ^{12}C is present, which in addition to the NT, includes the GC and buffer. Although the true production of the cosmogenic isotopes is expected to follow the same radial distribution shown in Figure 4.4, in the buffer the β-decays won't be observed as there is no liquid scintillator present. There may be some slight disparities between the volumes due to a difference in ^{12}C density, but the difference is small and will be ignored for now. This means that muons with low visible energy passing through the buffer, are expected to produce the cosmogenic isotopes with the

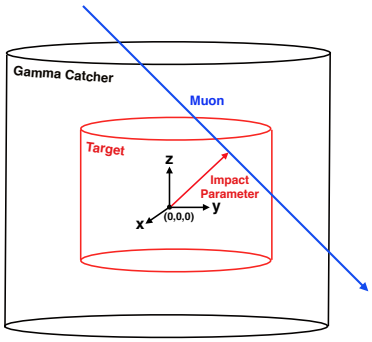

(a) A schematic diagram of the NT, GC, axis coordinates with the detector center as (0,0,0) and the impact parameter which is a muon's closest reconstructed distance to the detector center.

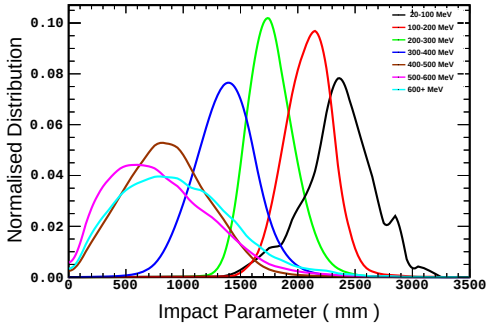

(b) The impact parameter is shown for muons separated into seven samples according to their visible energy. There is a clear anti-correlation between visible energy and impact parameter.

Figure 4.5 Impact parameter

same radial distribution, but the LDP should reflect the fact that few events will be observed close to the muon due to the non-scintillating buffer.

The Background Lateral Distance Profiles (BLDPs) of the muon sub-samples can be used to cross check whether there is any position dependence. They are created by selecting muon and prompt IBD pairs which are separated by more than 2 s to avoid correlated events. Then, instead of using the distributions from IBD data which may be contaminated by BGs whose spatial distribution in the detector could be different, MC generated IBD candidates subject to the same selection criteria as the data are used. In an infinite detector, one would expect the BLDPs to be the same for all the muon sub-samples. Their normalised distributions can be seen in Figure 4.6a, demonstrating that they are all different. Muons with a larger visible energy pass mainly through the center of the detector, which means the radial distribution is narrower. Those with a smaller visible energy have a broader distribution as they pass through the buffer, and as such have a wider fiducial volume where events can be located.

The true radial distribution described by Equation 4.5 is the expectation in an infinite detector with no reconstruction resolution effects. This is the same for all muons, however, due to the detector geometry, the corresponding LDPs will be different for each muon sub-sample. To calculate the modifying function called the envelope function, we can use the BLDPs and start by creating the distribution expected in an infinite detector. In an infinite detector, once again taking the muon as the reference frame, one would expect the number of BG events to be distributed evenly in the x-y plane. The number of events within each consecutive band of thickness dr is then $2\pi r\mathrm{d}r$, so a linear distribution in r is expected.

If one creates an LDP of this distribution including the reconstruction resolution described in Section 4.5.2.2, then this would be the expected distribution for an infinite detector. Instead, the distributions observed are the BLDPs given in Figure 4.6a. Dividing the BLDP with the LDP for an infinite detector, gives the envelope function for each muon sub-sample. This is multiplied with the β-n distribution to give the expected LDP. Figure 4.6b shows the envelope function for each muon sub-sample. To create LDPs representative of data, the envelope functions are multiplied by the β-n radial distribution.

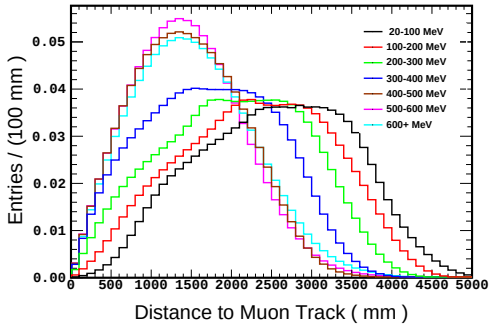

(a) BLDP for separate muon visible energy sub-ranges (muon-prompt). Taken by comparing BG muons to MC IBD candidates.

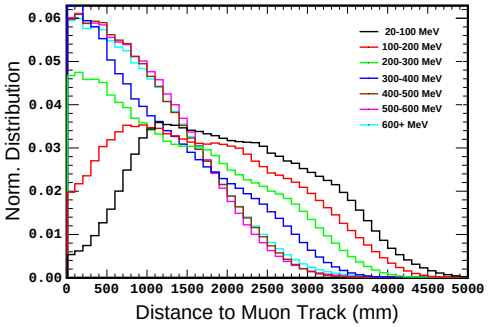

(b) Detector "envelope" functions given by dividing the BG LDP with the expected distribution from an infinite detector.

Figure 4.6 Distance to muon track for sub-samples of muons separated according to their visible energy

4.5.2.4 Toy MC and Best Fit

A toy MC is used to generate muon and β-n emitters from systematically varied values of the two parameters λ and σ_μ. The detector geometry effects are included using the detector envelope function for $E^{\mu}_{\text{vis}} > 600\,\text{MeV}$. The χ^2 is then calculated by comparing the toy MC data set to the LDP extracted from data in Section 4.5.1.
Figure 4.7 shows a plot of the reduced χ^2 on the vertical axis against the λ and σ_μ values used to create the toy MC. The function was fitted with a 2D polynomial to find the minimum at $\lambda = 491\,\text{mm}$ and $\sigma_\mu = 110\,\text{mm}$ with $\chi^2_{\text{min}}/d.o.f = 17.6/27$. To find the uncertainty on the parameters, the χ^2 was calculated from the minimum along the λ and σ_μ directions and fitted with a quadratic equation. For two free parameters, the point at which $\chi^2 = \chi^2_{\text{min}} + 2.3$ [22] is the 1σ error on each parameter giving $\lambda = 491 \pm 105\,\text{mm}$ and $\sigma_\mu = 110 \pm 33\,\text{mm}$.
Figure 4.8a shows the LDP from data along with a toy MC data set generated using the best fit parameters of λ and σ_μ. Figure 4.8b shows the normalised LDPs for all other sub-samples of E^{μ}_{vis} created using the best fit values of λ and σ_μ. Their differences arise

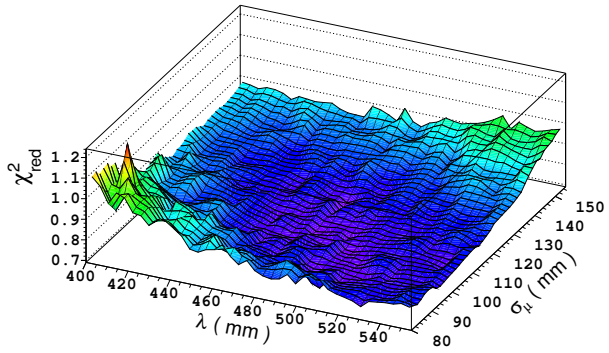

Figure 4.7 Reduced χ^2 for different values of λ and σ_μ

from the detector geometry and because muons with a smaller visible energy are further away from the fiducial volume. This is apparent for the lowest muon visible energy range 20 to 100 MeV where the probability of finding a β-n emitter is much smaller close to the muon track as they are in the non-scintillating buffer. We are now able to calculate the efficiency of any cut on the distance between a muon and prompt event in the data. This allows an increase in the signal to BG ratio and as a result the uncertainty on $\mathscr{R}_{\beta n}$ can be reduced.

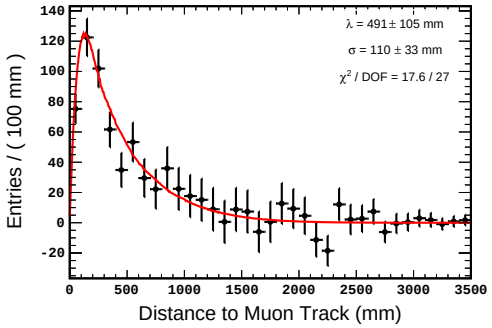

(a) The toy MC LDP created with the best fit parameters for λ and σ_μ shown in red along with the LDP from data represented by black points. Both are from muons $E^{\mu}_{\text{vis}} > 600\,\text{MeV}$

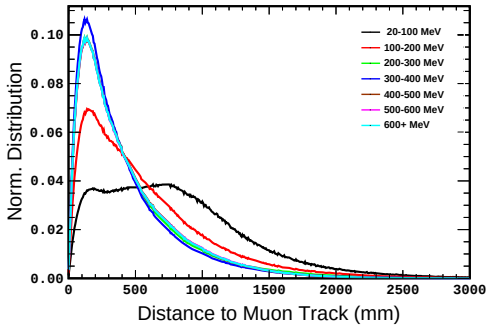

(b) The LDPs for separate muon visible energies created using the best fit parameters $\lambda = 491\,\text{mm}$ and $\sigma_\mu = 110\,\text{mm}$ including detector geometry effects.

Figure 4.8 The LDPs shown as solid lines are created using a toy MC with $\lambda = 491\,\text{mm}$ and $\sigma_\mu = 110\,\text{mm}$ from the best fit results. The plot on the left represents the LDP for $E^{\mu}_{\text{vis}} > 600\,\text{MeV}$ where the black points are extracted from data.

4.5.3 Efficiency Correction

The normalised distributions shown in Figure 4.8b represent the expected LDPs for different sub-samples of muons separated according to E^{μ}_{vis}. They can be used to estimate the efficiency of a distance cut ε_d which corresponds to the area of the normalised LDP between zero and d. The corrected β-n rate for each range of E^{μ}_{vis} is calculated by dividing the rate using the distance cut with the efficiency $\mathscr{R}^{d}_{\beta\text{n}}/\varepsilon_d$. The range of d from which the average of the corrected rates is taken, is chosen such that there are still enough events at minimum d for a fit to be meaningful, and maximum d because the LDPs show that between 69-91 % of all β-n events occur within 1000 mm of the muon track, depending on E^{μ}_{vis}. This corresponds to d between 400 mm and 1000 mm, where the β-n rate is evaluated in increments of 100 mm. The average corrected uncertainty was taken as the statistical error and the RMS of the values around the average was taken as the systematic uncertainty. The average β-n rates along with the statistical and systematic uncertainty for each muon sub-sample are shown in Table 4.1. The sum of the muon sub-samples gives $\mathscr{R}^{\text{tot}}_{\beta\text{n}} = 2.76^{+0.43}_{-0.39}(\text{stat})\pm 0.23(\text{syst})\ \text{day}^{-1}$. This value can be cross checked against the $\Delta T_{p\text{-}\mu}$ distribution for all muons shown in Figure 4.2a where the rate was found to be $2.99 \pm 1.16\,\text{day}^{-1}$. The two values are found to be fully consistent with one another and the upper uncertainty on the rate measurement has been reduced from 39 % in Section 4.4 to 18 % here.

Table 4.1 Average β-n rates corrected using the LDPs for each muon visible energy sub-sample.

E^{μ}_{vis} (MeV)	$\mathscr{R}^{\text{fit}}_{\beta\text{n}} \pm (\text{stat}) \pm (\text{syst})\ (\text{day}^{-1})$
$20-100$	$0.07 \pm 0.19 \pm 0.13$
$100-200$	$0^{+0.11}_{-0.00} \pm 0.03$
$200-300$	$0^{+0.14}_{-0.00} \pm 0.08$
$300-400$	$0.09 \pm 0.20 \pm 0.07$
$400-500$	$0.54 \pm 0.24 \pm 0.15$
$500-600$	$0.49 \pm 0.10 \pm 0.05$
>600	$1.58 \pm 0.12 \pm 0$
Total	$2.76^{+0.43}_{-0.39} \pm 0.23$

4.5.4 Additional Systematic Errors and Corrections to the β-n Rate

All sources of systematic uncertainties and their measurements are discussed in this section. They include the uncertainty on how well the two parameters λ and σ_{μ} are known in the toy

MC, the effect of the bin width, the fraction of ^{8}He in the total rate and the run length parameter R_L from Equation 4.1.

4.5.4.1 Toy MC Parameters

The uncertainties from the toy MC parameters estimated in Section 4.5.2.4 are $\lambda = 491 \pm 105$ mm and $\sigma_\mu = 110 \pm 33$ mm. To evaluate the effect of these uncertainties on $\mathscr{R}^{\text{tot}}_{\beta\text{n}}$, it is re-evaluated using LDPs created with values of λ and σ_μ shifted by the $\pm 1\sigma$ uncertainties and observing the change in $\mathscr{R}^{\text{tot}}_{\beta\text{n}}$. The resulting uncertainties were found to be $\mathscr{R}^{\text{tot}+3.3}_{\beta\text{n}-3.1}$ % for λ and $\mathscr{R}^{\text{tot}+0.3}_{\beta\text{n}-0.2}$ % for σ_μ.

4.5.4.2 Bin Width

The effect of the bin width used in the $\Delta T_{p\text{-}\mu}$ histograms on $\mathscr{R}^{\text{tot}}_{\beta\text{n}}$ was estimated by systematically varying the bin size and observing the ratio $\mathscr{R}^{\text{mod}}_{\beta\text{n}}/\mathscr{R}^{\text{tot}}_{\beta\text{n}}$, where $\mathscr{R}^{\text{mod}}_{\beta\text{n}}$ is the modified rate calculated using a different binning and $\mathscr{R}^{\text{tot}}_{\beta\text{n}}$ is the current rate from Section 4.5.3, using the standard bin width of 20 ms. Figure 4.9a shows the ratio where the bin width of the $\Delta T_{p\text{-}\mu}$ histograms is varied systematically between 10 and 200 ms. The histogram is fitted with a Gaussian whose mean value is taken as the correction factor and the sigma of the Gaussian is added as a systematic uncertainty.
The correction factor is 1.004±0.008 and shows that the bin width used of 20 ms slightly underestimates the mean rate.

4.5.4.3 ^{8}He Fraction

Throughout the analysis so far, the fraction of ^{8}He in $\mathscr{R}^{\text{tot}}_{\beta\text{n}}$ was assumed to be zero although a measurement of the ^{8}He fraction performed in Section 6.3 shows that this isn't the case. It was decided not to use the measurement from Section 6.3 here as this analysis will be published before the ^{8}He fraction results. Instead the published results from KamLAND are used [72] where the yields of each isotope are quoted taking into account inefficiencies such as neutron detection, energy, time and non β-n branching ratios. The yields are proportional to the average muon energy, i.e $Y(E_\mu) \propto E_\mu^\alpha$ where $Y(E_\mu)$ is the yield of each isotope, α is a scaling factor which is also isotope dependent and E_μ is the average muon energy. We can introduce a factor b to extrapolate to the DC far detector depth, giving $Y(E_\mu) = bE_\mu^\alpha$. The average muon energy and yields are known from [72] and allow the calculation of b for each isotope. The yields at the DC far detector depth can be calculated using the average muon energy from the off-off BG paper [77] and the previously calculated b factors. The yields are the total yields, so to be useful to us, a correction factor (from MC) is applied to correct for

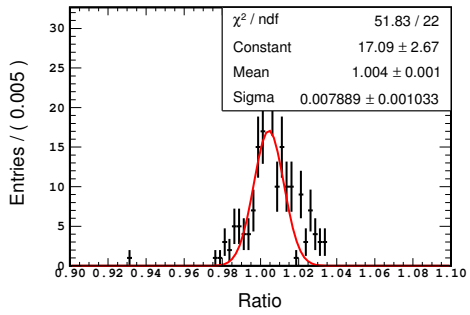

(a) The bin width is systematically varied between 10 and 200 ms and the ratio the corresponding rate $\mathscr{R}_{\beta n}^{\text{mod}}$ to the standard rate $\mathscr{R}_{\beta n}$ using a bin width of 20 ms is shown. A Gaussian fit to plot gives a correction factor of 1.004 ± 0.008.

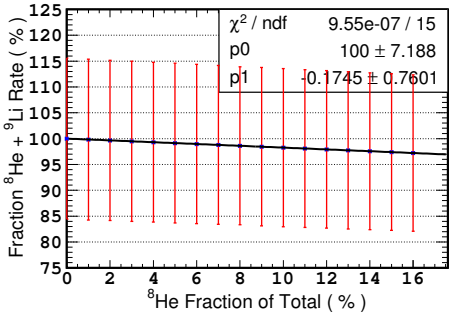

(b) The ^{8}He fraction was systematically varied between 0 and 20 % and the percentage change compared to $\mathscr{R}_{\beta n}$ is shown. The best fit line was used to evaluated the correction factor and associated uncertainty from the KamLAND measurement scaled to the DC far detector depth.

Figure 4.9 Evaluation of the systematic uncertainties from the bin width and ^{8}He fraction on the $\mathscr{R}_{\beta n}$

DC energy cuts, muon dead time and branching ratios (not all branches decay via the β-n route) as shown in Figure 6.1. This gives a ^{8}He fraction of $F_{He}^{DCfar} = \frac{Y_{He}}{Y_{He}+Y_{Li}} = 7.9 \pm 6.5\%$. The fraction of ^{8}He in Equation 4.1 is then systematically varied between 0 and 20 % giving the modified rate $\mathscr{R}_{\beta n}^{\text{mod}}$, whose percentage of $\mathscr{R}_{\beta n}^{\text{tot}}$ is shown in Figure 4.9b. There is a clear anti-correlation between the ^{8}He fraction and the total β-n rate. The results are fitted with a straight line and used to estimate the correction factor evaluated at the calculated KamLAND fraction of 7.9 %. The uncertainty due to the KamLAND measurement on $\mathscr{R}_{\beta n}^{\text{tot}}$ is evaluated by calculating its fractional change when the ^{8}He fraction is changed by ± 6.5 %.

The correction to $\mathscr{R}_{\beta n}^{\text{tot}}$ and its corresponding uncertainty was measured to be $-1.4 \pm 1.1\%$.

4.5.4.4 Run Length Parameter

The $\Delta T_{p\text{-}\mu}$ histograms have a slope at large $\Delta T_{p\text{-}\mu}$ which is assumed to arise from the finite run length, prompting the introduction of the run length parameter in Equation 4.1. To estimate the systematic uncertainty from this parameter, it was left free in the fit and its effect on $\mathscr{R}_{\beta n}^{\text{tot}}$ was evaluated.

The associated uncertainty was estimated to be ± 3.3 %.

4.5.5 Combination LDP and MIN rates

The uncertainty on $\mathscr{R}^{\text{tot}}_{\beta\text{n}}$ can be further reduced by combining it with a β-n enriched sample. The enriched sample is chosen so that its β-n rate is as close to $\mathscr{R}^{\text{tot}}_{\beta\text{n}}$ as possible whilst minimising the uncertainty on its measurement. This allows it to be combined with the β-n rate evaluated in Section 4.5 to reduce the overall uncertainty. Since the Double Chooz publication [14], an asymmetric error has been used on $\mathscr{R}^{\text{tot}}_{\beta\text{n}}$ in the $\sin^2(2\theta_{13})$ fit which has allowed this approach to be used.

The β-n enriched sample was selected using the following criteria:

1. $E^{\mu}_{\text{vis}} > 400\,\text{MeV}$ and number neutrons > 0

2. $E^{\mu}_{\text{vis}} > 500\,\text{MeV}$, number neutrons = 0 and $d < 1\,\text{m}$

where the definition of a neutron is that its time to the latest muon $< 1\,\text{ms}$ and $1.8 < E_{\text{vis}} < 2.6\,\text{MeV}$ or $4 < E_{\text{vis}} < 10\,\text{MeV}$ corresponding to its capture on H and Gd respectively. The $\Delta T_{p\text{-}\mu}$ histogram corresponding to the enriched sample is shown in Figure 4.10a where a fit with Equation 4.1 gives a rate of $2.26 \pm 0.15\,\text{day}^{-1}$. This rate and uncertainty can be shown in $\Delta\chi^2$ space in Figure 4.10b as a black line to the left of the kink. To the right of the kink, the rate from Section 4.5.3 corresponding to $2.76^{+0.49}_{-0.45}$ is shown. In both cases $\Delta\chi^2 = 0$ is taken as the rate and $\Delta\chi^2 = 1$ is taken as the 1σ uncertainty, which is why the enriched rate curve is much narrower as it has a smaller uncertainty. The black curve is then fitted with a two sided quadratic function $\Delta\chi^2 = \frac{x-\mu}{\sigma_{l,r}}$ where μ is the new rate which joins each side of the quadratic function and $\sigma_{l,r}$ are the two different sigmas on each side of the rate, μ.

The red curve gives a new rate of $2.61^{+0.55}_{-0.30}\,\text{day}^{-1}$. Although the new rate has moved to a lower value and the discrepancy between the upper and lower sigma has increased, the overall uncertainty has been reduced. The $\sin^2(2\theta_{13})$ fit explained in Section 3.11 with more detail in Section 3.7 explains the use of nuisance or pull parameters in the χ^2 fit function. The pull parameters act such that the value of $\mathscr{R}^{\text{tot}}_{\beta\text{n}}$ is allowed to move according to its measured uncertainty. This means that a change in $\mathscr{R}^{\text{tot}}_{\beta\text{n}}$, as long as the uncertainty is estimated correctly will give enough freedom to the fit for the output parameter of $\mathscr{R}^{\text{tot}}_{\beta\text{n}}$ to move to the correct value and explains why combining the two rates in this manner is possible.

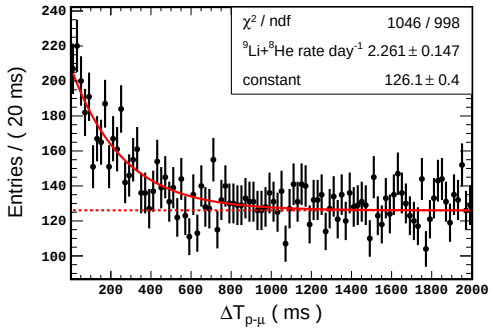

(a) The β-n enriched sample obtained by selecting muons with $E^{\mu}_{\text{vis}} > 400\,\text{MeV}$ and number neutrons > 0 or $E^{\mu}_{\text{vis}} > 500\,\text{MeV}$, number neutrons = 0 and $d < 1\,\text{m}$.

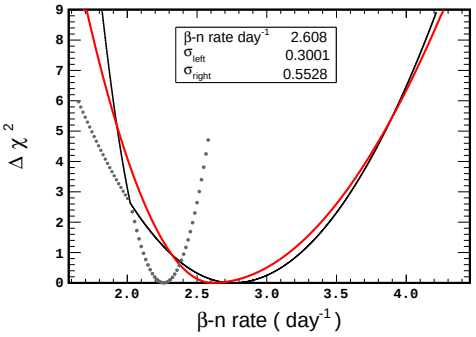

(b) The enriched rate is shown as the black line to the left of the kink and the LDP method rate from Section 4.5 is the black line to the right of the kink. The red line is a double sided quadratic fitted to the black curve giving a new rate of $2.61^{+0.55}_{-0.30}\,\text{day}^{-1}$

Figure 4.10 The figure on the left shows the $\Delta T_{p\text{-}\mu}$ distribution from the β-n enriched sample. The figure on the right shows the combination of the β-n enriched sample rate with $\mathscr{R}^{\text{tot}}_{\beta\text{n}}$.

4.6 $\mathscr{L}_{Li}$ Veto

4.6.1 $\mathscr{L}_{Li}$ Rate Estimate

Finally, the number of events removed by the $\mathscr{L}_{Li}$ veto needs to be estimated so that it can be subtracted from $\mathscr{R}^{\text{tot}}_{\beta\text{n}}$.

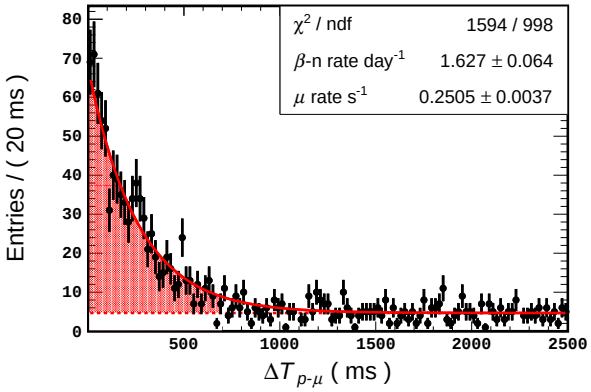

Figure 4.11 Muons with $\mathscr{L}_{Li} > 0.4$

In the first method the $\Delta T_{p\text{-}\mu}$ distribution of all muons which fulfill the veto criteria of $\mathscr{L}_{Li} > 0.4$ are fitted with 4.1. The $\Delta T_{p\text{-}\mu}$ distribution can be observed in Figure 4.11 and the

fit returns a β-n rate of $1.63 \pm 0.06\,\mathrm{day}^{-1}$. In this fit CF_c is set to a window time of 1.25 to 700 ms as $\mathscr{L}_{Li}$ is only calculated over this time period. It should be noted that this method only works because the average time between muons that fulfill this criteria are on the order of 10 s. Otherwise the method of only choosing the muon with the highest $\mathscr{L}_{Li}$ in the veto would make this approach unfeasible.

As a cross check, if the number of events removed by the $\mathscr{L}_{Li}$ veto are known, then a simple subtraction of the estimated number of BG events or non β-n will give the $\mathscr{L}_{Li}$ veto rate. The total number of events rejected by the $\mathscr{L}_{Li}$ vetoes is 932. To estimate the number of non β-n emitters in this number, 10 consecutive time windows of length 700 ms were created starting from $\Delta T_{p\text{-}\mu}$ = 2000 to 2700 ms. For each time window, the same procedure used to calculate $\mathscr{L}_{Li}$ was applied to all muons and the highest value noted for each window, excluding any that occur within the first 1.25 ms of each. If the value is greater than 0.4 for each window (where the procedure is applied to each neutrino candidate separately) the window is incremented by one. The average value was taken and found to be 167.7±4.2 events. This number is subtracted from 932 and divided by the live time to give a rate of $1.65 \pm 0.07\,\mathrm{day}^{-1}$, which is in agreement with the the value from the $\Delta T_{p\text{-}\mu}$ fit.

4.6.2 IBD Inefficiency from $\mathscr{L}_{Li}$

Simulated IBD candidates, or MC are used in Section 3.11 to estimate $\sin^2(2\theta_{13})$. They are produced in accordance with the instantaneous thermal power at the two reactors. As a result, the inefficiency of any selection criteria that affects the number of detected IBD candidates, must be known so that a correction can be made to the number of IBD candidates from the MC. The $\mathscr{L}_{\mathrm{Li}}$ veto is one such device that induces IBD inefficiency.

To estimate the fraction of IBD candidates removed by the $\mathscr{L}_{\mathrm{Li}}$ veto, ten windows each of length 700 ms, corresponding to the time window used to calculate the $\mathscr{L}_{\mathrm{Li}}$ in $\Delta T_{p\text{-}\mu}$ were created. The first one starts 2 s prior to any prompt events to remove any correlated events such as β-n emitters because a pure sample of IBDs is required. The $\mathscr{L}_{\mathrm{Li}}$ is calculated for each window in exactly the same fashion as is normally done, except with the time offset of each window. The events within 1.25 ms of each window are ignored and the highest value $\mathscr{L}_{\mathrm{Li}}$ is noted. The IBD inefficiency is defined as:

$$\mathscr{L}_{\mathrm{Li}}^{\mathrm{ineff}} = \frac{\sum_{i=1}^{10} n_{\mathrm{veto}}}{\sum_{i=1}^{10} n_{\mathrm{tot}}} \tag{4.6}$$

where n_{veto} is the number of times where the $\mathscr{L}_{\mathrm{Li}} > 0.4$ and n_{tot} is the total number of events in that window. This gives an IBD inefficiency of $\mathscr{L}_{\mathrm{Li}}^{\mathrm{ineff}} = (0.508 \pm 0.012)\,\%$.

4.7 Final Rate

The rate after all corrections, inclusion of systematic uncertainties and subtraction of events removed by the $\mathscr{L}_{Li}$ veto gives:

$$\boxed{\mathscr{R}^{\text{fit}}_{\beta\text{n}} = 0.95^{+0.57}_{-0.33}}$$

This is the final number used as the estimate of the β-n background rate in the measurement of $\sin^2(2\theta_{13})$ described in Section 3.11.

4.8 Conclusion

This Chapter summarises the methods used to estimate the rate of β-n emitters contaminating the IBD sample selected through neutron capture on H. The preliminary analysis looking at all muons gave an uncertainty on $\mathscr{R}^{\text{tot}}_{\beta\text{n}}$ of 39 %. By evaluating the LDPs for different muon sub-samples selected according to their visible energy and applying an efficiency corrected distance cut has reduced this uncertainty to 18 %. The final rate $\mathscr{R}^{\text{fit}}_{\beta\text{n}}$ and its uncertainty is an important input to the $\sin^2(2\theta_{13})$ measurement described in Section 3.11. Although it still dominates the sum of uncertainties from all the BGs by over 50 %, it has improved significantly since the previous publication [45], where the estimate was $\mathscr{R}^{\text{fit,tot}}_{\beta\text{n}} = 2.8 \pm 1.2\,\text{day}^{-1}$.

Part III

Cosmogenic Radioisotopes

Chapter 5

Muons and Radioisotope Production

5.1 Introduction

A brief introduction into the muon differential energy spectrum and its evolution as a function of depth given radiative energy losses. A derivation of the yield and production rate definitions for cosmogenic isotope production is given from the cross section of the muon and target atom interaction. Finally, the relationship between the yield of a cosmogenic radioisotope and the mean muon energy, which is related to the depth is given

5.2 Muon Passage through Earth

As muons pass through the earth they lose energy due to ionisation and the radiative processes bremsstrahlung, pair production and photo-nuclear interactions. The energy loss due to these mechanisms can be described by:

$$-\frac{dE_\mu}{dX} = a + bE_\mu \tag{5.1}$$

where a is the loss due to ionisation and b is the energy loss due to radiative processes [22]. The energy loss due to the three radiative energy losses included in b are described as follows [78]:

$$b = b_{Brem} + b_{Pair} + b_{Hadronic} \tag{5.2}$$

Both a and b have a dependence on the muon energy E_μ. Equating the two terms due to energy loss gives a critical energy $\varepsilon \equiv a/b$ above which discrete, radiative processes become more important than continuous energy loss.

Integrating Equation 5.1 under the assumption that the energy dependence of a and b is small and can be neglected gives:

$$E_\mu = (E_{\mu,0} + \varepsilon)e^{-bX} - \varepsilon \tag{5.3}$$

where $\varepsilon = a/b$. This is the relation between the energy of a muon when it is produced in the atmosphere $E_{\mu,0}$ and its average energy after travelling a distance X through matter.

The differential muon energy spectrum on the Earth's surface is taken from Gaisser [78]:

$$\frac{\mathrm{d}N_\mu}{\mathrm{d}E_\mu} = 0.14E_\mu^{-2.7} \cdot \left(\frac{1}{1 + \frac{1.1E_\mu \cos\theta}{115\,\mathrm{GeV}}} + \frac{0.054}{1 + \frac{1.1E_\mu \cos\theta}{850\,\mathrm{GeV}}} \right) \mathrm{cm}^{-2}\,\mathrm{sr}^{-1}\,\mathrm{s}^{-1}\,\mathrm{GeV}^{-1} \tag{5.4}$$

However, this differential spectrum doesn't fit the data very well at low muon energies as it doesn't take into account muon decay and muon loss. Instead, a function taken from Heisinger [79] is used:

$$\frac{\mathrm{d}N_\mu}{\mathrm{d}E_\mu} = \frac{20.74}{E_\mu^{3.7} + 99.83E_\mu^{2.833} + 1424E_\mu^{1.731} + 6613} \mathrm{cm}^{-2}\,\mathrm{sr}^{-1}\,\mathrm{s}^{-1}\,\mathrm{GeV}^{-1} \tag{5.5}$$

This gives the differential muon spectrum on the Earth's surface. If the spectrum is to be calculated at a depth X, the muon energy as a function of depth described in Equation 5.3 can be substituted into the spectrum at the Earth's surface given by Equation 5.5. The muon energy dependence of the variables a and b was taken into account by applying a fit to four values given at various depths for each in [80] which is then used to estimate each of them for each muon energy. The differential muon spectrum can be calculated for different depths by estimating the muon energy loss as a function of distance travelled through the Earth and the calculated spectra can be observed in Figure 5.1.

5.3 Cross Section

The cross section for the production of muon induced radioactive isotopes has been measured using muon beams. One such experiment wished to evaluate the BG component in the GALLEX experiment from cosmogenic isotopes by irradiating a tank containing 851 of $GaCl_3 - HCl$ solution with a muon beam from CERN. In this particular case mono-energetic muon beams with energies 100 GeV, 200 GeV and 280 GeV were used. I have taken the

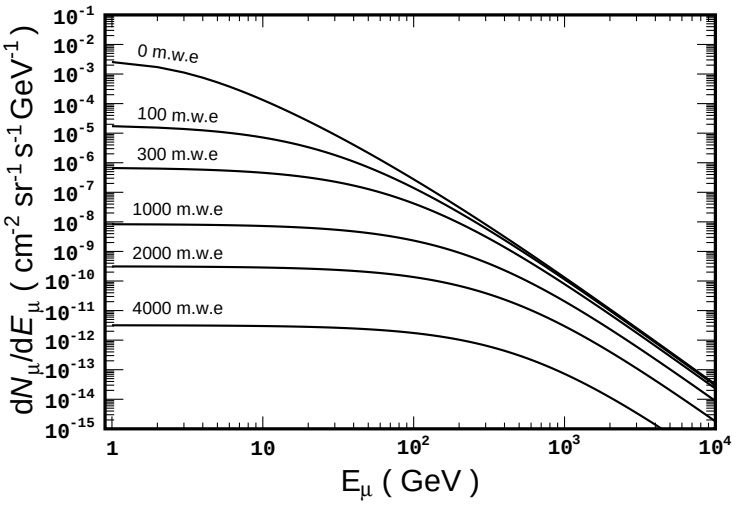

Figure 5.1 Differential muon rate spectrum as a function of muon energy. The surface spectrum was calculated using Equation 5.5 from [79]. The spectra underground were calculated by propagating the muon energy loss using Equation 5.3 from the surface spectrum. This includes the muon energy dependence of a and b, where a fit was applied to the four values given at various depths for each in [80] and then used to estimate them for each muon energy.

formula for the cross section of cosmogenic isotope production from Cribier [81] as:

$$\sigma_{\text{eff}} = \frac{\mathscr{N}_c}{N_\mu \cdot l \cdot n_T} \tag{5.6}$$

where σ_{eff} is the effective cross section not corrected for isotope production away from the muon track and therefore not observed in the detector, $\mathscr{N}_c$ is the efficiency corrected number of cosmogenic isotope c produced, l is the length of the target, n_T is the number density of target atoms and $\mathscr{N}_\mu$ is the number of muons that pass through the target. This experiment used a cylindrical tank of length l and this distance represents the distance travelled by the the muons through the target.

Nowadays it is more useful to use the average length a muon has travelled through the target denoted by $\langle l_\mu \rangle$ as we consider the cosmic muon flux rather then muon beams. The muon flux ϕ_μ is given by:

$$\phi_\mu = \frac{R_\mu \langle l_\mu \rangle}{V} = \frac{N_\mu}{T_L} \frac{\langle l_\mu \rangle}{V} \tag{5.7}$$

where T_L is the live time, R_μ is the muon rate, N_μ is the number of muons passing through the target with a volume V. Equation 5.6 can be re-arranged using the definition of ϕ_μ into a

format more useful today:

$$\sigma = \frac{\mathscr{N}_c}{\phi_\mu T_L N_T} \tag{5.8}$$

where N_T is the number of target atoms within the volume.

The dependence of the cross section for muon induced radioactive isotopes production is thought to follow a power law as follows [79]:

$$\sigma(E_\mu) = \sigma_0 \cdot E_\mu^\alpha \tag{5.9}$$

where the cross section σ is a function of the muon energy E_μ and α is the power law exponent.

5.4 Cosmogenic Production Rates and Yields

The production rate of muon-induced radioactive isotopes can be calculated using the cross section [82]:

$$R_c = N_T \int \frac{\mathrm{d}N_\mu}{\mathrm{d}E_\mu} \sigma(E_\mu) \mathrm{d}E_\mu \tag{5.10}$$

where $\mathrm{d}N_\mu/\mathrm{d}E_\mu$ is the differential muon rate energy spectrum at depth h.

A substitution of the muon energy dependence in Equation 5.9 allows the production rate to be written as:

$$R_c = N_T \sigma_0 \int E_\mu^\alpha \frac{\mathrm{d}N_\mu}{\mathrm{d}E_\mu} \mathrm{d}E_\mu \tag{5.11}$$

The production rate can also be defined in terms of the mean muon energy and muon flux as:

$$R_c = \beta_\alpha N_T \sigma \langle E_\mu \rangle^\alpha \phi_\mu \tag{5.12}$$

where ϕ_μ is the total muon flux and the correction factor β_α compensates for the averaging of E_μ:

$$\beta_\alpha(h) = \frac{\langle E_\mu^\alpha \rangle}{\langle E_\mu \rangle^\alpha} \tag{5.13}$$

where the mean muon energy is defined as:

$$\langle E_\mu \rangle = \frac{\int E_\mu \frac{\mathrm{d}N_\mu}{\mathrm{d}E_\mu} \mathrm{d}E_\mu}{\int \frac{\mathrm{d}N_\mu}{\mathrm{d}E_\mu}} \tag{5.14}$$

The yield and production rate is calculated by both KamLAND [72] and Borexino [83] using the following formula:

$$Y_c = \frac{\mathscr{N}_c}{R_\mu T_L \cdot \langle l_\mu \rangle \cdot \rho} \tag{5.15}$$

and the production rate as follows:

$$R_c = \frac{\mathscr{N}_c}{V \cdot \rho \cdot T_L} \tag{5.16}$$

where $\mathscr{N}_c$ denotes the total number of decays of the cosmogenic radioisotope c, R_μ is the muon rate in the volume, T_L is the live time, $\langle l_\mu \rangle$ is the average muon track length in the volume, ρ is the density of the volume liquid, ε_{det} is the detection efficiency and V is the volume. However, in the Double Chooz Collaboration a measurement of $\langle l_\mu \rangle$ through the detector and R_μ depend on the muon reconstruction algorithm, where any biases have not been fully investigated. Instead, a publication of the BGs measured during a period of time where both reactors were off and only a small number of anti-neutrinos were expected evaluated the muon flux at the far detector site $\phi_\mu^{\mathrm{DC}} = 0.72 \pm 0.04\,\mathrm{s}^{-1}\,\mathrm{m}^{-2}$ instead [77]. The yield given by Equation 5.15 can be re-arranged using the muon flux relation given by Equation 5.7 to:

$$Y_c = \frac{\mathscr{N}_c}{\phi_\mu V \cdot T_L \cdot \rho} \tag{5.17}$$

This equation will be used over the subsequent chapters to calculate the yield of a given cosmogenic radioisotope produced in the DC far detector. A substitution of the yield definition into the cross section Equation 5.8 gives:

$$Y = \frac{\sigma}{m_T} \tag{5.18}$$

where m_T is the mass of the target atom. The yield measurement can be thought of as the cross section per target mass. A substitution into Equation 5.9 can be made using the yield definition instead of the cross section and using the mean muon energy to give the relationship:

$$Y = Y_0 \langle E_\mu \rangle^\alpha \tag{5.19}$$

This equation gives a relationship for the yield of each cosmogenic radioisotope as a function of mean muon energy.

Chapter 6

^{9}Li and ^{8}He

The radioisotopes ^{9}Li and ^{8}He are produced in organic liquid scintillators by cosmic muon interactions with ^{12}C. They both undergo β-decay, where all decays except those which end up in the lowest energy state of the daughter nucleus subsequently emit a neutron[1], giving them their name β-n emitters. This is important for detectors observing anti-neutrinos through IBD as the two signals are almost completely indistinguishable. Measurements of the yields and production rates at the DC depth, which in this thesis only uses data from the far detector, can be compared to measurements at other depths such as KamLAND [72] and Borexino [83] to give an estimate of the power law exponent α as a function of the average muon energy $\langle E_\mu \rangle$. Knowledge of the power law exponent would allow future experiments to estimate the β-n background at their depth.

A measurement of the β-n emitters in DC is carried out to evaluate the background contamination in the IBD samples for both the Gd and H-channels as explained in Section 3.5.3 and Chapter 4 respectively. This measurement contains a mixture of both ^{8}He and ^{9}Li decay events, which for the calculation of the yields and production rates needs to be separated into the rate for each radioisotope. They can be separated if a measurement of the ^{8}He fraction f_{He} is made by fitting a relatively pure sample of β-n emitters to the individual predicted spectra produced by MC. As the visible energy and $\Delta T_{p\text{-}\mu}$ of each radioisotope has a characteristic distribution in accordance with the β[2] spectrum and exponential decay following each characteristic lifetime, the fit can take advantage of both.

An explanation of the event selection and corresponding $\Delta T_{p\text{-}\mu}$ and visible energy spectrum distribution is given in Section 6.2 and an explanation of the ^{8}He fraction fit is given in

[1] Please note that Figure 6.1a shows that the 7940 keV line doesn't decay with a neutron, but later in [84] this is contradicted and for this work it is assumed that it does.

[2] In the β-n emitter situation the energy spectrum isn't purely composed of β^- events, there are also contributions from the subsequent decays of the ^{9}Li and ^{8}He daughter nuclei.

Section 6.3. The β-n background rate estimate for the Gd-channel IBD sample from Section 3.5.3 is separated into the ^{8}He and ^{9}Li components using f_{He}. Efficiency corrections, for example non-neutron emitting branching ratios which are specific to each isotope are corrected for and the yields and production rates calculated. Section 6.4 compares the yield measurements at the DC far detector to those at KamLAND and Borexino together with the power law exponent measurement.
This section uses the full data set described in Chapter 3 corresponding to 467.9 and 462.72 days of live time for the Gd and H analyses respectively [14, 46].

6.1 Predicted Energy Spectrum

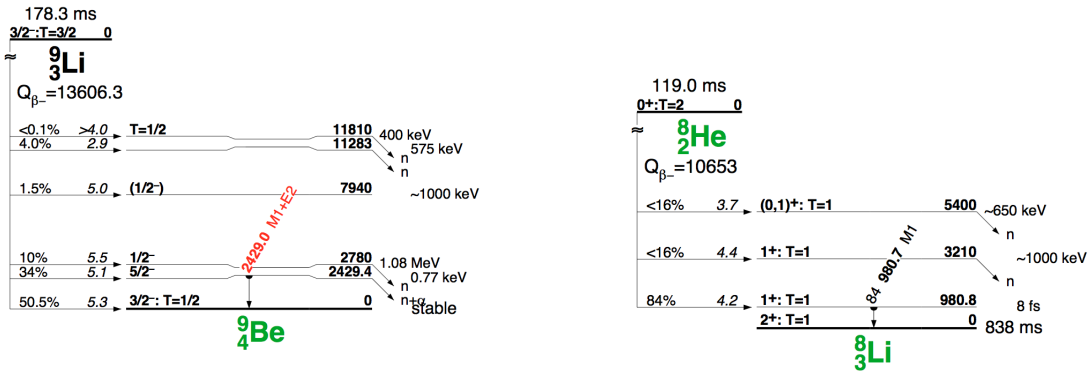

(a) ^{9}Li decay scheme. 49.5 % of the decays will subsequently emit a neutron.

(b) ^{8}He decay scheme. Less than 16 % of the decays will subsequently emit a neutron.

Figure 6.1 The decay schemes for ^{9}Li and ^{8}He where some branches subsequently emit a neutron. On these occasions they are collectively referred to as β-n emitters, whose double coincidence mimics the IBD signal. Source [84]

Generating predicted spectra for ^{9}Li and ^{8}He is complicated, as in addition to the β^{-} decay, the following decays result in the emissions of α's. In the case of the β-n chain for ^{9}Li, the subsequent decay will always be to $\alpha+\alpha+n$. Although the neutron is observed as a separate, delayed event, the DC detector cannot differentiate between the β^{-}'s and the $\alpha's$ due to the short decay times of the daughter ^{9}Be nucleus so the prompt visible energy spectrum will be a mixture of all energy depositions. Quenching, the reduced light yield of some ions, is approximately one tenth compared to an electron for α's and is taken into account in the simulation. Not all of the branching ratios are known for the subsequent decay, so each branch is simulated individually to create the raw spectra. The raw spectra

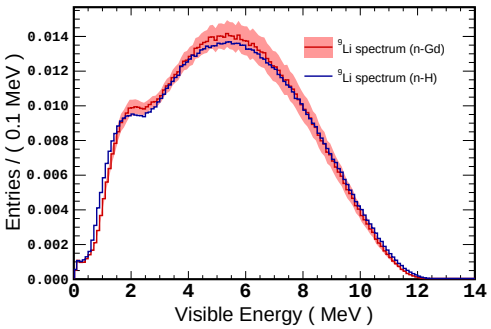

(a) The prediction of the prompt visible energy spectra for the ^{9}Li β-n emitter.

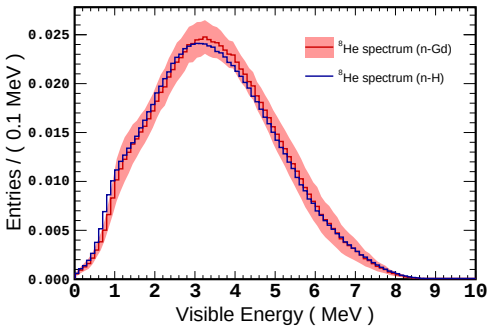

(b) The prediction of the prompt visible energy spectra for the ^{8}He β-n emitter.

Figure 6.2 The predicted visible energy spectra for the β-n emitters ^{9}Li and ^{8}He. For each there are two spectra created by applying the selection criteria for the Gd-channel shown in red and the H-channel in blue. The uncertainty, displayed using pink bands is only shown for the Gd-channel for the sake of clarity, it is similar for the H-channel. The error only represents the diagonal elements in the covariance matrix created for that spectrum. Source [85]

decay chains are then passed through software which simulates the effects of the detector response and electronics, called the detected spectra. The IBD analysis cuts described in Chapter 3 are applied to the detected spectra. There are two sets of selection cuts, one each for delayed neutron capture on H and Gd, so there are also two prompt visible spectra for ^{9}Li and ^{8}He each. The two spectra differ slightly due to the selection of the delayed neutron. In the H-channel the neutrons, especially those with higher energy are more likely to leave the FV[3] which means that the prompt events corresponding to that neutron and particular decay branch won't be observed. For each spectrum the decay chains are varied according to the uncertainties on their branching ratios to create covariance matrices. An additional uncertainty from the weak magnetism is included in the covariance matrices. These are then used in the ^{8}He fraction fit. Figure 6.2 shows all four prompt visible energy spectra, separated into two plots according to the cosmogenic β-n emitter being considered. In each plot the spectrum expected for the Gd-channel is shown in red and the H-channel is shown in blue. The uncertainty shown by the pink bands, is only displayed for the Gd-channel spectra although it is similar for the H-channel. More information can be found in [85].

[3] In the H-channel, the FV includes the GC.

6.2 Energy Spectrum and Time Distribution

The β-n emitters ^{9}Li and ^{8}He are indistinguishable from IBD events, so their preliminary selection is made using the criteria described in Chapter 3. This gives us two samples of IBD candidates which can be used in the f_{He} measurement, those from delayed neutron capture on H and on Gd. Normally, the $\mathscr{L}_{\mathrm{Li}}$ is used to remove or veto β-n emitters. In this case, we want to obtain a relatively pure sample of β-n candidates, so instead of removing these events from the IBD sample, we select them and reject the IBD candidates. An explanation of $\mathscr{L}_{\mathrm{Li}}$ is given in Section 3.4.4 and [68].

Normally, the $\mathscr{L}_{\mathrm{Li}}$ is calculated for $\Delta T_{p\text{-}\mu}$ up to 700 ms prior to the prompt. As we wish to evaluate the BG component within the β-n sample, the $\mathscr{L}_{\mathrm{Li}}$ is calculated for all muon prompt pairs with $\Delta T_{p\text{-}\mu} < 16.1$ s. If $\mathscr{L}_{\mathrm{Li}} > 0.4$, the $\Delta T_{p\text{-}\mu}$ and E_{vis} information is placed in a 2D histogram.

The Gd and H β-n samples are first treated separately to check the validity of the spectra in each. In the normal IBD selection, the prompt visible energy cuts and muon dead time differ between the Gd and H-channels. To avoid any normalisation issues further down the line, the same cuts are applied to both and only events which satisfy $E_{\mathrm{vis}} \in [0.7, 12]$ MeV and which aren't within 1.25 ms of a muon are selected. The β-n visible energy spectra are shown separately for the two channels in Figure 6.3. On-time windows which select events satisfying $\Delta T_{p\text{-}\mu} \in [1.25, 701.25]$ ms are shown as a black line. The average of twenty off-time windows between $\Delta T_{p\text{-}\mu} \in [2.1, 16.1]$ s, each of which has the same length as the on-time window gives the BG spectrum represented by blue points. The BG is composed mostly of IBD candidates although other BGs may be present. This is apparent in the H-channel where there are more events present at lower energies compared to the Gd-channel, which are compatible with accidentals. The difference between the on-time and BG spectra give the β-n spectra shown by the red points. The β-n spectra appear to be coherent between the two samples.

To increase the available statistics the β-n candidates from the H and Gd-channels are combined. The resulting $\Delta T_{p\text{-}\mu}$ and E_{vis} distributions are shown in Figure 6.4a. Although the distribution is known until $\Delta T_{p\text{-}\mu} = 16.1$ s, only the first 2.1 s are shown as a flat distribution is observed at at longer times. This flat distribution shows the BG component whilst the build-up of events at $\Delta T_{p\text{-}\mu} < 2$ s is due to an excess of β-n emitters correlated to the muons. To include all the uncertainties, a χ^2 fit is performed which requires there to be enough events in each bin for a Gaussian uncertainty to be valid. As a result the visible energy spectrum is split into bins with a width of 1 MeV except for the first and final bins which have a width of 0.8 MeV and 2.5 MeV respectively, bringing the total number of bins along the energy axis to $B_E = 10$. The $\Delta T_{p\text{-}\mu}$ axis has been split into bin widths of 175 ms, starting

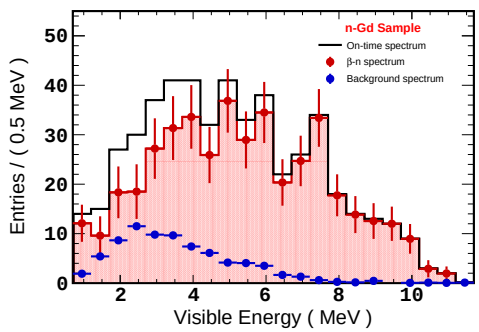

(a) β-n candidates from the Gd-channel.

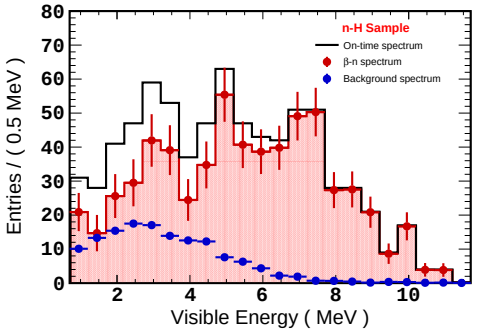

(b) β-n candidates from the H-channel.

Figure 6.3 The events shown satisfy $\mathscr{L}_{\mathrm{Li}} > 0.4$, where the on-time and BG spectra differ according to their $\Delta T_{p\text{-}\mu}$ selection. The on-time spectra (black lines), superimposed is the BG (blue points) from the average of the off-time windows and the difference between the two is the resulting β-n prompt energy spectrum (red points). The spectra for the Gd and H-channels are shown separately.

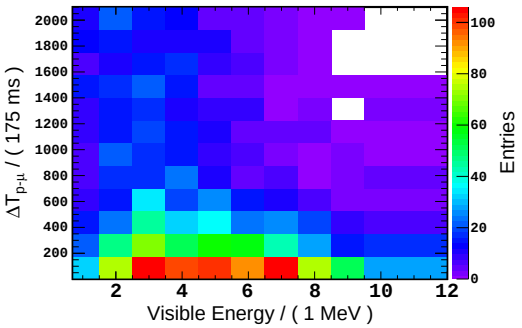

(a) Although the $\Delta T_{p\text{-}\mu}$ distribution is known to 16.1 s, only the first 2.1 s is shown. The build-up of events at small $\Delta T_{p\text{-}\mu}$ are β-n emitters.

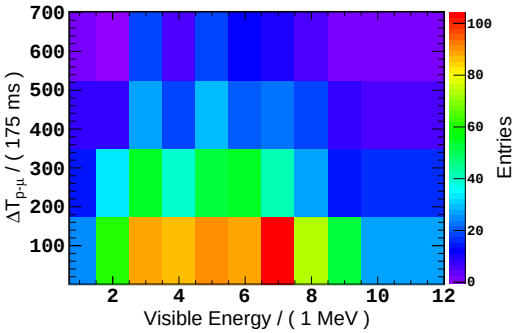

(b) BG subtracted histogram showing β-n events. The information shown in this histogram is used in the ^{8}He fraction fit.

Figure 6.4 The $\Delta T_{p\text{-}\mu}$ and E_{vis} distribution of muon-prompt pairs which satisfy $\mathscr{L}_{Li} > 0.4$. The Gd and H samples are combined to increase the number of statistics. The figure on the right represents the BG subtracted figure on the left and is used to measure the ^{8}He fraction.

from 1.25 ms where only the first four BG subtracted bins will be used in the fit. This brings the total number of bins along the time axis to $B_t = 4$.
The f_{He} fit will be performed over the period $\Delta T_{p\text{-}\mu} \in [1.25, 701.25]$ms which corresponds to the first four time bins in Figure 6.4a. Four separate BG spectra are created, from the same figure, by taking the average of 20 spectra for each, with a window length of 175 ms between $\Delta T_{p\text{-}\mu} \in [2.1, 16.1]$s. The lower limit was chosen to make sure that there are no β-n emitters present in the BG (0.05% remaining) and the upper limit to increase statistics. The BG spectra are subtracted from each time bin and the results are shown in 6.4b.

6.3 ^{8}He Fraction Measurement

This sections describes how the predicted spectra from Section 6.1 are fitted to the data from Section 6.2. The aim of the fit is to estimate the number of ^{9}Li events N^{Li} and the number of ^{8}He events N^{He} in the data sample, from which f_{He} can be calculated. This is achieved by minimising the χ^2 function, whose definition is given and the treatment of the uncertainties using covariance matrices is explained in the following section.

6.3.1 χ^2 Definition

The χ^2 definition is as follows:

$$\chi^2 = \mathbf{y}^{\mathbf{T}} \left(\mathbf{M}_{\mathrm{stat}} + \sum_{n}^{\mathrm{H,Gd}} \sum_{c}^{^{9}\mathrm{Li},^{8}\mathrm{He}} \left(\mathbf{M}_{\mathrm{spec}}^{c,n} + \mathbf{M}_{\mathrm{es}}^{c,n} \right) \right)^{-1} \mathbf{y} \tag{6.1}$$

where $\mathbf{M}$ refers to the whole covariance matrix, including the time distribution such that it is made of $B_t \times B_t$ blocks, where each block consists of B_E bins in the energy plane. The number of time bins is $B_t = 4$ and the number of energy bins is $B_E = 10$. This gives the size to the covariance matrices, shown in Equation 6.1 labelled as $\mathbf{M}$, the proportions $B_t B_E \times B_t B_E$. $\mathbf{M}_{\mathrm{stat}}$ corresponds to the statistical uncertainty explained in Section 6.3.3. $\mathbf{M}_{\mathrm{spec}}$ corresponds to the branching ratio and weak magnetism uncertainty from Section 6.1. $\mathbf{M}_{\mathrm{es}}$ is the covariance matrix corresponding to the energy scale uncertainty explained in Section 6.3.5. There is a covariance matrix for each of the cosmogenic isotopes c corresponding to ^{9}Li and ^{8}He and the spectra for the Gd and H-channels denoted by n. $\mathbf{y} = y_i - \mu_i$ is the difference between the data y_i and expected value μ_i for each bin i explained in Section 6.3.2, whose length is $B_t \cdot B_E$. Later on in this section, $\mathbf{m}$ will refer to a covariance matrix containing only E_{vis} information. It is used as the building block of $\mathbf{M}$ and no time information has been introduced yet.

6.3.2 Expected Value μ

The fit function is minimised with respect to two free parameters, the total number of ^{9}Li events N^{Li} and the total number of ^{8}He events N^{He}, used to evaluate the expected value for each bin i given by μ_i^{Li} and μ_i^{He}. There are two components involved when calculating μ_i^c, the prompt E_{vis} and $\Delta T_{p\text{-}\mu}$. The E_{vis} component is given by the normalised predicted spectrum $S^c(E_{\mathrm{vis}})$. The spectrum is normalised to unity and no energy selection criteria are applied. This has the advantage that no efficiency correction has to be made at a later time to correct for selection cuts. In Chapter 4, the normalisation constant $A = N^c/\tau_c$ has already been evaluated for use in the β-n BG rate measurement when fitting the $\Delta T_{p\text{-}\mu}$ distribution. In the following measurement, the number of events N_k within each time bin k is calculated as follows:

$$\begin{aligned} N_k^c &= \int_T^{T+\Delta B} A \cdot e^{-\frac{t}{\tau_c}} \mathrm{d}t \\ &= N^c \left(e^{-\frac{T}{\tau_c}} - e^{-\frac{T+\Delta B}{\tau_c}} \right) \end{aligned} \tag{6.2}$$

where for brevity t is used instead of $\Delta T_{p\text{-}\mu}$, T is the start time of the bin and ΔB is the bin width. The time and energy components can be combined to give the expected value:

$$\mu_i^c = N^c \cdot \left(e^{-\frac{T}{\tau_c}} - e^{-\frac{T+\Delta B}{\tau_c}} \right) \cdot S^c(E_{\mathrm{vis}}) \tag{6.3}$$

The expected value for bin i is the sum of the two isotopes $\mu_i = \mu_i^{^{9}\mathrm{Li}} + \mu_i^{^{8}\mathrm{He}}$, whose vector is denoted by $\mathbf{y}$.

There is a final consideration to be made, that the data is composed of two separate samples from the Gd and H-channels and that there is a predicted spectra for each. This can be treated in two ways, either the Gd and H data samples can be fitted separately or they can be combined to increase the statistics and possibly the sensitivity. For the scenario when they are fitted together, an extra factor is needed corresponding to the fraction of events F_n in each sample. This is calculated by performing a BG subtraction on the Gd and H data as shown in Figure 6.3 and then evaluating the fraction. This was found to be $F_{\mathrm{Gd}} = 0.409$ and $F_{\mathrm{H}} = 0.591$.

6.3.3 Statistical Uncertainty

The statistical uncertainty is composed of two parts, arising from the on-time windows and the BG or off-time windows. These can be combined by adding the two covariance matrices for each $\mathbf{M}_{\mathrm{stat}} = \mathbf{M}_{\mathrm{on}} + \mathbf{M}_{\mathrm{off}}$. For the on-time windows, the uncertainty for each bin i is

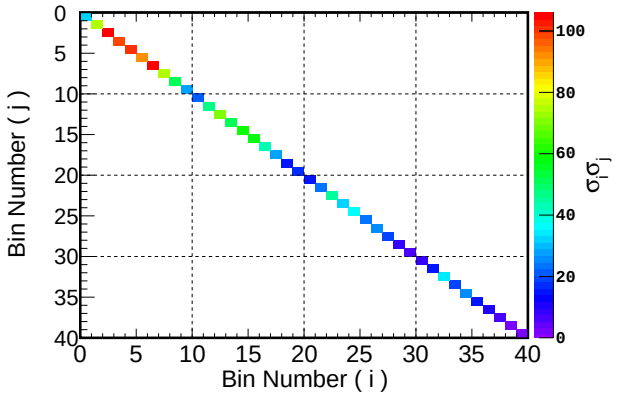

(a) $\mathbf{M}_{\text{on}}$

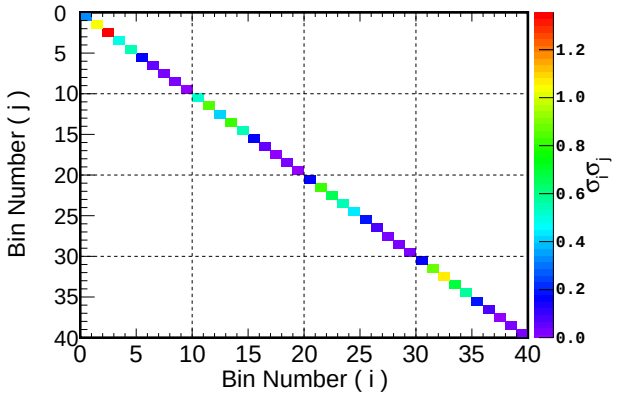

(b) $\mathbf{M}_{\text{off}}$

Figure 6.5 The covariance matrix representing the total statistical uncertainty $\mathbf{M}_{\text{stat}}$ is given by the sum of the uncertainty from the on-time window $\mathbf{M}_{\text{on}}$ shown in the upper plot 6.5a and the off-time window $\mathbf{M}_{\text{off}}$ shown in the lower plot 6.5b. The black dotted lines represent the boundary between each time bin.

calculated using the Poisson distribution where $\sigma_i = \sqrt{n_i}$ and n_i is the number of entries. The covariance matrix $\mathbf{M}_{\text{on}}$ is constructed by setting the diagonal elements to σ_i^2 because bin i is fully correlated to itself. As the statistical uncertainty arises from random fluctuations, no correlation is expected between bins so the off-diagonal elements are set to zero. $\mathbf{M}_{\text{on}}$ can be seen in Figure 6.5a, where σ_i^2 is calculated from the first four time bins in Figure 6.4a.

The BG spectra themselves are calculated in Section 6.2 by taking the average between $\Delta T_{p\text{-}\mu} \in [2.1, 16.1]$ s. This time period is split into windows of length 175 ms and the BG spectrum for bin B_t is taken as the average of every fourth. This allows the unbiased uncertainty on the mean to be calculated:

$$\sigma_i^2 = \frac{\sum_m^{20}(x_{m,i} - \bar{x}_i)^2}{20 \cdot (20-1)} \tag{6.4}$$

The corresponding covariance matrix can be seen in Figure 6.5b, where each time bin is separated by a black dotted line. The values are different between all of the time bins as different BG spectra have been created for each.

6.3.4 Prediction Uncertainty

The creation of the covariance matrices containing the uncertainty on the spectrum prediction has been explained in Section 6.1 and is shown in Figure 6.6a and Figure 6.6b for ^{9}Li and ^{8}He respectively. For each isotope there are 2 blocks of matrices separated by black dotted lines where each line represents the boundary between the spectra created using the Gd and H selection cuts. Each cosmogenic isotope's covariance matrix can be represented by the following:

$$\mathbf{m}_{\text{spec}}^{\text{Gd,H}} = \left(\begin{array}{c|c} \sigma_g^2 & \text{covariance}(g,h) \\ \hline \text{covariance}(h,g) & \sigma_h^2 \end{array} \right) \tag{6.5}$$

where the on-diagonals represent the covariance matrix for each spectrum whilst the off-diagonals contain the covariance of the two. g and h are used to represent Gd and H respectively when describing the covariance matrices and $\mathbf{m}$ is used to represent a single time bin. There are 140 bins for each block, each of which has a bin width of 0.1 MeV and $E_{\text{vis}} \in [0, 14]$ MeV.

Figure 6.6 needs to be modified to represent the binning used for the data which is made up of 10 bins with $E_{\text{vis}} \in [0.7, 12]$ MeV. This is done separately for each block within the covariance matrix by combining the contents of the bins corresponding to each new bin. The new covariance matrices are shown in Figure 6.7.

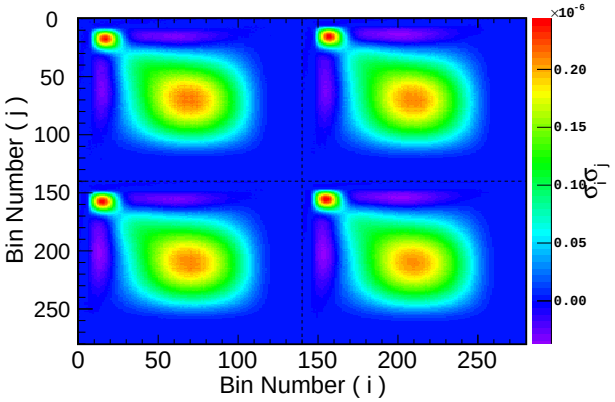

(a) ^{9}Li

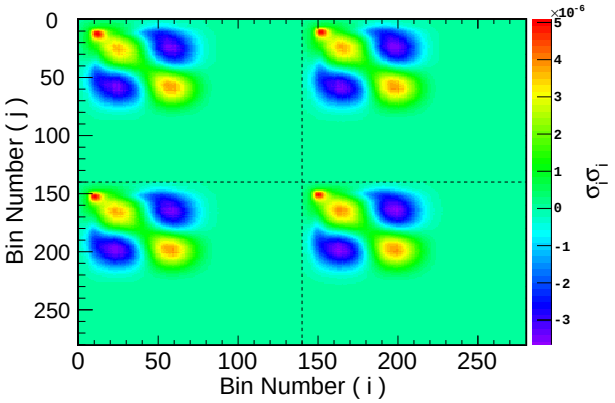

(b) ^{8}He

Figure 6.6 The full covariance matrices containing the uncertainties on the predicted spectrum for ^{9}Li shown in 6.6a and ^{8}He shown in 6.6a. The black dotted lines represent the boundaries between the spectra selected using Gd or H selection cuts. The 140 bins in each block correspond to $E_{\text{vis}} \in [0, 14]$ MeV and have a width of 0.1 MeV. From [86]

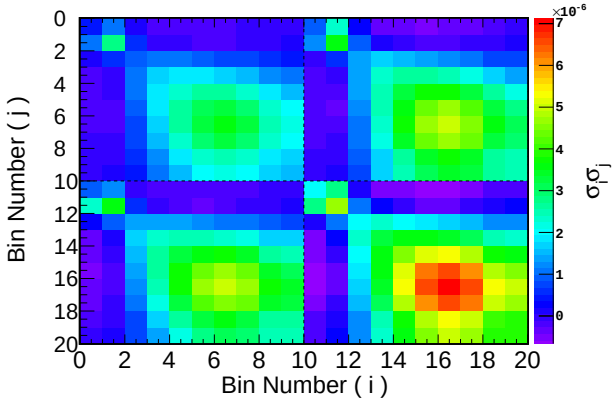

(a) ^{9}Li

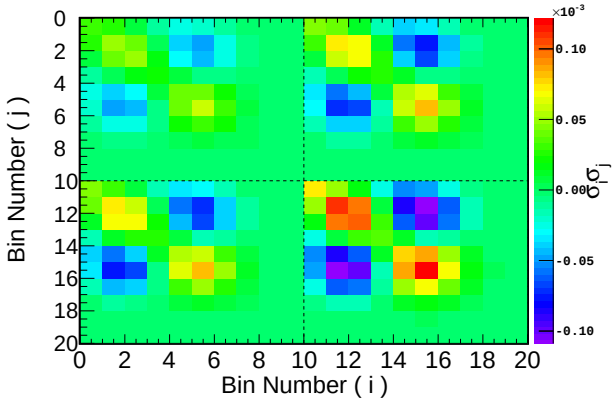

(b) ^{8}He

Figure 6.7 The reduced covariance matrices containing the uncertainties on the predicted spectrum for ^{9}Li shown in Figure 6.7a and ^{8}He in Figure 6.7a. The content in each bin is the sum of the corresponding bins from the full covariance matrix shown in Figure 6.6 and each block represents the bin widths used in the data. The black dotted lines represent the boundary between the spectra created using the Gd and H selection criteria.

The reduced covariance matrices in Figure 6.7 represent each cosmogenic isotope, however they need to be combined into one matrix of size $B_E \times B_E$ to represent each time bin. This can be done by "collapsing the matrix". Each covariance matrix is currently represented as follows:

$$\mathbf{m}^{c}_{\text{spec}} = \left(\begin{array}{ccc|ccc} \sigma^2_{g_1} & \cdots & \sigma_{g_1}\sigma_{g_{B_E}} & \sigma_{g_1}\sigma_{h_1} & \cdots & \sigma_{g_1}\sigma_{h_{B_E}} \\ \vdots & \ddots & \vdots & \vdots & \ddots & \vdots \\ \sigma_{g_1}\sigma_{g_{B_E}} & \cdots & \sigma^2_{g_{B_E}} & \sigma_{g_{B_E}}\sigma_{h_1} & \cdots & \sigma_{g_{B_E}}\sigma_{h_{B_E}} \\ \hline \sigma_{g_1}\sigma_{h_1} & \cdots & \sigma_{g_{B_E}}\sigma_{h_1} & \sigma^2_{h_1} & \cdots & \sigma_{h_1}\sigma_{h_{B_E}} \\ \vdots & \ddots & \vdots & \vdots & \ddots & \vdots \\ \sigma_{g_1}\sigma_{h_{B_E}} & \cdots & \sigma_{g_{B_E}}\sigma_{h_{B_E}} & \sigma_{h_1}\sigma_{h_{B_E}} & \cdots & \sigma^2_{h_{B_E}} \end{array}\right) \tag{6.6}$$

where the black lines separate the blocks corresponding to the Gd and H spectra. The current normalisation of the covariance matrix is such that each spectrum is normalised to one. It is necessary, before collapsing the four blocks into a single block to multiply the matrix by the correct factor to normalise the Gd and H spectra into their correct proportions. This is done by multiplying the terms in the matrix by a combination of F_g and F_h as shown below:

$$\mathbf{m}^{c}_{\text{spec}} = \left(\begin{array}{ccc|ccc} F_g^2\sigma^2_{g_1} & \cdots & F_g^2\sigma_{g_1}\sigma_{g_{B_E}} & F_g\sigma_{g_1}F_h\sigma_{h_1} & \cdots & F_g\sigma_{g_1}F_h\sigma_{h_{B_E}} \\ \vdots & \ddots & \vdots & \vdots & \ddots & \vdots \\ F_g^2\sigma_{g_1}\sigma_{g_{B_E}} & \cdots & F_g^2\sigma^2_{g_{B_E}} & F_g\sigma_{g_{B_E}}F_h\sigma_{h_1} & \cdots & F_g\sigma_{g_{B_E}}F_h\sigma_{h_{B_E}} \\ \hline F_g\sigma_{g_1}F_h\sigma_{h_1} & \cdots & F_g\sigma_{g_{B_E}}F_h\sigma_{h_1} & F_h^2\sigma^2_{h_1} & \cdots & F_h^2\sigma_{h_1}\sigma_{h_{B_E}} \\ \vdots & \ddots & \vdots & \vdots & \ddots & \vdots \\ F_g\sigma_{g_1}F_h\sigma_{h_{B_E}} & \cdots & F_g\sigma_{g_{B_E}}F_h\sigma_{h_{B_E}} & F_h^2\sigma_{h_1}\sigma_{h_{B_E}} & \cdots & F_h^2\sigma^2_{h_{B_E}} \end{array}\right) \tag{6.7}$$

Now that the matrix is normalised correctly, there is no need to worry about the fraction of events from the Gd or H selection, it is enough to collapse this into a single $B_E \times B_E$ matrix and normalise it to the expected number of events. To collapse the matrix, the four blocks are added together as shown below, where $F_c\sigma_c$ has been replaced by Σ_c:

$$\mathbf{m}^{c}_{\text{spec}} = \begin{pmatrix} \Sigma^2_{g_1}+\Sigma^2_{h_1}+2\Sigma_{g_1}\Sigma_{h_1} & \cdots & \Sigma_{g_1}(\Sigma_{g_{B_E}}+\Sigma_{h_{B_E}})+\Sigma_{h_1}(\Sigma_{g_{B_E}}+\Sigma_{h_{B_E}}) \\ \vdots & \ddots & \vdots \\ \Sigma_{g_1}(\Sigma_{g_{B_E}}+\Sigma_{h_{B_E}})+\Sigma_{h_1}(\Sigma_{g_{B_E}}+\Sigma_{h_{B_E}}) & \cdots & \Sigma^2_{g_{B_E}}+\Sigma^2_{h_{B_E}}+2\Sigma_{g_{B_E}}\Sigma_{h_{B_E}} \end{pmatrix} \tag{6.8}$$

This can be thought of as being equivalent to the standard addition of Gaussian uncertainties:

$$\begin{aligned}\sigma_z^2 &= \sigma_x^2 + \sigma_y^2 + 2\rho\sigma_x\sigma_y \\ &= \sigma_x^2 + \sigma_y^2 + 2\mathrm{cov}(x,y)\end{aligned} \tag{6.9}$$

for the function $z = x + y$, where x and y represent the covariance matrix for either the Gd or H spectrum.

The full covariance matrix corresponding to all four time bins can now be constructed. As the spectra are the same for each time bin, full correlation is assumed between them and the matrix is constructed such that $\mathbf{m}^c_{\mathrm{spec}}$ is the same in each block. The covariance is then normalised to the expected number of events by multiplying the bin (i,j) by $\mu^c_i\mu^c_j$ where the expected value μ is given by Equation 6.3. The corresponding covariance matrices $\mathbf{M}^c$ are shown in Figure 6.8 where they have been normalised to the best fit results from Section 6.3.6. The black dotted lines represent the boundary between each time bin and a clear decrease in the average bin content can be observed moving through the blocks towards higher bin number and therefore larger $\Delta T_{p\text{-}\mu}$.

6.3.5 Energy Scale Central Values and Uncertainty

Having prepared the data, MC spectra, and covariance matrices containing the statistical and predicted uncertainty, a ^{8}He fraction fit could now be performed. However, there is still one more uncertainty to take into consideration. This is the uncertainty on the energy scale whose treatment is similar to that described in Sections 3.2.4.5 and 3.7.2 for the IBD candidates, except that here the LNL is calculated for electrons instead of positrons and a covariance matrix is constructed instead of using nuisance parameters.

The energy scale uncertainty is composed of the stability, uniformity and non-linearity components, whose combination involves a change in the energy scale by applying a correction to MC events called the Central Value (CV). This will be explained in the first part of this section. Later, the creation of the covariance matrices from the energy scale uncertainties on the CVs will be explained.

6.3.5.1 Definition of Central Values

Most of the elements in the uncertainty on the energy scale have already been calculated for the $\sin^2(2\theta_{13})$ measurement described in Section 3.2.4.5. The MC CVs and uncertainties are

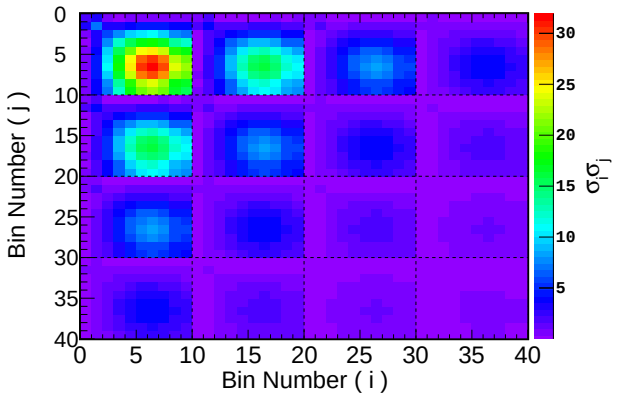

(a) $\mathbf{M}^{\mathrm{Li}}_{\mathrm{spec}}$

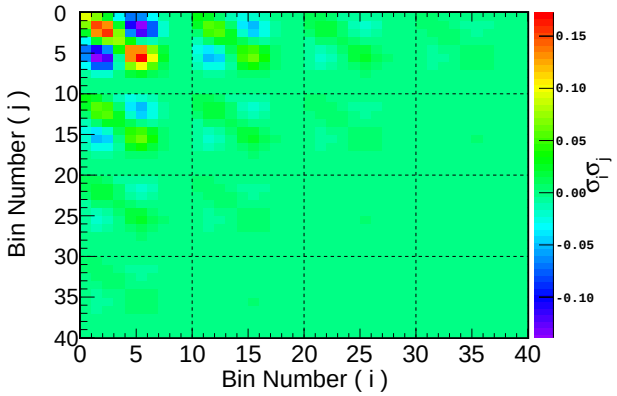

(b) $\mathbf{M}^{\mathrm{He}}_{\mathrm{spec}}$

Figure 6.8 The full covariance matrices for the uncertainty on the predicted spectra for all four time bins. $\mathbf{M}^{\mathrm{Li}}_{\mathrm{spec}}$ is shown in Figure 6.8a and $\mathbf{M}^{\mathrm{He}}_{\mathrm{spec}}$ in Figure 6.8b. They are normalised to N^{Li} and N^{He} given by the best fit results from Section 6.3.6. The black dotted lines represent the boundaries between time bins. As the covariance matrices are the same for each time bin except for the normalisation due to the time distribution, the off-diagonal blocks contain the correlation between each and are non-zero.

calculated as follows [87]:

$$E_{\text{fit}}^{MC} = E_{\text{vis}}^{MC} \cdot LNL \cdot stab./unifor. \cdot QNL \tag{6.10}$$

$$= E_{\text{vis}}^{MC} \cdot \left(\frac{\overline{a}_{LNL}}{E_{\text{vis}}^{MC}} + \overline{b}_{LNL} \right) \cdot b_{st/u} \cdot (b_{QNL} + c_{QNL}.E_{\text{vis}}^{MC}) \tag{6.11}$$

where the stability, uniformity, QNL and LNL are explained in Section 3.2.4. This can be re-arranged to give something similar to Equation 3.15:

$$E_{\text{fit}}^{MC} = a'_{CV} + b'_{CV} \cdot E_{\text{vis}}^{MC} + c'_{CV} \cdot (E_{\text{vis}}^{MC})^2 \tag{6.12}$$

where each CV is given by [87]:

$$\begin{aligned} a'_{CV} &= \overline{a}_{LNL} \cdot b_{st/u} \cdot b_{QNL} \\ b'_{CV} &= \overline{a}_{LNL} \cdot b_{st/u} \cdot c_{QNL} + \overline{b}_{LNL} \cdot b_{st/u} \cdot b_{QNL} \\ c'_{CV} &= \overline{b}_{LNL} \cdot b_{st/u} \cdot c_{QNL} \end{aligned} \tag{6.13}$$

All of the parameters and their uncertainties have been evaluated for the IBD analysis and they are applicable to the energy scale uncertainty in this section. The only exception is the LNL, whose discrepancy between MC and data is because the Light Yield (LY) and Birk's quenching parameter k_B[4] aren't tuned in the MC scintillator. The LNL is particle dependent and although it was evaluated for positrons in the IBD $\sin^2(2\theta_{13})$ measurement, it hadn't been evaluated for electrons. The following section explains the evaluation of the LNL correction for electrons and the creation of $\mathbf{M}_{\text{es}}$.

6.3.5.2 Light Nonlinearity (LNL)

Figure 3.5 in Section 3.2.4.5 shows the remaining discrepancy between the MC and data after the QNL correction is made. As the discrepancy between the visible energy of the H and Gd neutron capture peaks, normalised to the number of γ's is the same, the disparity is thought to arise from the scintillator modelling. The default MC, used to generate all the MC described in this thesis, uses LY $= 8152\,\text{photons}\,\text{MeV}^{-1}$ and Birk's constant $k_B = 0.202\,\text{mm}\,\text{MeV}^{-1}$ for the NT scintillator. Combinations of (k_B,LY) were varied at random and calibration source MC generated using these parameters. Four combinations that reduced the discrepancy between data and MC in Figure 3.5 were chosen as they best represent the data. ^{252}Cf was generated in the NT center using these four combinations and

[4] Scintillation is dependent on the particle type and energy [88].

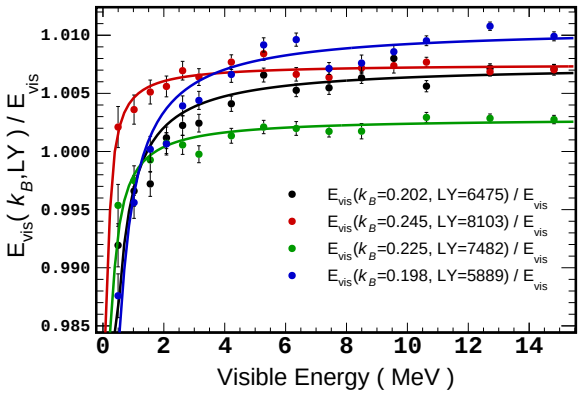

Figure 6.9 Mono-energetic electrons produced at various energies for four combinations of (k_B, LY) that best match the data. After extracting the PE to MeV factor by generating ^{252}Cf MC their visible energy is evaluated and the ratio to the visible energy of the default MC E_{vis} is shown. The average of the parameters from a fit to the four curves gives the LNL correction.

the PE to MeV factor extracted for each using the neutron capture peak on H. For each combination of (k_B, LY), mono-energetic electrons were created between 0.5 and 14 MeV and the visible energy calculated using the PE to MeV factor already extracted. Taking the ratio of the visible energy from the default combination of (k_B, LY) labelled E_{vis} in Figure 6.9 to the combinations that best match the data gives four separate curves. Each curve is fitted with the function $f(E_{\text{vis}}) = a/E_{\text{vis}} + b$. The average value of a is $\overline{a}_{LNL} = -0.0083 \pm 0.0053$ and the average value for b is $\overline{b}_{LNL} = 1.0071 \pm 0.0032$ where the errors are from the RMS of the values. The correlation coefficient between a and b is calculated using the standard formula [22]:

$$\rho_{ab} = \frac{\text{cov}(a,b)}{\sigma_a \sigma_b} \tag{6.14}$$

and evaluated to be $\rho_{ab} = -0.68$.

6.3.5.3 Calculation of the Central Values

The CVs forming the correction to the MC visible energy described in Equation 6.12 are evaluated separately for the Gd and H data samples. The liquid scintillator properties are different in the GC and NT, and although the LNL has been evaluated in the NT, it has not been done for the GC. The calculation of a'_{CV}, b'_{CV} and c'_{CV} is simple following the relationships given in Equation 6.13 and the values calculated in Section 3.2.4 are displayed

Table 6.1 Energy scale values and their corresponding uncertainties. From [87]

	CV	Uncertainty
$b_{st/u}$	1	0.62 %
b_{QNL}	1.004	0.36 %
c_{QNL}	$-0.0001\,\mathrm{MeV}^{-1}$	$0.06\,\%\,\mathrm{MeV}^{-1}$

in Table 6.1. The corresponding correlation matrix is:

$$\begin{pmatrix} \rho_{b_{st/u}b_{st/u}} & \rho_{b_{st/u}b_{QNL}} & \rho_{b_{st/u}c_{QNL}} \\ \rho_{b_{QNL}b_{st/u}} & \rho_{b_{QNL}b_{QNL}} & \rho_{b_{QNL}c_{QNL}} \\ \rho_{c_{QNL}b_{st/u}} & \rho_{c_{QNL}b_{QNL}} & \rho_{c_{QNL}c_{QNL}} \end{pmatrix} = \begin{pmatrix} 1 & 0 & 0 \\ 0 & 1 & -0.6 \\ 0 & -0.6 & 1 \end{pmatrix}$$

The uncertainties on the central values are evaluated analytically by generating random values of each component, such as stability etc according to their uncertainties and correlations and observing the effect on the CVs.

The energy scale uncertainty is further simplified by estimating an effective linear uncertainty [87] on b'_{CV} which is a good approximation for the uncertainties on a'_{CV} and c'_{CV} as well. It is calculated by randomly throwing the parameters a'_{CV}, b'_{CV} and c'_{CV} according to their uncertainties and taking the weighted average over the shape of the visible energy spectrum.

Gadolinium Spectra For the Gd spectra the energy scale parameters in Table 6.1 are combined with the LNL parameters in Section 6.3.5.2 to give the central values a'_{CV}, b'_C and c'_{CV} and their uncertainties as:

$$\begin{aligned} a'_{CV} &= -0.0083 \pm 0.0053\,\mathrm{MeV} \\ b'_{CV} &= 1.0111 \pm 0.0079 \\ c'_{CV} &= -0.0001 \pm 0.0006\,\mathrm{MeV}^{-1} \end{aligned}$$

and their corresponding correlations are:

$$\begin{pmatrix} \rho_{a'a'} & \rho_{a'b'} & \rho_{a'c'} \\ \rho_{b'a'} & \rho_{b'b'} & \rho_{b'c'} \\ \rho_{c'a'} & \rho_{c'b'} & \rho_{c'c'} \end{pmatrix} = \begin{pmatrix} 1 & -0.287 & 0.003 \\ -0.287 & 1 & -0.277 \\ 0.003 & -0.277 & 1 \end{pmatrix}$$

The effective linear uncertainty is calculated using these parameters for both the ^{9}Li and ^{8}He spectra, giving an uncertainty on b'_{CV} of $\sigma_{\mathrm{Gd}} = 0.76\,\%$, and the uncertainties on a'_{CV} and c'_{CV} are zero. It should be noted that the parameters a'_{CV}, b'_{CV} and c'_{CV} form the central values for the predicted spectrum and must always be applied to the MC visible energy spectrum.

Hydrogen Spectra The composition of the liquids in the GC is different to that in the NT and as such the LY and k_B have different values in the detector modelling and therefore the LNL may be different for this data set. The LNL has not been evaluated for the GC and as such the corresponding parameters are set to $a_{LNL} = 0$ and $b_{LNL} = 1$. To allow the χ^2 fit more freedom to find the correct LNL correction the uncertainties on the LNL parameters are set to cover two times the allowed positive and negative deviation of the parameters from the Gd LNL correction [87]. This gives $\sigma(a^{H}_{LNL}) = 0.0272$ and $\sigma(b_{LNL}) = 0.0206$ and the central values:

$$
\begin{aligned}
a'_{CV} &= 0.0 \pm 0.0273\,\mathrm{MeV} \\
b'_{CV} &= 1.004 \pm 0.0219 \\
c'_{CV} &= -0.0001 \pm 0.0006\,\mathrm{MeV}^{-1}
\end{aligned}
$$

with their corresponding correlations:

$$
\begin{pmatrix}
\rho_{a'a'} & \rho_{a'b'} & \rho_{a'c'} \\
\rho_{b'a'} & \rho_{b'b'} & \rho_{b'c'} \\
\rho_{c'a'} & \rho_{c'b'} & \rho_{c'c'}
\end{pmatrix}
=
\begin{pmatrix}
1 & 0 & 0 \\
0 & 1 & -0.103 \\
0 & -0.103 & 1
\end{pmatrix}
$$

The effective linear uncertainty is estimated to be $\sigma_{\mathrm{H}} = 2.46\,\%$.
To summarise, the energy scale uncertainty on b'_{CV} for the Gd and H spectra is:

$$
\begin{aligned}
\sigma_{\mathrm{G}} &= 0.76\,\% \\
\sigma_{\mathrm{H}} &= 2.46\,\%
\end{aligned}
$$

6.3.5.4 Covariance Matrices

It is assumed that any correlation between the H and Gd energy scales, which would be the components excluding the LNL, is small and therefore negligible. However, full correlation is assumed between the ^{9}Li and ^{8}He spectra within each data set as the energy scale is the same in each case. For the sake of brevity, I will only talk about the procedure for the Gd data, however the same procedure is used for the H data set. To keep in line with the

covariance matrices produced for the predicted spectra, a congruous binning of 0.1 MeV was used as each spectrum extends from 0 to 140 MeV, corresponding to 140 bins. This allows the matrix to be rebinned relatively easily as explained in Section 6.3.4 and gives freedom in case the visible energy bin sizes are altered. A fully correlated covariance matrix $\mathbf{m}_{es}^{\mathrm{Gd,H}}$ between the ^{9}Li and ^{8}He spectra should have the dimensions $(2\cdot 140\times 2\cdot 140)$ and contain (2×2) blocks of matrices represented by:

$$\mathbf{m}_{\mathrm{es}}^{\mathrm{Gd,H}} = \left(\begin{array}{c|c} \sigma^2_{\mathrm{Li}} & \mathrm{covariance(Li,He)} \\ \hline \mathrm{covariance\ (He,Li)} & \sigma^2_{\mathrm{He}} \end{array}\right) \tag{6.15}$$

where σ^2_{Li} and σ^2_{He} are the blocks corresponding to each individual spectrum whilst the off-diagonal elements include the correlation, or the covariance between the two.
To create the covariance matrices, the CVs a'_{CV}, b'_{CV} and c'_{CV} using Equation 6.12 are applied to the predicted spectra. As the predicted spectra were received in the format of a binned histogram, a tree[5] of events was created using RooFit [89] which interpolated between the bin entries to create a tree of E_{vis} information. Minimal discrepancy was found between the interpolated tree of events and the original histogram of the predicted spectra. A tree of events is needed as the CVs have to be applied on an event by event basis, and later b'_{CV} is varied according to its uncertainty to create the covariance matrix. Histograms of the event trees with the CVs applied are called the *central* histograms.
A random draw is now made for the effective linear uncertainty on b'_{CV} following a Gaussian distribution centred around zero whose σ equals the calculation in 6.3.5.3 called $\Delta b'$. Histograms are created with the central values a'_{CV}, $(b'_{CV}+\Delta b')$ and c'_{CV} called the *shifted* histograms. A vector difference of the two histograms shown in Equation 6.16 is given by Δ_i =*shifted-central* histograms, where the first 140 bins represent the ^{9}Li spectrum and the second 140 the ^{8}He spectrum.

$$\Delta_i = \begin{pmatrix} \sigma_{\mathrm{Li}_1} \\ \vdots \\ \sigma_{\mathrm{Li}_{B_E}} \\ \sigma_{\mathrm{He}_1} \\ \vdots \\ \sigma_{\mathrm{He}_{B_E}} \end{pmatrix} \tag{6.16}$$

$\Delta_i\cdot\Delta_j$ is added to each element of the covariance matrix such that $\mathbf{m}_{ij}=\mathbf{m}_{ij}+\Delta_i\Delta_j$. The process of throwing for a new value of b'_{CV} and seeing its effect on the spectrum compared to

[5] A tree here refers to the system of storing events in ROOT

the CVs is repeated 5000 times, after which the average is taken by dividing the covariance matrix with this number. The fractional covariance matrix, or a matrix normalised to unity, is created by dividing each block by the number of events in each CV histogram squared. For example, if the number of events in the ^{9}Li *central* histogram is n_{Li}, the upper left block shown in 6.15 is divided by n_{Li}^2, where the off-diagonals are divided by $n_{\mathrm{Li}}n_{\mathrm{He}}$. The corresponding covariance matrices are shown in Figure 6.10a for the Gd energy scale and 6.10b for the H energy scale. The blocks representing each cosmogenic isotope are separated by black dotted lines. Below those figures, Figures 6.10c and 6.10d show the same

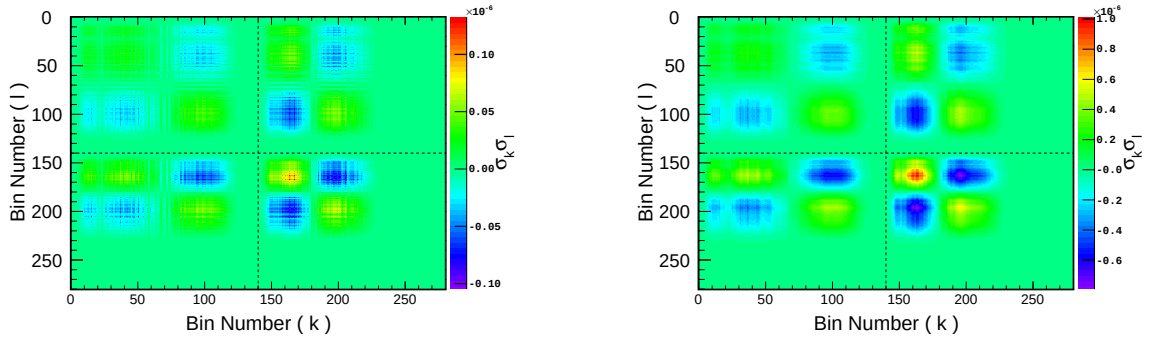

(a) $\mathbf{m}^{\mathrm{Gd}}$ **(b)** $\mathbf{m}^{\mathrm{H}}$

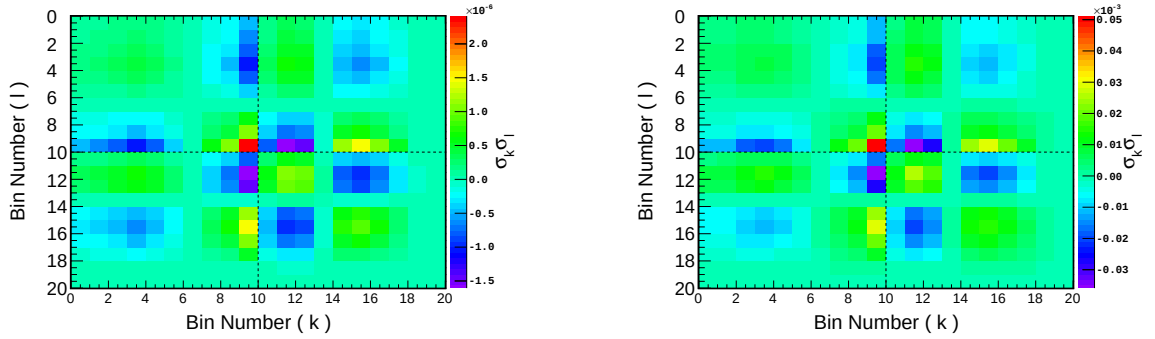

(c) $\mathbf{m}^{\mathrm{Gd}}$ **(d)** $\mathbf{m}^{\mathrm{H}}$

Figure 6.10 The top row of covariance matrices represent the uncertainty on the energy scales for Gd in Figure 6.10a and H in Figure 6.10b. They represent the uncertainty on the full visible energy spectrum between 0 and 140 MeV with a binning of 0.1 MeV. The black dotted lines represent the boundaries between the ^{9}Li (top left block) and ^{8}He (bottom right block) spectra. The matrices on the bottom row represent the full covariance matrices which have been resized in accordance with the binning used for the data and the fit.

covariance matrices, containing the uncertainty on the Gd and H energy scales respectively, but resized in accordance with the binning used for the data.

It is now necessary to construct the full covariance matrix covering all B_t time bins. The Gd and H covariance matrices are first normalised to the fraction of events F_{Gd}^2 and F_{H}^2

respectively. Each bin has to be normalised to the correct number of events before collapsing the matrix into each time bin. This is done by multiplying the bin (i, j) by $\mu_i^c \mu_j^c$ where the expected value μ is given by Equation 6.3. The matrix is then collapsed and placed in the

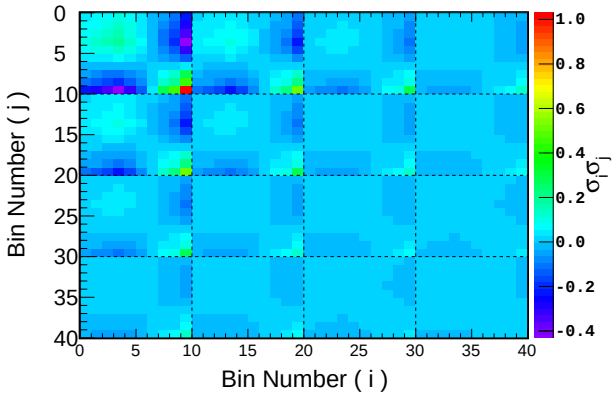

(a) $\mathbf{M}_{\text{es}}^{\text{Li,Gd}} + \mathbf{M}_{\text{es}}^{\text{He,Gd}}$

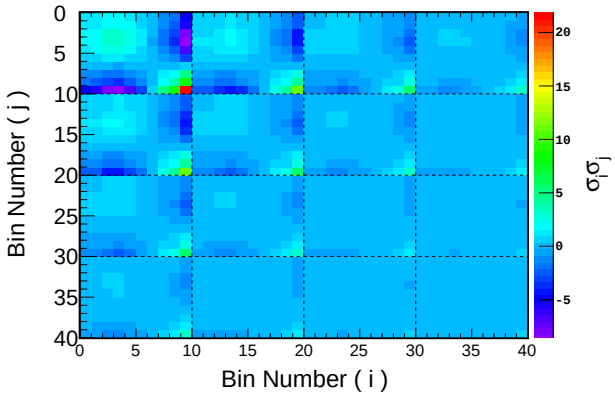

(b) $\mathbf{M}_{\text{es}}^{\text{Li,H}} + \mathbf{M}_{\text{es}}^{\text{He,H}}$

Figure 6.11 The full covariance matrices covering all four time bins are shown where $\mathbf{M}^{\text{Gd}}$ is shown in Figure 6.11a and $\mathbf{M}^{\text{H}}$ in Figure 6.11b. They are normalised to N^{Li} and N^{He} given by the best fit results in Section 6.3.6. The black dotted line represent the boundaries between the time bins. As the covariance matrices are the same for each time bin except for the normalisation due to the time distribution, the off-diagonal blocks contain the correlations between the time bins.

corresponding time bin, where the full covariance matrix can be seen in Figure 6.11. Figure 6.11a and Figure 6.11b show the complete covariance matrices for the uncertainty on the Gd and H energy scale respectively, including the time distribution. They are normalised to the best fit results from Section 6.3.6 and the black dotted lines represent the boundary between the time bins.

6.3.6 Results

The χ^2 value as defined in Equation 6.1 is minimised by changing two free parameters, N^{Li} and N^{He} using a package in ROOT called TMinuit [73]. Each time TMinuit alters one of the free parameters, the covariance matrices are created on the fly, as for example to create $\mathbf{M}_{\mathrm{es}}$ the blocks have to be normalised to N^{Li} and N^{He} before collapsing the matrices into each time bin.

It is also possible to set up the fit such that the two free parameters are the total number of events and the ^{8}He fraction. Preliminary studies showed that this gives exactly the same results as when using the free parameters N^{Li} and N^{He}, as long as the correlation between them is correctly taken into account when calculating the ^{8}He fraction. In this fit N^{Li} and N^{He} are used to simplify the normalisation of the covariance matrices.

The results are shown in Figure 6.12, where Figure 6.12a shows the data summed along the time axis giving the total visible energy spectrum. The black points represent the data, the best fit by the red line which is the sum of the ^{8}He and ^{9}Li spectra using the correct fraction of Gd and H in each case and the pink error bars represent the total uncertainty on the MC, inclusive of the spectrum prediction and energy uncertainty where only the diagonal uncertainties from the covariance matrices are shown. The individual components of the predicted spectra are shown as dotted lines, blue for ^{9}Li and green for ^{8}He. Figure 6.12b shows the time distribution of the data, taken as the sum of all data within each time bin. The data is represented by the black points, the blue line shows the ^{9}Li contribution and the green the ^{8}He contribution and the red their sum.

The best fit was found at $\chi^2/d.o.f$ = 56/38 giving $N^{\mathrm{Li}} = 1310 \pm 88$ events and $N^{\mathrm{He}} = 40 \pm 58$ events where the correlation between them is $\rho = -0.78$. To calculate the ^{8}He fraction of the total, the uncertainty propagation including the correlation needs to be evaluated.

For the sake of brevity, the substitution $l = N^{\mathrm{Li}}$ and $h = N^{\mathrm{He}}$ is made. The ^{8}He fraction is denoted by the function f:

$$f = \frac{h}{l+h} \tag{6.17}$$

The standard definition for calculating the Gaussian uncertainty on a function f is given by:

$$\sigma_f^2 = \left(\frac{\partial f}{\partial l}\right)^2 \sigma_l^2 + \left(\frac{\partial f}{\partial h}\right)^2 \sigma_h^2 + 2\rho \frac{\partial f}{\partial h}\frac{\partial f}{\partial l}\sigma_h \sigma_l \tag{6.18}$$

The two derivatives are evaluated to be:

$$\frac{\partial f}{\partial l} = -\frac{h}{(l+h)^2}, \frac{\partial f}{\partial h} = \frac{l}{(l+h)^2}$$

Table 6.2 A summary of the fit results with the ^{8}He fraction and goodness of fit.

	$\chi^2_{\text{min}}/d.o.f$	N^{Li}	N^{He}	ρ	f_{He} (%)
Gd only	14/18	517 ± 46	31 ± 33	-0.76	5.7 ± 6.9
H only	31/18	799 ± 80	10 ± 48	-0.76	1.2 ± 5.9
Gd+H combined	56/38	1310 ± 88	40 ± 58	-0.78	2.9 ± 4.3

Substituting the derivatives into Equation 6.18 gives the error on the ^{8}He fraction:

$$\sigma_f^2 = \frac{h^2}{(l+h)^4}\sigma_l^2 + \frac{l^2}{(l+h)^4}\sigma_h^2 - 2\rho\frac{hl}{(l+h)^4}\sigma_h\sigma_l \tag{6.19}$$

Using this propagation the ^{8}He fraction is $f_{\text{He}} = (2.9 \pm 4.3)\,\%$.

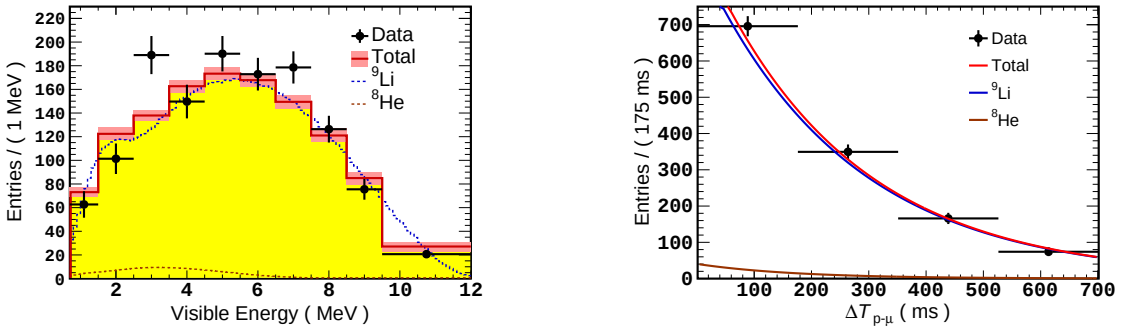

(a) Visible energy spectrum

(b) Time distribution

Figure 6.12 The data used in the fit is represented by the black points where the visible energy spectrum is shown in Figure 6.12a and the time distribution in Figure 6.12b. The ^{9}Li (blue line) and ^{8}He (green line) spectra are shown normalised to the best fit results N^{Li} and N^{He} and corrected to represent the time window used to select the data. The red line shows their sum and in the case of the energy spectrum the pink band represents the uncertainty on the prediction and energy scale. The best fit was found at $\chi^2/d.o.f = 56/38$ with a ^{8}He fraction of $f_{\text{He}} = (2.9 \pm 4.3)\,\%$

The fit was also applied to the H and Gd data sets individually using the same procedure already described, but in the construction of the covariance matrices any correlation between Gd and H is ignored. As the number of events in each case is lower, two time bins of length 350 ms where $\Delta T_{p\text{-}\mu} \in [2, 702]$ ms were used instead of four. The results are summarised in Table 6.2.

6.4 Cosmogenic Yields and Production Rates

Using the fraction measurement from Section 6.3.6, the combined β-n rate measurement from the Gd $\sin^2(2\theta_{13})$ analysis explained in [14] and Chapter 3 can be separated into the individual rates for ^{9}Li and ^{8}He. Using the muon flux at the far detector site already evaluated in a DC publication [77], the rates can be turned into yield and production rate measurements and compared to other experiments which have published these values, Borexino [83] and KamLAND [72].

6.4.1 Yield and Production Rate Calculations

The cosmogenic yields and production rates describe the total number of events $\mathscr{N}_c$, for each cosmogenic radioisotope c that are produced within a fiducial volume V, which in DC is the NT. A measurement of the so called β-n emitters has already been carried out to the highest possible accuracy for the Gd-channel described in Section 3.5.3 as well as the selection inefficiencies. This simplifies the calculation significantly and this rate, as supposed to the less accurate H-channel, is used as the starting point for the yield and rate calculations. The β-n rate measurement gives $\mathscr{R}^{\text{tot}}_{\beta\text{n}} = 2.2^{+0.35}_{-0.27}\,\text{day}^{-1}$ as described in [14]. This is the pure measurement, before it is combined with the Li enriched sample used to decrease the overall error and before the systematic uncertainties are added.
The systematic uncertainties measured in Section 3.5.3 but not yet applied to this β-n rate are now done so. These are the uncertainties due to the lateral distance parameter λ ($\pm 0.5\,\%$), bin size ($\pm 0.9\,\%$) and run length parameter in the fit function ($\pm 0.9\,\%$). The correction due to the ^{8}He fraction in the fit function given in [14] is $-1.4 \pm 1.1\,\%$. This value comes from extrapolating the yields measured in KamLAND to the DC far detector depth giving a ^{8}He fraction of $8 \pm 7\%$, for more information see Section 4.5.4.3. However, as the ^{8}He fraction has been measured in Section 6.3.6 and the effect of the fraction on the final β-n rate has been shown to be linear in Figure 4.9b, the correction and uncertainty can be estimated using linear extrapolation. The correction and uncertainty were evaluated to be $-0.8 \pm 0.7\,\%$. Multiplying the rate by the livetime gives the total number of events $N^{\beta\text{n}} = 1068^{+171}_{-132}$ events. The relationship between the inefficiencies ε_k that reduce the total number $\mathscr{N}_c$ to the observed number of events N_c is given by:

$$\mathscr{N}_c = \frac{N_c}{\prod \varepsilon_k} \tag{6.20}$$

The selection and detection inefficiencies are taken from Section 3.6, which have been evaluated for the IBD candidates. It is assumed that the inefficiencies for the β-n emitters

are the same as for the IBD candidates. In the case of the neutron selection efficiency, this is a good assumption as roughly 90 % of the neutrons go to low lying states of the daughter nucleus and have energies comparable to the IBD neutrons [86].
Corrections are first made for inefficiencies which affect both the ^{9}Li and ^{8}He isotopes, such as the Gd fraction which corrects for neutron captures on Hydrogen not observed with these selection cuts, isolation cuts etc. Further corrections are then made specific to each cosmogenic isotope, such as prompt E_{vis} cuts, muon dead time which removes a different fraction of events for each isotope as they have different lifetimes and non β-n branches which aren't observed using the double coincidence. They are summarised in Table 6.3. The

Table 6.3 List of inefficiency corrections for β-n emitters which at the lower end are specific to each cosmogenic isotope.

	β-n (ε)	
Gd fraction	0.853±0.0008	
Multiplicity Cut	0.9894	
Delayed Muon Veto	0.9986	
FVV, IVV, OV	-	
Selection $\Delta T, \Delta R, E_d$	0.9829±0.0006	
Spill in/out	1.0208	
	^{9}Li (ε)	^{8}He (ε)
Muon dead time	0.9961	0.9942
Prompt E_{vis} cut	0.9914	0.9867
β-n branching ratio	0.508±0.09	0.16±0.01

cosmogenic yields and production rates are then calculated using Equations 5.17 and 5.16 respectively where the muon flux is $\phi_{\mu}^{\text{DC}} = 0.72 \pm 0.04\,\text{s}^{-1}\,\text{m}^{-2}$ [77]. The yields are $Y(^{9}\text{Li}) = 9.78^{+2.14}_{-1.89} \times 10^{-8}\,\mu^{-1}\,\text{g}^{-1}\,\text{cm}^{2}$ and $Y(^{8}\text{He}) = 0.95 \pm 1.4 \times 10^{-8}\,\mu^{-1}\,\text{g}^{-1}\,\text{cm}^{2}$. The production rates are $R(^{9}\text{Li}) = 608^{+133}_{-118}\,\text{kton}^{-1}\,\text{day}^{-1}$ and $R(^{8}\text{He}) = 59 \pm 87\,\text{kton}^{-1}\,\text{day}^{-1}$.

6.4.2 Cross Section

To predict the cosmogenic BG at Borexino and KamLAND, the SPS muon beam at CERN was aimed at liquid scintillator targets and the production rates for different cosmogenic isotopes was measured [82]. Two muon beam energies of 100 GeV and 190 GeV were used to measure the dependence of the cross section on the mean muon energy and an exponent of $\alpha = 0.73 \pm 0.1$ was measured. Although KamLAND and Borexino both only quote the yield and production rates, [82] only measured the cross sections and then predicted the

production rates. It might be of interest to quote the cross section at the DC far detector as a comparison. The cross sections for each isotope are calculated using Equation 5.8 giving $\sigma(^{9}\text{Li}) = 2.27^{+0.50}_{-0.44}\,\mu\text{b}$ and $\sigma(^{8}\text{He}) = 0.22 \pm 0.33\,\mu\text{b}$.

6.4.3 Comparison to Borexino and KamLAND

Borexino [83] and KamLAND [72] are the only experiments that have published comprehensive lists of their cosmogenic radioisotope yields and production rates using liquid scintillator detectors. The KamLAND detector is located at the Kamioka underground laboratory at 2700 m.w.e depth with a mean muon energy of $\langle E_\mu \rangle^{Kam} = 260 \pm 8$ GeV. The Borexino experiment is located at the Gran Sasso National Laboratory at 3800 m.w.e, corresponding to a similar mean muon energy of $\langle E_\mu \rangle^{Bor} = 283 \pm 19$ GeV. In comparison, the Double Chooz far detector is located at a much shallower underground site with a depth of 300 m.w.e and a corresponding mean muon energy of $\langle E_\mu \rangle^{DC} = 63.7 \pm 0.8$ GeV [77].

6.4.3.1 Correction for Carbon Density

All three experiments use organic liquid scintillators for particle detection, but the chemical composition is different for each. Cosmogenic radioisotopes are created by muon interactions with carbon atoms, so if the carbon density is different between experiments, a correction needs to be made as Equation 5.17 does not take this into account. Table 6.4 lists the liquid scintillator composition of KamLAND, Borexino and Double Chooz along with the calculated number of carbon atoms per 100 ton and the corresponding correction factor n_C^{DC}/n_C^{exp}, where *exp* denotes the KamLAND or Borexino experiment. The ^{9}Li and ^{8}He yields for Borexino and KamLAND are corrected to the Double Chooz carbon density and plotted against the mean muon energy in Figure 6.13. The relatively low mean muon energy of the Double Chooz far detector compared to KamLAND and Borexino gives a good anchor point for a fit between all three for the power law exponent α as $Y_c \propto \langle E_\mu \rangle^{\alpha}$. A fit to the three ^{9}Li measurements using Equation 5.19 gives the result $\alpha = 0.64 \pm 0.15$ and is represented on the plot by the black line where the red shading corresponds to the 1σ uncertainty on the fit. It is calculated using the standard formula for Gaussian uncertainty propagation giving:

$$\sigma_Y = \langle E_\mu \rangle^{\alpha} \sqrt{\sigma_b^2 + \ln(\langle E_\mu \rangle)^2 b^2 \sigma_\alpha^2 + 2\rho\,\sigma_b \sigma_\alpha^2 \ln(\langle E_\mu \rangle)} \tag{6.21}$$

Table 6.4 The liquid scintillator properties for Double Chooz, KamLAND and Borexino. These can be used to calculate the Carbon density per 100 t and therefore the correction to the KamLAND and Borexino yields.

	Double Chooz	KamLAND	Borexino
Composition	Dodecane (80%) $[CH_3(CH_2)_{10}CH_3]$ O-PXE (20%) $[C_{16}H_{18}]$	Dodecane (80%) $[CH_3(CH_2)_{10}CH_3]$ Pseudocumene (20%) $[C_9H_{12}]$	Pseudocumene (100%) $[C_9H_{12}]$
V (m^3)	10.3	1171 ± 25	113.1
m (t)	8.24	913.4	99.6 ± 3.8
ρ_{LS} ($g\,cm^{-3}$)	0.80	0.780 ± 0.001	0.8802
n_C $(C/100t)$	4.31×10^{30}	4.30×10^{30}	4.51×10^{30}
n_C^{DC}/n_C^{exp}	1	1.003	0.956

where σ_b is the uncertainty on b and σ_α is the uncertainty on the power law exponent α. No such fit was applied to the ^{8}He yields as there is only an upper limit from the Borexino experiment.

6.4.3.2 Including the Hagner Measurement

Also shown is the measurement from Hagner [82] where only the combined ^{9}Li and ^{8}He cross section was evaluated at a single muon energy of 190 GeV. The resulting cross section was $\sigma^{Hagn.}_{\text{Li+He}} = 2.12 \pm 0.35\,\mu$b. The yield can be calculated from the cross section using Equation 5.18, however, the cross section is a function of muon energy. In the case of DC, KamLAND and Borexino the muon spectrum is not mono-energetic but has a differential muon rate spectrum explained in Section 5.2. In the Hagner measurement of the cross section a mono-energetic muon beam was used, if a comparison is to be made between Hagner and these experiments, the muon spectrum at a given depth needs to be taken into account. This can be done by including the factor β_α into Equation 5.18. This factor can be calculated numerically by first calculating the depth that a mean muon energy of 190 GeV corresponds to and then estimating the correction β_α at that depth. The depth corresponding to $\langle E_\mu \rangle = 190$ GeV is estimated by calculating $\langle E_\mu \rangle$ for each depth X until the correct energy is found. The mean muon energy is calculated as a function of depth X using Equation 5.14, where the calculation of the differential muon spectrum dN_μ/dE_μ has been explained in Section 5.2. The results can be seen in Figure 6.14, where a depth of $X = 1476$ m.w.e was found to represent $\langle E_\mu \rangle = 190$ GeV. The correction factor β_α can now

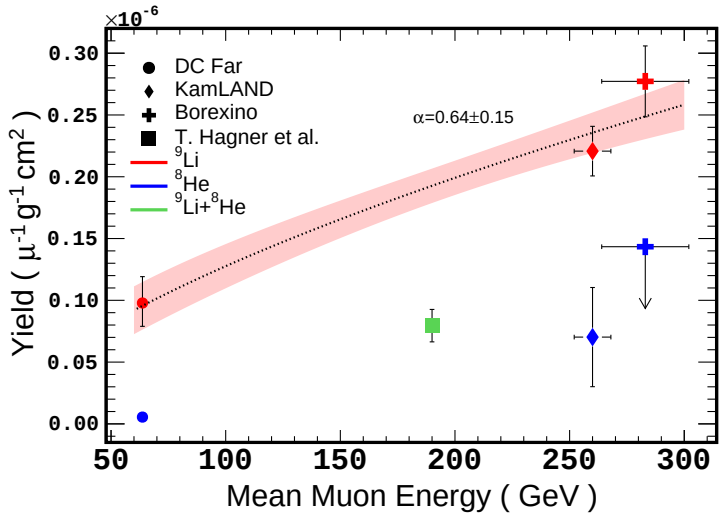

Figure 6.13 Carbon density corrected ^{9}Li and ^{8}He yields for Double Chooz, KamLAND and Borexino. The arrow for the Borexino ^{8}He yield denotes an upper limit. A fit to the ^{9}Li yields gives $\alpha = 0.64 \pm 0.15$. No such fit was applied to the ^{8}He data as there are only two data points.

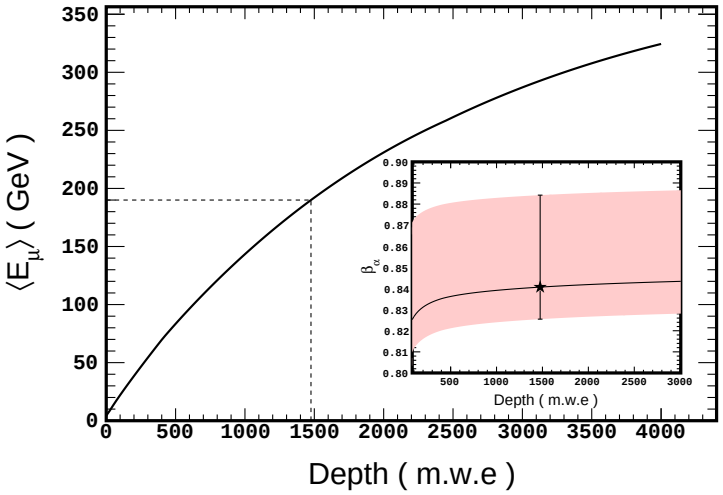

Figure 6.14 The average muon energy calculated at multiple depths. A depth of 1476 m.w.e was found to correspond to a mean muon energy of $\langle E_{\mu} \rangle = 190$ GeV. The inset shows the calculated value of β_{α} at this depth, where the black line represents the α measurement in this chapter and the red band the $\pm 1\sigma$ error band according to its measurement uncertainty. This gives $\beta_{\alpha} = 0.84^{+0.04}_{-0.02}$.

be calculated, including the power law exponent dependence on the muon energy:

$$\beta_\alpha(h) = \frac{\langle E_\mu^\alpha \rangle}{\langle E_\mu \rangle^\alpha} \tag{6.22}$$

This can be solved numerically using the differential muon spectra in Section 5.2. The inset in Figure 6.14 shows the calculated β_α as a function of depth, where the black line corresponds to the α measurement in this chapter, and the red error band corresponds to the $\pm 1\sigma$ on the measurement. This gives $\beta_\alpha = 0.84^{+0.04}_{-0.02}$, which is used to correct the cross section measurement from Hagner, giving a yield of $Y^{Hagn.}_{\mathrm{Li+He}} = 7.68^{+1.32}_{-1.28} \times 10^{-8}\,\mu^{-1}\,\mathrm{g}^{-1}\,\mathrm{cm}^2$. This is represented by the green square marker on Figure 6.14. It would be expected that this point lies above the best fit line given by the measurement of α in this section as it corresponds to the cross section for both ^{9}Li and ^{8}He production, but is much lower. In fact, even the Hagner prediction for the production rate at Borexino $R_{\mathrm{Li+He}} = 0.034 \pm 0.007\,\mathrm{kton}^{-1}\,\mathrm{day}^{-1}$ is much less then the measured value at Borexino $R_{\mathrm{Li}} = 0.083 \pm 0.009\,\mathrm{kton}^{-1}\,\mathrm{day}^{-1}$.

6.5 Conclusion

Using the full data set available from the DC far detector, corresponding to 467.9 and 462.72 days of live time for the Gd and H analyses respectively, a measurement of the ^{8}He fraction was made $f_{\mathrm{He}} = (2.9 \pm 4.3)\,\%$. This fraction measurement allowed the calculation of the yields and production rates for ^{9}Li and ^{8}He separately. The calculated yields are $Y(^9\mathrm{Li}) = 9.78^{+2.13}_{-1.89} \times 10^{-8}\,\mu^{-1}\,\mathrm{g}^{-1}\,\mathrm{cm}^2$ and $Y(^8\mathrm{He}) = 0.95 \pm 1.4 \times 10^{-8}\,\mu^{-1}\,\mathrm{g}^{-1}\,\mathrm{cm}^2$. The production rates are $R(^9\mathrm{Li}) = 608^{+133}_{-117}\,\mathrm{kton}^{-1}\,\mathrm{day}^{-1}$ and $R(^8\mathrm{He}) = 59 \pm 87\,\mathrm{kton}^{-1}\,\mathrm{day}^{-1}$. A fit to these measurements and those from KamLAND and Borexino gives the power law exponent $\alpha = 0.64 \pm 0.15$. This is the first experimental determination of α for ^{9}Li and could be useful for liquid scintillator experiments in the planning phase that wish to evaluate their β-n BG at a given depth. The only other determinations have been made using simulation, one using FLUKA by the KamLAND collaboration $\alpha = 0.801 \pm 0.026$ [72] and one using Geant4 $\alpha = 1.06$ [90]. These are both slightly larger than the measurement made in this chapter, suggesting more ^{9}Li is produced at shallower depths then expected by simulation.

Chapter 7

^{12}B and ^{12}N

7.1 Introduction

The cosmogenic radioisotope ^{12}B is produced in copious amounts in the DC far detector and both KamLAND and Borexino measured its yield as the second highest after ^{11}C. The relatively high endpoint of its spectrum $Q_{\beta^-} = 13.4\,\text{MeV}$ and relatively short lifetime $\tau = 29.1\,\text{ms}$ make it easy to observe in the DC far detector, although only above 4 MeV. Below this energy the signal to background ratio is too small. In the future, the spectrum could be used to cross check the energy scale and check for any disparity between the data and MC. ^{12}N has a lifetime on a similar scale $\tau = 15.9\,\text{ms}$ although its endpoint is significantly higher at $Q_{\text{EC}} = 17.3\,\text{MeV}$, which gives a good handle when it comes to estimating its production rate. The primary processes that produce these radioisotopes are $^{12}\text{C}(n,p)^{12}\text{B}$ and $^{12}\text{C}(p,n)^{12}\text{N}$ which then both decay back into ^{12}C [72]. Figure 7.1 shows the decay schemes for ^{12}B on the left and ^{12}N on the right which undergo β^- and β^+ decay respectively. When the decay isn't to the ground or first state, there is a possibility that the excited ^{12}C* will decay into three α's. The modelling of these decays is explained in Section 7.3 along with the process involved when generating cosmogenic radioisotope decays.

A fit to the data using the generated spectra as the expected values is explained in Section 7.6 and 7.7 for ^{12}B and ^{12}N respectively along with the subsequent yield and production rate calculations.

In Section 7.8 the ^{12}B yield measurement is used in addition to those from KamLAND and Borexino to determine the power law exponent α. This gives the relationship between the yields and the mean muon energy.

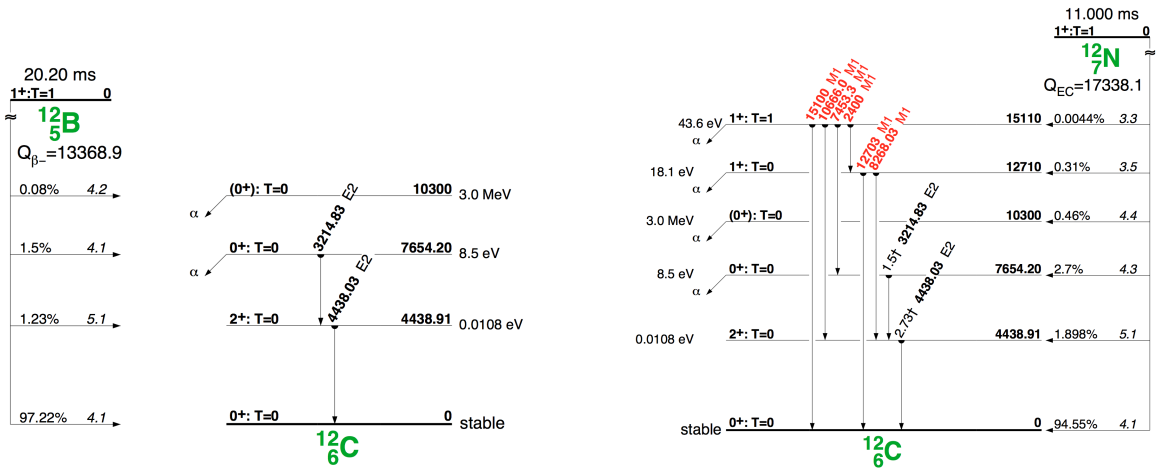

(a) ^{12}B. **(b)** ^{12}N.

Figure 7.1 The decay schemes for ^{12}B and ^{12}N. Source [84]

7.2 Real Radial Distribution

The real radial distribution of ^{12}B and ^{12}N to the parent muon was simulated using FLUKA as described in Section 4.5.2.1. The results are shown in Figure 7.2, where the violet points represent ^{12}B and the green ^{12}N. A fit to the distributions using Equation 4.5 gives $\lambda_{1,^{12}\mathrm{B}} = 7 \pm 1$ mm, $\lambda_{2,^{12}\mathrm{B}} = 905 \pm 7$ mm and $\lambda_{2,^{12}\mathrm{N}} = 549 \pm 21$ mm. The parameters corresponding to the number of events give $N_{1,^{12}\mathrm{B}} = 288 \pm 30$ events, $N_{2,^{12}\mathrm{B}} = 20690 \pm 146$ events and $N_{2,^{12}\mathrm{N}} = 705 \pm 28$ events. The first term in Equation 4.5 corresponding to the shorter average production length is ignored when fitting the ^{12}N distribution as the simulation shows this to be invalid. The simulation shows that ^{12}B is more likely to be produced at larger distances from the parent muon compared to ^{12}N. The average production length of ^{12}B is 905 mm compared to 549 mm for ^{12}N whose average production length is comparable to ^{9}Li and ^{8}He, which are on the order of 600 mm. This is most likely because the main production process for ^{12}B's is a (n, p) reaction on ^{12}C. For ^{12}N, ^{9}Li and ^{8}He main production process is from pions which travel significantly less than neutrons due to their charge. The term corresponding to ^{12}B produced close to the muon track could be due to muon capture where $\mu^- + {}^{12}\mathrm{C} \rightarrow {}^{12}\mathrm{B} + \nu_\mu$.

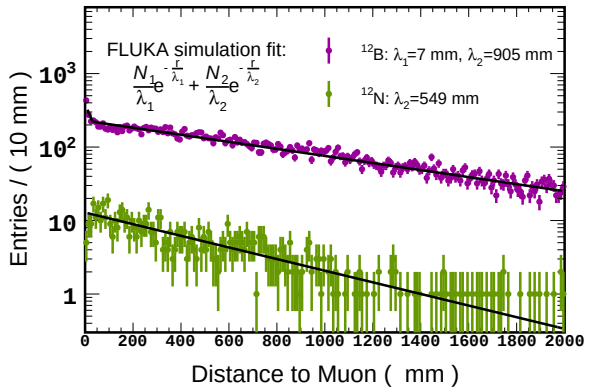

Figure 7.2 FLUKA simulations for the production of ^{12}B and ^{12}N as a function of the distance from the parent muon. A fit of the function shown in the plot gives $\lambda_{1,^{12}\mathrm{B}} = 7 \pm 1$ mm, $\lambda_{2,^{12}\mathrm{B}} = 905 \pm 7$ mm and $\lambda_{2,^{12}\mathrm{N}} = 549 \pm 21$ mm. Data from [74]

7.3 Spectrum Generation

7.3.1 MC Production Chain

The cosmogenic radioisotope spectra are generated using packages incorporated in the Double Chooz Offline Group Software (DOGS) [91, 92]. The chain of packages used is shown in Figure 7.3. The generation begins with DCGenSpec [93] which was already established and contained the necessary knowledge for creating the decays of some radioisotopes. DCGenSpec is fed with data files containing information about the decay

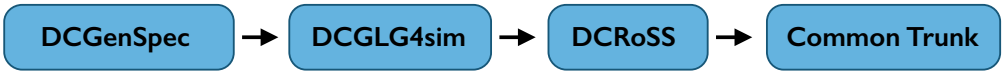

Figure 7.3 The flow chart explaining the process behind cosmogenic radioisotope production.

schemes, including the branching ratios, the particle type, which for electrons and positrons includes the endpoint energies (Q), whilst for heavier particles such as α's the kinetic energy is given and for γ's the energy. DCGenSpec uses this information to create events randomly, creating files with the particle type, momentum and position. This information is then fed into the next package used in MC production, DCGLG4sim. DCGLG4sim reproduces the detector geometry and material properties [94] and is based on the Geant4 framework [63, 64]. The DC Readout System Simulation (DCRoSS) simulates the electronics of the detector and the final stage is the Common Trunk (CT) which applies the same algorithms

used on the data such as position and energy reconstruction. The reconstructed events which come out after the CT can be compared directly to the data.

7.3.2 Beta Decay

The probability $N(p_e)$ of a β particle having momentum between p_e and $p_e + dp_e$ is given by [95]:

$$N(p_e)dp_e = \frac{g^2}{2\pi^3}|\mathscr{M}|^2 F(Z', p_e)(Q - T_e)^2 p_e^2 dp_e \tag{7.1}$$

where $\mathscr{M} = M_{if}$ is the nuclear matrix element of the initial i to final f state and T is the kinetic energy. $F(Z', p_e)$ is the Fermi Function which adds a correction for the Coulomb interaction between the nucleus and emitted β particle and depends on the atomic number of the daughter nucleus Z'. Further functions are included in the beta spectrum generator for electron screening and forbidden decays.

7.3.3 ^{12}B and ^{12}N Generated Spectra

The decay scheme for ^{12}B was already incorporated into DCGenSpec and the scheme for ^{12}N was added using information from [84, 96]. The decay schemes in Figure 7.1 show that on the occasions ^{12}B and ^{12}N decay to the second or higher excited state of ^{12}C*, there is a chance there will be a subsequent decay to ^{8}Be and α:

$$^{12}\mathrm{C} \rightarrow ^{8}\mathrm{Be} + \alpha \tag{7.2}$$

where ^{8}Be is unstable and decays further into two α's

$$^{8}\mathrm{Be} \rightarrow \alpha + \alpha \tag{7.3}$$

This decay chain was not included in the spectrum generator and was added by modelling a sequential decay of 7.2 then 7.3 using relativistic mechanics.

The momentum of ^{8}Be is calculated using 2-body decay. The 4-momentum of the parent ^{12}C particle is $P_C = (M_C, 0)$ and the daughter particles have 4-momenta $P_{Be} = (E_{Be}, \mathbf{p}_{Be})$ and $P_\alpha = (E_\alpha, \mathbf{p}_\alpha)$. Using conservation of momentum $\mathbf{p}_{Be} = -\mathbf{p}_\alpha$ where $|\mathbf{p}| = \mathbf{p}_{Be} = \mathbf{p}_\alpha$, conservation of energy $M_C = E_{Be} + E_\alpha$, substituting the energy mass relation $E^2 = m^2 + p^2$ into the conservation of energy equation and re-arranging gives both the ^{8}Be and α

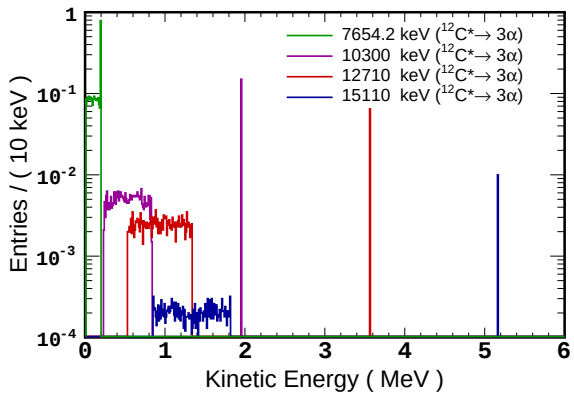

Figure 7.4 The kinetic energy distribution of α's from the decay of ^{12}C*. The kinetic energies are modelled using relativistic kinematics and a sequential decay of $C* \rightarrow Be + \alpha \rightarrow 3\alpha$. The 15.1 MeV decay distribution is exaggerated for the sake of demonstrative purposes, its branching ratio is too small $< 0.0044\,\%$ to be visible otherwise.

momentum in the laboratory frame and in this case the Center of Mass (COM) frame:

$$|\mathbf{p}| = \frac{\sqrt{M_C^4 + M_{Be}^4 + M_\alpha^4 - 2M_C^2M_{Be}^2 - 2M_C^2M_\alpha^2 - 2M_{Be}^2M_\alpha^2}}{2M_C} \tag{7.4}$$

The momentum of the ^{8}Be atom is assigned a direction at random whilst the α particle is given the same momentum but in the opposite direction.

The momenta of the two α particles from the subsequent decay of the ^{8}Be are first calculated in the COM frame. Substituting the mass of the parent and daughter particles into Equation 7.4 gives:

$$|\mathbf{p}| = \frac{\sqrt{M_C^4 - 4M_C^2M_\alpha^2}}{2M_C} \tag{7.5}$$

where the momentum in this case is the same for both α's. A transformation into the laboratory frame is made by calculating the Lorentz boost vector $\beta = -\mathbf{p}_{Be}/E_{Be}$ and applying the corresponding transformation matrix to both α particles. Figure 7.4 shows the kinetic energies of the 3α's after a ^{12}C* decays. Decays from different energy levels of ^{12}C* are represented by different colours. The lines represent the mono-energetic α's from the first decay shown in Equation 7.2 and the top hat distributions at lower energies represent the α's from the subsequent decay of ^{8}Be. The total effect of these decays is expected to be small as α's have a large quenching compared to other ions. This means that the light yield in a scintillator is smaller in the case of α's, where it is approximately one tenth of that from an electron.

After incorporating the excited ^{12}C decays and the decay schemes for ^{12}N into the generator, the produced spectra can be seen in Figure 7.5a where ^{12}B is represented by a violet line and ^{12}N by a green one. These spectra include the detector response and can be used in Section 7.6 to evaluate the expected value which is compared to the data.

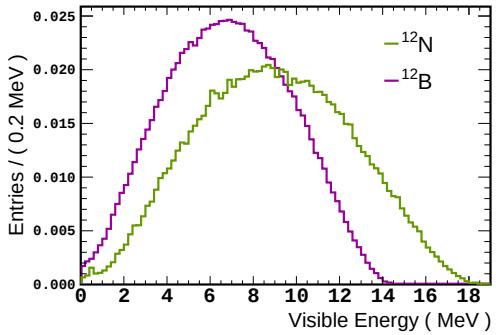

(a) The generated spectra for ^{12}B (violet) and ^{12}N (green)

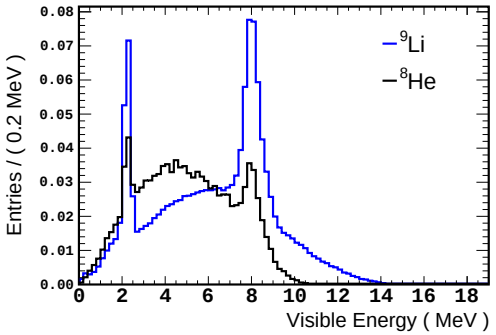

(b) The generated spectra for ^{9}Li (blue) and ^{8}He (black)

Figure 7.5 The generated, cosmogenic radioisotope decay spectra used in the ^{12}B fit to predict the expected value for each bin. They include the detector response and are representative of data.

7.3.4 ^{9}Li and ^{8}He Generated Spectra

The generation of the spectra for the contaminants ^{9}Li and ^{8}He have been explained in Chapter 6. However, these spectra only represent the decays which subsequently emit a neutron, labelled the β-n emitters. They do not include the decays to the ground state of the daughter nucleus. These are generated separately and combined with the β-n spectra from Chapter 6 in the correct proportions. The ground state decays correspond to 45 % and 84 % for ^{9}Li and ^{8}He respectively. In the ^{12}B fit there is no cut on subsequent events, which means that the neutrons following β-decays from ^{9}Li and ^{8}He will also be found in the spectrum. As the binning used is on the order of ms whilst the average capture time for neutrons on Gd is 30 µs a single spectrum is created to take into account the ground state decay, non-ground state decays and the subsequent neutron capture. The observed energy region $E_{\text{vis}} \in [4, 17]$ MeV is above the neutron capture peak on Hydrogen 2.2 MeV. As the ^{9}Li and ^{8}He yields and production rates have already been estimated in Chapter 6, they are used here purely as a contaminant in the ^{12}B yield estimation, so an understanding of the detector response to the neutron capture peak on H is not important.

The ^{9}Li and ^{8}He spectra are created by adding the correct proportions of the ground state decays and β-n decays including the corresponding delayed neutron capture spectra, added in equal proportions to the fraction of β-n decays and including their detection efficiency. The neutron detection efficiency was estimated using MC generated IBD candidates described in Section 3.1. It is given by the ratio of the number of neutrons detected in the FV to the number of prompt β events detected in the FV, where the FV is defined by the spatial cuts described in Section 7.5.2. The efficiency for neutron capture on Gd was estimated to be $\varepsilon_{ndet} = 91.7\,\%$ where the statistical uncertainty is negligible. Figure 7.5b shows the corresponding spectra where ^{9}Li is represented by a blue line and ^{8}He by a black line. The neutron capture peaks are much more dominant in the ^{9}Li spectra because the β-n branching ratio is 49.5 % whilst in the ^{8}He case it is only 16 %.

7.4 Fit Method

To evaluate the yields of each cosmogenic isotope, a BML fit is performed using both the ΔT and E_{vis} information. This approach is used when a Poisson distribution of events is expected in each bin, this means that the number of events in each bin is an integer. This is achieved by including the BG spectrum in the hypothesis θ, instead of performing a BG subtraction as was done for ^{9}Li and ^{8}He in Chapter 6. Starting with a Poisson distribution, the probability P that the number of events n_i in bin i is given by the expectation μ_i is:

$$P(n_i;\mu_i) = \frac{\mu_i^{n_i}}{n_i} e^{-\mu_i} \tag{7.6}$$

This probability is largest when $n_i \approx \mu_i$. To find the model θ that best fits the data set $\mathbf{n}$ the product of all the probabilities, called the likelihood $L(\mathbf{n},;\theta)$ should be maximised. It is defined as follows [22]:

$$L(\mathbf{n};\theta) = \prod_i^N \frac{\mu_i^{n_i}}{n_i} e^{-\mu_i} \tag{7.7}$$

The likelihood function can be normalised such that it follows the χ^2 distribution in the limit of large n_i by using the likelihood ratio λ:

$$\lambda = \frac{L(\mathbf{n};\theta)}{L(\mathbf{n};\mathbf{n})} \tag{7.8}$$

and multiplying by -2 then $-2\ln\lambda \approx \chi^2$. This gives the likelihood function to be minimised:

$$-2\ln\lambda = -2\sum_{i}^{N}\ln\left(\frac{\mu_i^{n_i}}{n_i}e^{-\mu_i}\right) + 2\sum_{i}^{N}\ln\left(\frac{n_i^{n_i}}{n_i}e^{-n_i}\right) \tag{7.9}$$

It is useful to use the negative of the likelihood ratio as most fitters tend to minimise a function, so it is easier to minimise $-2\ln\lambda$ than maximise $2\ln\lambda$.

The expectation value μ_i is estimated using the sum of the cosmogenic isotope spectra created from MC simulations along with the ΔT distribution which follows an exponential according to the isotope's lifetime:

$$\mu_i = \sum_c \mu_i^c + \mu_i^{\mathrm{BG}} \tag{7.10}$$

Where the sum is taken over the cosmogenic radioisotopes c in addition to the expected BG component for each bin i. The definition of μ_i is already given by Equation 6.3 but shown again to give the full picture:

$$\mu_i^c = N^c \cdot \left(e^{-\frac{T}{\tau_c}} - e^{-\frac{T+\Delta B}{\tau_c}}\right) \cdot S^c(E_{\mathrm{vis}}) \tag{7.11}$$

where N^c is the number of events, $\mathrm{S}(E_{\mathrm{vis}})$ is the predicted spectrum generated in Section 7.3, ΔB is the bin width along the time axis and τ_c is the lifetime of the cosmogenic isotope c.

In some situations only a fit to the ΔT distribution is used which follows a similar form to Equation 4.1 but reduced to:

$$f(\Delta T) = \Delta B \cdot \sum_c \frac{N^c}{\tau_c} e^{-\frac{\Delta T}{\tau_c}} + C \tag{7.12}$$

where ΔB is the bin width used to create the ΔT distribution, c is the relevant cosmogenic radioisotope and C is the constant BG.

7.5 Event Classification and Spatial Cuts

In the first part of this section the preliminary selection criteria for muon events and cosmogenic candidates are explained. The second part discusses the FV used in the analysis and the selection of the spatial reconstruction cuts.

7.5.1 Classification of Muons and Cosmogenic Candidates

The preliminary selection of cosmogenic events is explained in Table 7.1. The muon visible energy E^{μ}_{vis} refers to the reconstructed energy in the ID as defined in Section 3.2.4 without the uniformity correction. An event passing the muon veto criteria will induce a dead time of 2 ms which only affects cosmogenic candidates. Muons which only deposit energy in the ID are classified as tagging muons whose ΔT to cosmogenic candidates is used in the fit. Muons that only deposit energy in the IV are thought to be too far away from the FV to create cosmogenic radioisotopes and are called veto muonsand start a deadtime of 2 ms. The rate of veto muons $R^{\text{veto}}_{\mu} = 44.6\,\text{s}^{-1}$ is measured by plotting the time difference between subsequent muons and fitting with the exponential function $e^{-\Delta_{\mu\mu}\cdot R_{\mu}}$ where R_{μ} is the muon rate and $\Delta_{\mu\mu}$ is the time difference between subsequent muons. The rate of tagging muons is $R^{\text{tag}}_{\mu} = 15.9\,\text{s}^{-1}$ and in both measurements the uncertainty from the fit is negligible.

Table 7.1 Preliminary selection criteria for cosmogenic candidates and the definition of vetoing and tagging muons.

Vetoing Muon	
Energy ID	$E^{\mu}_{\text{vis}} > 20\,\text{MeV}$
Charge IV	$q_{\text{IV}} > 3\times10^{4}\,\text{CU}$
Tagging Muon	
Energy ID	$E^{\mu}_{\text{vis}} > 20\,\text{MeV}$
Cosmogenic Event	
Dead Time	$\Delta T(\mu_{\text{veto}}) < 2\,\text{ms}$
Energy ID	$4 < E_{\text{vis}} < 19\,\text{MeV}$
Charge IV	$q_{\text{IV}} < 1\times10^{4}\,\text{CU}$
q_{max}/q_{tot}	< 0.12
σ_t	$< 36\,\text{ns}$
σ_q	$< 464 - 8\sigma_t$ CU
Q_{dev}	$< 3\times10^{4}\,\text{CU}$

A cosmogenic candidate is defined using the criteria in the lowest part of the table where the last four lines represent the LN cuts described in Section 3.3.2.

7.5.2 Spatial Distribution and Fiducial Volume

The spatial distribution of cosmogenic candidates dominated by ^{12}B can be created by performing a BG subtraction of the reconstructed spatial coordinates. The detector

coordinates are given by (x,y,z) and are defined such that $(x=0,y=0,z=0)$ is the center of the ID. In Chapter 6 where the ^{9}Li and ^{8}He yields are measured, the FV is the same as the NT. No spatial cuts are required due to the β-n double coincidence where observation of the delayed neutron capture on Gd, which is only found in the NT, limits the volume to the NT. Corrections are later made for neutrons entering and leaving the NT and the number of β-n candidates which aren't observed when the neutron is captured on H. In this chapter, the individual cosmogenic candidates are selected, so spatial cuts are necessary to limit the FV to the NT only. Including the GC would complicate the calculations as it has a different chemical composition and therefore ^{12}C density. Additionally, the calculation of the yields and production rates is dependent on observing the parent muon, which doesn't have to pass through the FV to produce radioactive isotopes. Section 7.2 shows that they can be produced far away from a muon's flight path, so decreasing the FV will allow a more accurate measurement.

To assess the spatial distribution of cosmogenic radioisotopes, a BG subtraction can be made in spatial reconstruction coordinates using the time difference between the cosmogenic candidate and the muon ΔT. In this section, an on-time window selects events with $\Delta T \in [2,52]$ ms and an off-time window is created by taking the average of ten windows between $\Delta T \in [2.5,3]$ s. An addition visible energy cut of $E_{\text{vis}} < 15$ MeV is applied to remove unnecessary BG events. The difference of the two gives the cosmogenic radioisotope distribution shown in Figure 7.6 by the black points, the MC is represented by a red line. Figure 7.6a displays the reconstructed height distribution given by z in the detector coordinate system and Figure 7.6b shows the radius squared distribution given by $r^2 = x^2 + y^2$. What is clear in both figures are the dips below the otherwise mostly flat distributions in both the data and the MC. These dips correspond to the walls of the acrylic target vessel through which electrons are not capable of passing. The dip does not go all the way down to zero because of the event position reconstruction explained in Section 3.2.2. The reconstruction resolution is such that if a point like source is considered, the events will be reconstructed with a Gaussian distribution in each space coordinate. This means that events in the GC can be reconstructed inside the NT and vice versa, giving rise to the dips observed.

The location of the dips can be used to our advantage to overcome any bias in the position reconstruction. Instead of using the NT vessel coordinates from the detector blueprints to select events within the FV which is also the NT, a cut can be applied to the location of the dip minima instead. By fitting the data points in Figures 7.6a and 7.6b with inverted Gaussian functions the NT boundary is found at $z_{\text{NT}}^{\text{bot}} = -1261$ mm, $z_{\text{NT}}^{\text{top}} = 1209$ mm and $r_{\text{NT}}^2 = 1.208 \times 10^6$ mm. The real NT acrylic vessel can be found at $z_{\text{real,NT}}^{\text{bot}} = -1229$ mm,

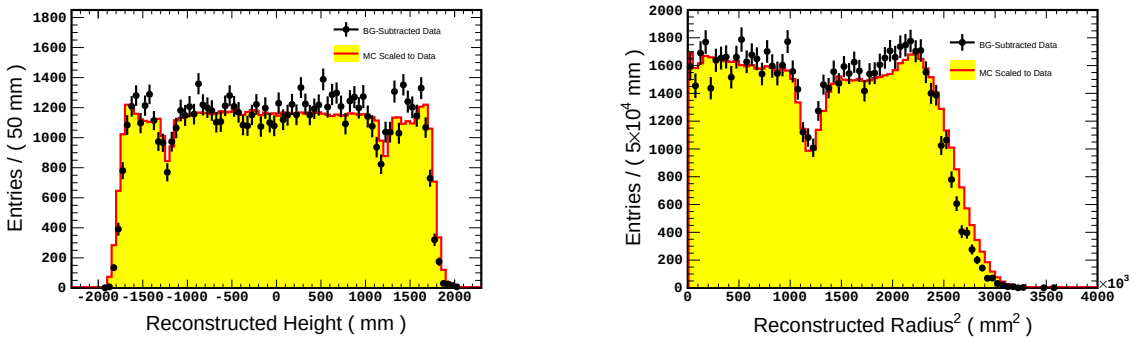

(a) Reconstructed height distribution

(b) Reconstructed radius squared distribution

Figure 7.6 The black data points represent the BG subtracted distribution of cosmogenic candidates dominated by ^{12}B. The histogram with a red line and filled in yellow represents MC events following the same selection criteria as the data (except any muon correlations) scaled to the number of events in the data.

$z^{\text{top}}_{\text{real,NT}} = 1229\,\text{mm}$ and $r^2_{\text{real,NT}} = 1.323 \times 10^6\,\text{mm}$ showing some tendency to reconstruct events closer to the detector center in the (x,y) plane. The MC is used to evaluate the uncertainty of the chosen spatial cuts and if there is any remaining reconstruction bias between the GC and NT volumes. The number of events generated in the NT but reconstructed in the GC and the number of events created in the GC but reconstructed in the NT are measured. As a function of the total number of events generated in the NT, a percentage of $2.46 \pm 0.37\,\%$ was found corresponding to a net number of events generated in the GC but reconstructed in the NT. This correction is applied to the yield and production rate calculations in the following sections.

7.6 ^{12}B Yields and Production Rates

The signal to BG ratio of cosmogenic radioisotope production is related to E^{μ}_{vis} for two reasons. Firstly, as shown in Section 4.5.2.3 the muon visible energy corresponds to its flight path though the ID, where muons with larger E^{μ}_{vis} are more likely to pass closer to the ID center and therefore the FV. Secondly, muons with larger E^{μ}_{vis} are also correlated to showering muons which have a larger $\mathrm{d}E/\mathrm{d}X$ than minimum ionising muons and are more likely to produce cosmogenic radioisotopes. To decrease the uncertainty on the final yield and production rate calculations, ΔT distributions for various minimum muon energies are fitted with Equation 7.12 using the dominant cosmogenic radioisotopes ^{12}B, ^{9}Li and ^{8}Li between $\Delta T \in [0, 15]\,\text{s}$. The minimum muon energy is defined so that only the ΔT distribution of cosmogenic isotopes and muons with E^{μ}_{vis} greater than the specified minimum

are used. The fit returns the number of each cosmogenic radioisotope produced by the muons used in the selection and their uncertainty. A good way of differentiating which is the best minimum muon energy to use in the fit would be to find the smallest $\delta S/S$, where the signal S in this chapter is the number of ^{12}B events from the fit. This was found for a minimum muon energy of 540 MeV. A fit is performed to the ΔT and E_{vis} distribution using muons with $E^{\mu}_{\text{vis}} > 540\,\text{MeV}$ and a correction is made later to compensate for ^{12}B produced by muons with $20\,\text{MeV} < E^{\mu}_{\text{vis}} < 540\,\text{MeV}$.

The energy spectrum of the cosmogenic candidates is created as a cross check for observational purposes. It is created using the same data sample used in the fit but utilises different bin sizes and includes a BG subtraction. Figure 7.8b shows the BG subtracted visible energy spectrum of the cosmogenic events as black points. It is created with an on-time window where $\Delta T \in [2,52]$ ms and subtracting the off-time spectrum which is the average of two windows between $\Delta T \in [502,602]$ ms. The cosmogenic predicted spectra displayed in the same figure are normalised from the fit to the number of events expected in the ΔT region of the spectrum $\Delta T \in [2,52]$ ms.

The amount of ^{12}B is evaluated by performing a fit over the time period $\Delta T \in [2,252]$ ms and energy range $E_{\text{vis}} \in [4,17]$ MeV. In this time and energy region the expected cosmogenic radioisotopes are ^{12}B, ^{12}N, ^{9}Li and ^{8}He where the latter three are treated as contaminants. This means that their yields and production rates are not evaluated using the fit results, they are simply used to accurately estimate the amount of ^{12}B. The yield and production rate estimates for ^{9}Li and ^{8}He are explained in Chapter 6 and ^{12}N in Section 7.7. There are other longer lived radioisotopes expected in this range such as ^{8}B and ^{8}Li, however their lifetimes are long enough that their distributions are expected to be flat over this ΔT range and are absorbed in μ_i^{BG}. For more information about ^{8}B and ^{8}Li see Chapter 8. The cosmogenic

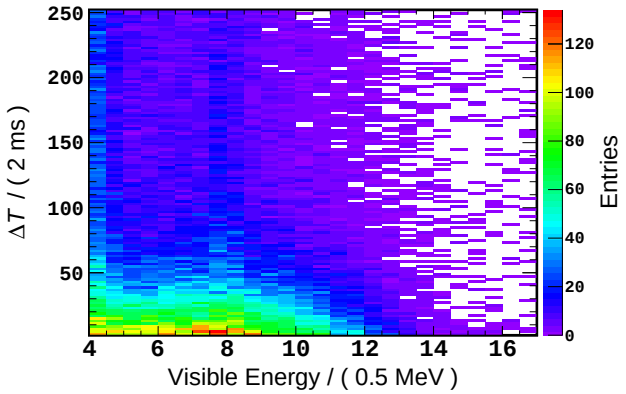

Figure 7.7 The two dimensional histogram of ΔT against visible energy used in the fit to estimate the number of ^{12}B and ^{12}N events.

spectra $S^c(E_{\text{vis}})$ used to evaluate the expected values μ_i are explained in Section 7.3 and the BG spectrum is created by taking the average of 25 windows between $\Delta T \in [500, 550]$. The best fit returned $N^{^{12}\text{B}} = 26917 \pm 275$, $N^{^{12}\text{N}} = 710 \pm 100$, $N^{^{9}\text{Li}} = 5133 \pm 575$ and $N^{^{8}\text{He}} = 465 \pm 580$ at $-2\ln\lambda/d.o.f = 2801/2596$. Figure 7.8a shows the ΔT distribution used for the fit where the data, represented by black points, is the sum of the events along the energy axis. Also shown are the contributions from ^{12}B (violet), ^{12}N (green), ^{9}Li (blue), ^{8}He (black) and the BG (light green). Their total is shown as a red line. The energy spectrum is

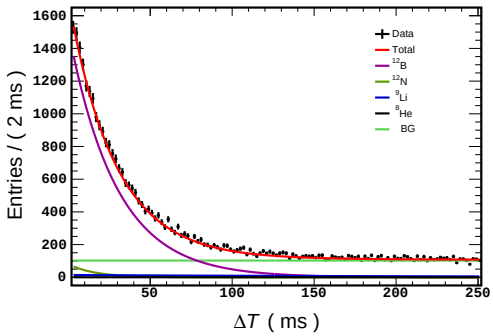

(a) The ΔT distribution from the data (black points). The cosmogenic radioisotope contributions are shown by coloured lines whose sum is displayed in red.

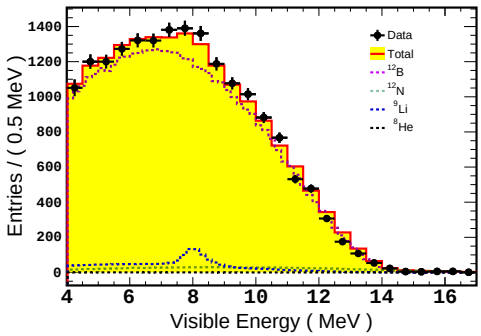

(b) The BG subtracted visible energy spectrum from data (black points) and the cosmogenic radioisotope contributions.

Figure 7.8 The best fit results and the corresponding components of the cosmogenic radioisotopes ^{12}B (violet), ^{12}N (green), ^{9}Li (blue) and ^{8}He (black) and their sum represented by a red line. The components in the ΔT distribution are represented by solid lines whilst the visible energy spectrum makes use of dashed lines

shown in Figure 7.8b where the data has already been explained. The components of ^{12}B (violet), ^{12}N (green), ^{9}Li (blue), ^{8}He (black) are represented using dotted lines and their sum is represented by a red line.

To evaluate the efficiency of selecting muons with $E^{\mu}_{\text{vis}} > 540\,\text{MeV}$, the number of ^{12}B events is measured using a fit to the ΔT distribution only for various minimum muon energies. Only the dominant cosmogenic radioisotopes expected ^{12}B, ^{9}Li and ^{8}He are included in the fit function defined by Equation 7.12. A plot of the number of ^{12}B events from the fit as a function of the minimum muon energy can be normalised to give the efficiency of each minimum muon energy cut. A separate correction needs to be made to the efficiency for each minimum muon energy due to the muon dead time. The muon dead time is applied to cosmogenic candidates if they are within 2 ms of a vetoing muon. However, a sub-sample of the veto muons are used to tag the cosmogenic events and although they also induce a dead time, this is corrected in the fit to the ΔT distribution. If we call the rate of all

veto muons R_μ^{veto} and the rate of muons that are used to tag cosmogenic events R_μ^{tag} then

$$R_\mu^{\text{veto}} = R_\mu^{\text{tag}} + R_\mu^{\text{eff}} \tag{7.13}$$

where R_μ^{eff} is the effective rate of veto muons. The probability that a cosmogenic candidate is vetoed is given by $P = R_\mu^{\text{eff}} \cdot 0.002$ in the limit where the induced dead time 0.002 s is small compared to the rate. The number of ^{12}B events is corrected using the probability of vetoing a cosmogenic candidate for each minimum muon energy. The muon dead time corrected number of ^{12}B events is represented by black points in Figure 7.9 and has been normalised to the result at $E_{\text{vis}}^{\mu} > 20\,\text{MeV}$. The efficiency of using a minimum muon energy of 540 MeV is 50.4 %. The same figure also shows the normalised ^{12}N number of events where in this

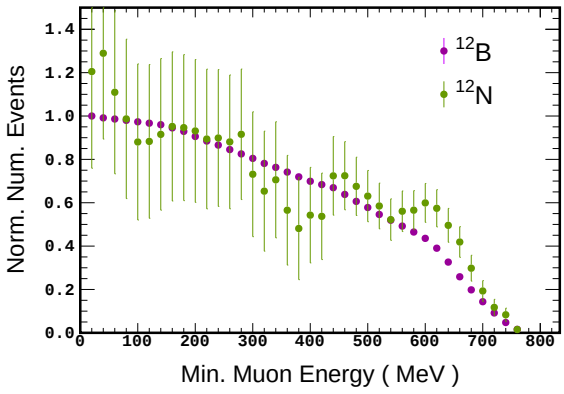

Figure 7.9 The efficiency as a function of minimum muon energy for ^{12}B (violet) and ^{12}N (green). They are estimated using fits to the ΔT distribution of cosmogenic candidates satisfying $E_{\text{vis}} \in [4, 19]\,\text{MeV}$ and $E_{\text{vis}} \in [14, 19]\,\text{MeV}$ for ^{12}B and ^{12}N respectively.

case only the ΔT distribution is used for cosmogenic candidates between $E_{\text{vis}} \in [14, 19]\,\text{MeV}$. Including the spatial reconstruction correction, minimum muon energy efficiency and using Equations 5.17 and 5.16 gives $Y(^{12}\text{B}) = 2.02 \pm 0.02 \times 10^{-6}\,\mu^{-1}\,\text{g}^{-1}\,\text{cm}^2$ and $R(^{12}\text{B}) = 12540 \pm 136\,\text{kton}^{-1}\,\text{day}^{-1}$. When calculating the yields and production rates, the total run time is used instead of the live time as corrections due to the dead time have already been made separately.

7.7 ^{12}N Yields and Production Rates

A pure sample of ^{12}N is expected for $E_{\text{vis}} \in [14, 19]\,\text{MeV}$. In this energy region the number of events are small, so instead of using a combined E_{vis} and ΔT fit, only the ΔT distribution

is fitted using Equation 7.12. The generated spectra are used to estimate the efficiency of the visible energy cuts.
The fit in Section 7.6 returned a non-zero number of ^{12}N events. The visible energy spectrum and ΔT distribution using a minimum muon energy $E^{\mu}_{\text{vis}} > 540\,\text{MeV}$ are shown in Figure 7.10 for observation purposes only. It shows the BG subtracted visible energy spectrum where the data is represented by black points. The on-time window is from $\Delta T \in [2,52]\,\text{ms}$ and the BG is the average of two windows between $\Delta T \in [502,602]\,\text{ms}$. The generated ^{12}N spectrum represented by a red line is normalised using a fit to the ΔT distribution shown in the inset. The fit only includes ^{12}N and is performed over $\Delta T \in [2,502]\,\text{ms}$.
The yields and production rates are calculated using a ΔT fit to all muons with $E^{\mu}_{\text{vis}} > 20\,\text{MeV}$, using the same energy regions and time periods just mentioned. The fit returns $N^{^{12}\text{N}} = 141.6 \pm 56.1$ events. The energy cut efficiency is $\varepsilon(^{12}\text{N}) = 8.6 \pm 0.56\,\%$ where the uncertainty is from the energy scale. Correcting $N^{^{12}\text{N}}$ for the energy cut efficiency, the position reconstruction bias and using Equations 5.17 and 5.16 gives $Y(^{12}\text{N}) = 6.62 \pm 2.6 \times 10^{-8}\,\mu^{-1}\,\text{g}^{-1}\,\text{cm}^2$ and $R(^{12}\text{N}) = 412 \pm 163\,\text{kton}^{-1}\,\text{day}^{-1}$.

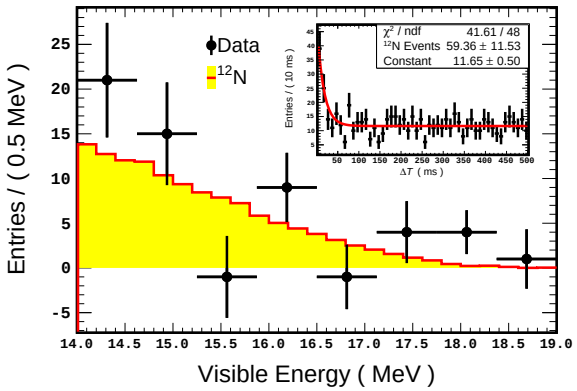

Figure 7.10 The BG subtracted ^{12}N visible energy spectrum (black points) in the region $E_{\text{vis}} \in [14,19]\,\text{MeV}$ for a minimum muon energy of 540 MeV. The generated spectrum (red line) is normalised using a fit to the ΔT distribution shown in the inset.

7.8 Comparison to Borexino and KamLAND

The ^{12}B and ^{12}N yields estimated for the DC far detector can be compared to those measured at KamLAND and Borexino in a similar fashion to Figure 6.13 for ^{9}Li and ^{8}He. The results are shown in Figure 7.11, where the violet points represent ^{12}B, the green points represent ^{12}N, the circles represent DC measurements at the far detector, diamonds represent

KamLAND and crosses represent Borexino. The Borexino and KamLAND measurements are carbon density corrected to DC as explained in Section 6.4.3.1 and the Borexino measurement of ^{12}N is an upper limit of 3σ. The three measurements of the ^{12}B yield can be

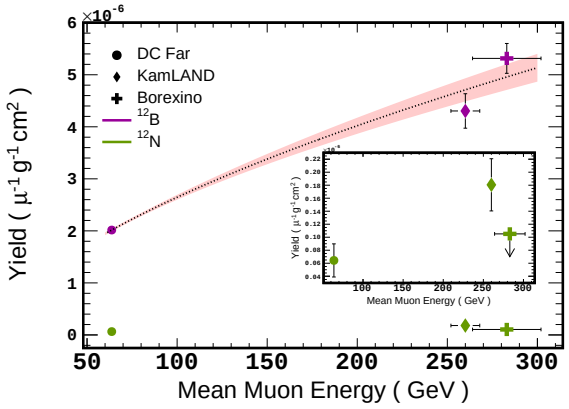

Figure 7.11 The carbon density corrected yields from DC far (circle), KamLAND (diamond) and Borexino (cross) for ^{12}B (violet) and ^{12}N (green). A magnification of the ^{12}N data points is shown in the inset and the Borexino measurement of ^{12}N is an upper limit of 3σ. A fit to the ^{12}B data points measures the power law exponent $\alpha = 0.60 \pm 0.03$

fitted with Equation 5.19 for the power law exponent to give $\alpha = 0.60 \pm 0.03$. The best fit is represented on the plot by a black dashed line and the pink error band represents the uncertainty on the fit.

7.9 Conclusion

The yields and production rates of ^{12}B and ^{12}N have been measured in the DC far detector. For ^{12}B they are $Y(^{12}\mathrm{B}) = 2.02 \pm 0.02 \times 10^{-6}\,\mu^{-1}\,\mathrm{g}^{-1}\,\mathrm{cm}^2$ and $R(^{12}\mathrm{B}) = 12540 \pm 136\,\mathrm{kton}^{-1}\,\mathrm{day}^{-1}$. For ^{12}N they are $Y(^{12}\mathrm{N}) = 6.62 \pm 2.6 \times 10^{-8}\,\mu^{-1}\,\mathrm{g}^{-1}\,\mathrm{cm}^2$ and $R(^{12}\mathrm{N}) = 412 \pm 163\,\mathrm{kton}^{-1}\,\mathrm{day}^{-1}$. The yields have been compared to the measurements by Borexino and KamLAND and have allowed a measurement of the power law exponent $\alpha = 0.60 \pm 0.03$ for the first time using ^{12}B. The relation $Y \propto \langle E_\mu \rangle^\alpha$ can be used to extrapolate the ^{12}B yield at other detector sites. Knowledge of the α parameter could give a better understanding into the ^{12}B production mechanisms as a function of mean muon energy, or depth.

Chapter 8

^{8}Li and ^{8}B

8.1 Introduction

This Chapter explains the measurement of the cosmogenic radioisotopes ^{8}Li ($Q_{\beta^-} = 13\,\text{MeV}$ and $\tau = 1.21\,\text{s}$) and ^{8}B ($Q_{EC} = 14.6\,\text{MeV}$ and $\tau = 1.11\,\text{s}$). Measurements of ^{8}Li and ^{8}B have been made by KamLAND, Borexino and T. Hagner et al. [82] in liquid scintillators. This suggests that their production also occurs in the DC far detector although the shallow overburden and their long lifetimes may drown them out to background events. The primary processes behind their production are ^{12}C$(n, p\alpha)^{8}$Li and ^{12}C$(\pi^+, {}^{2}\text{H}{}^{2}\text{H})^{8}$B [72]. Figure 8.1 shows the decay scheme for ^{8}Li on the left and ^{8}B on the right.

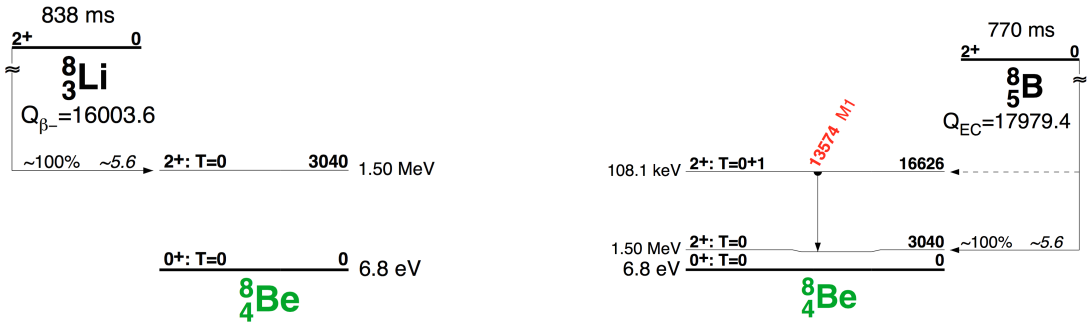

(a) ^{8}Li. **(b)** ^{8}B.

Figure 8.1 The decay schemes for ^{8}Li and ^{8}B. Source [84]

8.2 Real Radial Distribution

The real radial distribution has been simulated using FLUKA as described in Section 4.5.2.1 and the results are shown in Figure 8.2. The ^{8}Li distribution is represented by pale blue points and the ^{8}B by grey points. A fit to the distributions using Equation 4.5 gives $\lambda_{1,^{8}\mathrm{Li}} = 20 \pm 1$ mm, $\lambda_{2,^{8}\mathrm{Li}} = 734 \pm 8$ mm, $\lambda_{1,^{8}\mathrm{B}} = 21 \pm 2$ mm and $\lambda_{2,^{8}\mathrm{B}} = 530 \pm 10$ mm. The

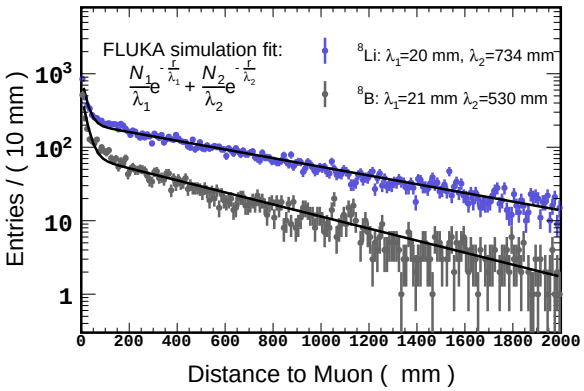

Figure 8.2 FLUKA simulations for the production of ^{8}Li and ^{8}B as a function of the distance from the parent muon. A fit of the function shown in the plot gives $\lambda_{1,^{8}\mathrm{Li}} = 20 \pm 1$ mm, $\lambda_{2,^{8}\mathrm{Li}} = 734 \pm 8$ mm, $\lambda_{1,^{8}\mathrm{B}} = 21 \pm 2$ mm and $\lambda_{2,^{8}\mathrm{B}} = 530 \pm 110$ mm. Data from [74]

parameters corresponding to the number of events give $N_{1,^{8}\mathrm{Li}} = 1418 \pm 65$ events, $N_{2,^{8}\mathrm{Li}} = 1551 \pm 136$ events, $N_{2,^{8}\mathrm{B}} = 980 \pm 56$ events and $N_{2,^{8}\mathrm{B}} = 3994 \pm 79$ events.

8.3 Spectrum Generation

The ^{8}Li and ^{8}B spectra were generated as described in Section 7.3.1. The decays of these radioisotopes hadn't been generated in DC before so their decay schemes were taken from [84] and used as input to the generator. The corresponding spectra which include the detector response can be seen in Figure 8.3 where ^{8}Li is shown by the pale blue line and ^{8}B by the grey line.

8.4 Event Selection

The preliminary selection follows the same criteria as described in Table 7.1. As ^{8}Li and ^{8}B have a much longer lifetime compared to ^{12}B, ^{12}N, ^{9}Li and ^{8}He, cosmogenic candidates within 0.6 s of a tagging muon are not used in the fit as they contain the shorter lived

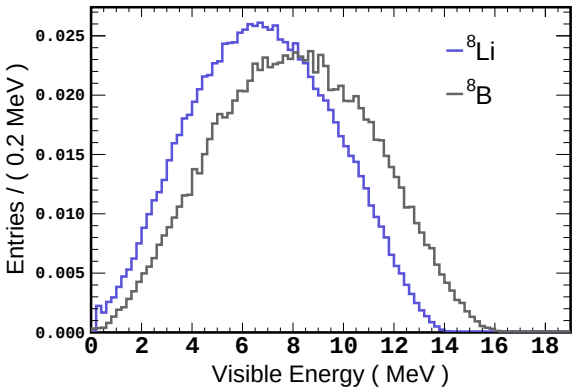

Figure 8.3 The generated spectra for ^{8}Li (pale blue) and ^{8}B (grey)

isotopes ^{12}B, ^{12}N, ^{9}Li and ^{8}He. In a similar manner to Section 7.6 a plot of $\delta S/S$ against the minimum muon energy showed a minimum for muons with $E^{\mu}_{\text{vis}} > 610\,\text{MeV}$. The signal S in this case is the number of ^{8}Li events from a fit to the ΔT distribution only for $\Delta T \in [0.6, 15]\,\text{s}$ and $E_{\text{vis}} \in [5, 19]\,\text{MeV}$.
The spectrum from data represented by black points in Figure 8.4a is created by taking the on-time window $\Delta T \in [0.6, 4.6]\,\text{s}$ and subtracting the BG spectrum which is the average of two spectra between $\Delta T \in [6.6, 14.6]\,\text{s}$.

8.5 Yields and Production Rates

The fit uses both ΔT and visible energy information using the BML approach explained in Section 7.4 and the generated spectra for ^{8}Li and ^{8}B from Section 8.3. The fit is performed over $\Delta T \in [0.6, 10]\,\text{s}$ using a bin width of 0.05 ms and the expected BG spectrum is created by taking the average between $\Delta T \in [10, 11]\,\text{s}$. The visible energy range used is $E_{\text{vis}} \in [5, 18]\,\text{MeV}$ with a bin width of 1 MeV. The generated spectra over the whole visible energy range $E_{\text{vis}} \in [0, 18]\,\text{MeV}$ are normalised to unity before being used in the fit. This means that the number of events returned by the fit covers the whole visible energy spectrum and ΔT distribution. A small binning is used in ΔT to help differentiate between ^{8}Li and ^{8}B as their lifetimes are very similar and the signal to BG ratio is very small. The results of the fit are $N^{^8\text{Li}} = 8734 \pm 837$ events and $N^{^8\text{B}} = 1994 \pm 659$ events at a minimum of $-2\ln\lambda/d.o.f = 2817/2598$. The correlation between the two parameters is $\rho = -0.88$.
The results are shown in Figure 8.4. Figure 8.4a shows the ΔT distribution of events used in the fit where the data is represented by the black points, the ^{8}Li content by the pale blue line, the ^{8}B content by the grey line, the BG by the green line and their sum is shown by the red

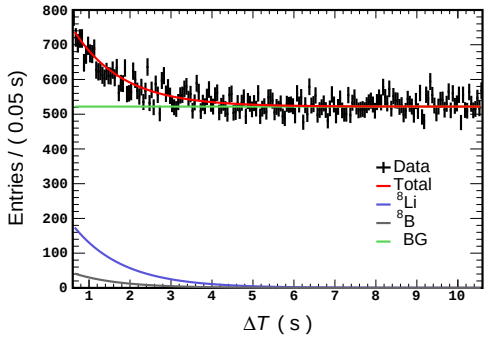

(a) The ΔT distribution of the data displayed as black points along with the cosmogenic radioisotope contributions. Their sum is displayed by the red line.

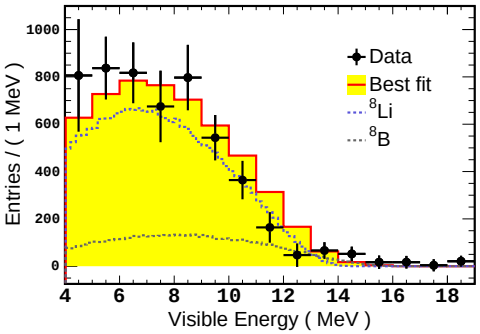

(b) The BG subtracted visible energy spectrum of data (black points) and the cosmogenic radioisotope contributions.

Figure 8.4 The best fit results with the corresponding components of the cosmogenic radioisotopes ^{8}Li (pale blue), ^{8}B (grey) and their sum by a red line. The components in the ΔT distribution are drawn using whole lines whilst the visible energy spectrum are drawn using dashed lines.

line. They are normalised to the expected number of events in the energy range used for the fit $E_{\text{vis}} \in [5, 18]$ MeV. Figure 8.4b shows the BG subtracted data spectrum also represented by black points and the ^{8}Li and ^{8}B content using the same colours as the ΔT distribution where the best fit results have been normalised to the number of events expected in the on-time window $\Delta T \in [0.6, 4.6]$ s.

The efficiency corresponding to a minimum muon energy of 610 MeV is estimated using the ^{12}B normalised shape in Figure 7.9 as the cosmogenic radioisotopes are expected to follow the same trend. For 610 MeV the efficiency is 41.3 %. Correcting $N^{^{8}\text{Li}}$ and $N^{^{8}\text{B}}$ for the minimum muon energy efficiency, position reconstruction bias and using Equations 5.17 and 5.16 gives the yields $Y(^{8}\text{Li}) = 8.23 \pm 0.79 \times 10^{-7}\,\mu^{-1}\,\text{g}^{-1}\,\text{cm}^{2}$ and $Y(^{8}\text{B}) = 1.88 \pm 0.62 \times 10^{-7}\,\mu^{-1}\,\text{g}^{-1}\,\text{cm}^{2}$ and the production rates $R(^{8}\text{Li}) = 5117 \pm 491\,\text{kton}^{-1}\,\text{day}^{-1}$ and $R(^{8}\text{B}) = 1168 \pm 386\,\text{kton}^{-1}\,\text{day}^{-1}$.

8.6 Comparison to KamLAND and Borexino

The yields can be compared to the carbon density corrected measurements from KamLAND and Borexino. They are shown in Figure 8.5 along with the measurements from the previous section at the DC far detector. The DC far detector measurements are shown by circles,

KamLAND by diamonds and Borexino by crosses. The separate measurements for ^{8}Li are coloured pale blue and measurements of ^{8}B are coloured grey.

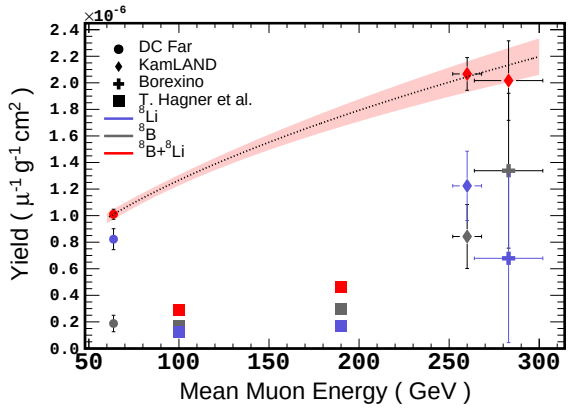

Figure 8.5 The carbon density corrected yields from DC far (circle), KamLAND (diamond), Borexino (cross) and T. Hagner et al. (squares) for ^{8}Li (pale blue) and ^{8}B (grey). Their sum is represented by red points assuming a correlation of $\rho = -0.88$.

The plot shows an incongruity for measurements between different experiments. The Hagner measurements are lower than expected, as was already shown in Section 6.4.3.2 for their $^9\text{Li} + {}^8\text{He}$ measurement. Interestingly, from the five experimental measurements, only two experiments, DC and KamLAND report larger yields of ^{8}Li than ^{8}B. This is difficult to attribute to different production rates at different depths as the discrepancy is across the $\langle E_\mu \rangle$ range. This suggests that there is an inherent difficulty in differentiating between the two radioisotopes and a better approach would be to combine their yields. The combined ^{8}Li and ^{8}B yields are represented by red points in Figure 8.5 where the uncertainties have been combined assuming a correlation of $\rho = -0.88$. A fit to the three points gives $\alpha = 0.5 \pm 0.05$.

T. Hagner et al. made two measurements each for ^{8}Li and ^{8}B of the cross section by using two muon beams with energies 100 GeV and 190 GeV. The yields are calculated from the measured cross sections using Equation 5.18. The correction factor β_α compensating for the differential muon spectrum has been re-evaluated using the α measurement to the total ^{8}Li+^{8}B yields. A muon beam of energy 100 GeV corresponds to a depth of 625 m.w.e and $\beta_\alpha^{100\,\text{GeV}} = 0.822 \pm^{+0.003}_{-0.001}$. A muon beam of energy 190 GeV corresponds to a depth of 1475 m.w.e and $\beta_\alpha^{190\,\text{GeV}} = 0.826 \pm^{+0.003}_{-0.001}$. The uncertainties are from the the error on the α measurement. Their measurements can be seen in the plot as squares. Using two measurements of each radioisotope, T. Hagner et al also determined the power law exponent for each. For ^{8}Li and ^{8}B they quote $\alpha = 0.5 \pm 0.71$ and $\alpha = 0.84 \pm 0.45$ respectively with an admittedly large uncertainty. Although this section and Section 6.4.3.2 show their yields

to be significantly smaller than the measurements made by Borexino, KamLAND and this work, if this bias is the same for both their measurements, the α determination should still be valid and in fact their uncertainties cover the α measurement in this Chapter.

8.7 Conclusion

The generated spectra of ^{8}B and ^{8}Li were used in a fit using both visible energy and time information to estimate their content in the data sample. Correcting for efficiencies the yields $Y(^{8}\mathrm{Li}) = 8.23 \pm 0.79 \times 10^{-7}\,\mu^{-1}\,\mathrm{g}^{-1}\,\mathrm{cm}^{2}$ and $Y(^{8}\mathrm{B}) = 1.88 \pm 0.62 \times 10^{-7}\,\mu^{-1}\,\mathrm{g}^{-1}\,\mathrm{cm}^{2}$ and production rates $R(^{8}\mathrm{Li}) = 5117 \pm 491\,\mathrm{kton}^{-1}\,\mathrm{day}^{-1}$ and $R(^{8}\mathrm{B}) = 1168 \pm 386\,\mathrm{kton}^{-1}\,\mathrm{day}^{-1}$ are calculated. The individual yield measurements and their comparisons to Borexino and KamLAND found incongruous results. Instead of fitting them individually for the power law exponent, they were combined and a fit to all three gives $\alpha = 0.5 \pm 0.05$. The uncertainty from the T. Hagner et al. measurements of α for ^{8}Li and ^{8}B covers the combined ^{8}Li+^{8}B α determination in this Chapter.

Chapter 9

Summary and Outlook

The Double Chooz experiment is one of three reactor neutrino experiments whose principle aim is the measurement of the θ_{13} neutrino mixing angle. Although Double Chooz was the first experiment to show a hint of disappearance in late 2011 [29], Daya Bay was the first to rule out the no-oscillation hypothesis at 5σ in 2012 [97]. Since then Daya Bay, RENO and Double Chooz have published improved measurements of $\sin^2(2\theta_{13})$ and it is now the best measured of the three mixing angles.

This thesis reported the latest Double Chooz results with measurements of the mixing angle using both the Gd $\sin^2(2\theta_{13}) = 0.090^{+0.032}_{-0.029}$ and H $\sin^2(2\theta_{13}) = 0.098^{+0.038}_{-0.039}$ channel. The H-channel used novel techniques such as an artificial neural network and pulse shape analysis to reduce the background significantly, resulting in a signal to background improvement of a factor of ten compared to the previous publication [45]. An important element of the $\sin^2(2\theta_{13})$ measurement was an accurate estimate of the backgrounds contaminating the IBD sample. The total background contamination was $B = 6.83^{+0.59}_{-0.36}\,\text{day}^{-1}$ where the β-n background contributes $\mathscr{R}^{\text{fit}}_{\beta\text{n}} = 0.95^{+0.57}_{-0.33}\,\text{day}^{-1}$. Although the β-n background doesn't dominate the total background rate, it does the uncertainty. The prevalent contribution to the uncertainty is purely statistical, where the large muon rate limits the precision of the β-n measurement. This has been reduced using a better understanding of the lateral distance profile of β-n production from the parent muon. Using this knowledge the efficiency of the distance to the parent muon could be used to reduce the number of un-correlated muons and improve the β-n measurement. The measurement before $\mathscr{R}^{\text{tot}}_{\beta\text{n}} = 2.99 \pm 1.16\,\text{day}^{-1}$ and after $\mathscr{R}^{\text{tot}}_{\beta\text{n}} = 2.76^{+0.49}_{-0.45}\,\text{day}^{-1}$ shows that the relative uncertainty has roughly halved. The final rate after subtracting the events removed by the $\mathscr{L}_{Li}$ veto is $\mathscr{R}^{\text{fit}}_{\beta\text{n}} = 0.95^{+0.57}_{-0.33}$. This was the final value used as input to the $\sin^2(2\theta_{13})$ fit in the H-channel [46].

The β-n emitters corresponding to some decay chains of ^{9}Li and ^{8}He are not the only cosmogenic radioisotopes produced in the Double Chooz detector. Cosmic muons which pass through the detector interact with the nuclei present to create many more. The dominant interactions take place with ^{12}C atoms present in the organic liquid scintillator. KamLAND and Borexino have already published cosmogenic yield measurements and the shallow depth of the Double Chooz detector allows a unique opportunity to understand their production rate as a function of depth or mean muon energy. The yield measurements for ^{12}B, ^{12}N, ^{9}Li, ^{8}He, ^{8}B and ^{8}Li at the Double Chooz far detector are summarised in Table 9.1.

Table 9.1 A summary of the yield measurements at the Double Chooz far detector along with the corresponding measurements from KamLAND [72] and Borexino [83]. Some of the Borexino measurements represent the 3σ confidence limit. The combination of ^{8}Li+^{8}B assumes a correlation of $\rho = -0.88$.

	Yield ($10^{-7}\,\mu^{-1}\,\mathrm{g}^{-1}\,\mathrm{cm}^{2}$)		
	This work	KamLAND	Borexino
^{12}B	20.2 ± 0.2	42.9 ± 3.3	56 ± 3
^{12}N	0.7 ± 0.3	1.8 ± 0.4	< 1.1
^{9}Li	1.0 ± 0.2	2.2 ± 0.2	2.9 ± 0.3
^{8}He	0.1 ± 0.1	0.7 ± 0.4	< 1.5
^{8}Li	8.2 ± 0.8	12.2 ± 2.6	7 ± 7
^{8}B	1.9 ± 0.6	8.4 ± 2.4	14 ± 6
^{8}Li+^{8}B	10.1 ± 0.4	20.7 ± 1.23	20.2 ± 2.99

The three yield measurements of each radioisotope are fitted with $Y = Y_0 \langle E_\mu \rangle^{\alpha}$ to give the first multi-experiment, cross-continent determination of the power law exponent α using liquid scintillator detectors. The mean muon energy at each site is representative of the detector depth, so if the depth or mean muon energy is known at some site, the α parameter allows an extrapolation of the cosmogenic radioisotope production to it. They are summarised in Table 9.2 along with the measurements from T. Hagner et al. and simulations using FLUKA by KamLAND where available. They allow the extrapolation of cosmogenic radioisotope production to other depths if the mean muon energy is known. This is especially important for ^{9}Li and ^{8}He as they are the dominant backgrounds of IBD signals which are imitated by their β-n decay signature. The measurements themselves differ from the simulations suggesting simulations aren't yet capable of modelling their production rates as a function of depth. The α parameters determined in this work could help to better understand the cosmogenic production processes and muon radiative energy loss as a

function of the mean muon energy. The near detector is even shallower than the DC far detector and once the data is available for analysis, measurements of the yields will add another point to the power law exponent fit reducing the uncertainty. Although a shallow

Table 9.2 A summary of the power law exponent α for each isotope from a fit to the three yield measurements in Table 9.1. Where available the measurements from Hagner et al. [82] using two muon beam energies of 100 GeV and 190 GeV. The last column lists the results of a FLUKA simulation by the KamLAND collaboration where the uncertainty is statistical [72].

	α		
	This work	Hagner et al.	FLUKA sim. (KamLAND)
^{12}B	0.60 ± 0.03	-	0.825 ± 0.007
^{12}N	-	-	0.921 ± 0.045
^{9}Li	0.64 ± 0.15	-	0.801 ± 0.026
^{8}He	-	-	0.926 ± 0.078
^{8}Li	-	0.50 ± 0.71	0.821 ± 0.010
^{8}B	-	0.84 ± 0.45	0.804 ± 0.019
^{8}Li+^{8}B	0.50 ± 0.05	-	-

depth detector has disadvantages due to the higher cosmic muon induced background, in the case of Double Chooz it has proven useful for the determination of α.
The list of cosmogenic radioisotopes measured in Double Chooz is not yet complete, and further work would be needed to measure ^{9}C, ^{10}C, ^{11}C, ^{11}Be and ^{6}He. Most of these radioisotopes have long lifetimes and low Q values, so the combination of a high muon rate at the DC depth and large backgrounds in this low energy region makes it challenging to measure their yields. Having said that, there are a number of techniques for reducing the background, such as using distance to the muon and only selecting muons which deposit large amounts of energy in detector. This would be the next step to make the picture complete.

References

Bibliography items with the label DocDB are slides and technical reports internal to the Double Chooz collaboration. They can be found at the following link:
www.dchooz.org/DocDB/cgi-bin/private/DocumentDatabase
They will be made public at the end of the Double Chooz experiment.

[1] W. Pauli. Dear radioactive ladies and gentlemen. *Phys. Today*, 31N9(27), 1978.

[2] S. Bilenky. *Introduction to the Physics of Massive and Mixed Neutrinos*. Lect. Notes Phys 817. Springer-Verlag Berlin Heidelberg, 2010.

[3] B. Pontecorvo. Inverse beta decay. *Camb. Monogr. Part. Phys. Nucl. Cosmol.*, 1:25–31, 1991.

[4] C. L. Cowan, F. Reines, F. B. Harrison, H. W. Kruse, and A. D. McGuire. Detection of the free neutrino: a confirmation. *Science*, 124(3212):103–104, 1956.

[5] C. S. Wu, E. Ambler, R. W. Hayward, D. D. Hoppes, and R. P. Hudson. Experimental test of parity conservation in beta decay. *Phys. Rev.*, 105:1413–1415, Feb 1957.

[6] M. Goldhaber, L. Grodzins, and A. W. Sunyar. Helicity of neutrinos. *Phys. Rev.*, 109:1015–1017, Feb 1958.

[7] G. Danby et al. Observation of high-energy neutrino reactions and the existence of two kinds of neutrinos. *Phys. Rev. Lett.*, 9:36–44, Jul 1962.

[8] Bruce T. Cleveland, Timothy Daily, Jr. Raymond Davis, James R. Distel, Kenneth Lande, C. K. Lee, Paul S. Wildenhain, and Jack Ullman. Measurement of the solar electron neutrino flux with the homestake chlorine detector. *The Astrophysical Journal*, 496(1):505, 1998.

[9] K. S. Hirata et al. Observation of ^{8}B solar neutrinos in the kamiokande-ii detector. *Phys. Rev. Lett.*, 63:16–19, Jul 1989.

[10] W. Hampel et al. GALLEX solar neutrino observations: results for GALLEX IV. *Physics Letters B*, 447(1–2):127 – 133, 1999.

[11] J.N. Abdurashitov et al. Solar neutrino flux measurements by the soviet-american gallium experiment (sage) for half the 22-year solar cycle. *Journal of Experimental and Theoretical Physics*, 95(2):181–193, 2002.

[12] Y. Fukuda et al. Evidence for oscillation of atmospheric neutrinos. *Phys. Rev. Lett.*, 81:1562–1567, Aug 1998.

[13] K. Kodama et al. Observation of tau neutrino interactions. *Physics Letters B*, 504(3):218 – 224, 2001.

[14] Y. Abe et al. Improved measurements of the neutrino mixing angle θ_{13} with the double chooz detector. *Journal of High Energy Physics*, 2014(10), 2014.

[15] F. P. An et al. Improved measurement of electron antineutrino disappearance at daya bay. *Chinese Physics C*, 37(1):011001, 2013.

[16] J. K. Ahn et al. Observation of reactor electron antineutrinos disappearance in the reno experiment. *Phys. Rev. Lett.*, 108:191802, May 2012.

[17] M. H. Ahn et al. Measurement of neutrino oscillation by the K2K experiment. *Phys. Rev. D*, 74:072003, Oct 2006.

[18] P. Adamson et al. Measurement of the neutrino mass splitting and flavor mixing by minos. *Phys. Rev. Lett.*, 106:181801, May 2011.

[19] T. Nakaya. New results from T2K. *Nuclear Physics B - Proceedings Supplements*, 235–236:97 – 104, 2013. The XXV International Conference on Neutrino Physics and Astrophysics.

[20] N. Barros. Final results from SNO. *Nuclear Physics B - Proceedings Supplements*, 237–238:107 – 110, 2013. Proceedings of the Neutrino Oscillation WorkshopProceedings of the Neutrino Oscillation Workshop.

[21] M. Pallavicini et al. Recent results and future development of borexino. *Nuclear Physics B - Proceedings Supplements*, 235–236:55 – 60, 2013. The XXV International Conference on Neutrino Physics and Astrophysics.

[22] K. A. Olive et al. Review of Particle Physics. *Chin. Phys.*, C38:090001, 2014.

[23] Carlo Giunti and Chung W. Kim. *Fundamentals of Neutrino Physics and Astrophysics*. Oxford University Press, 2007.

[24] D. V. Forero, M. Tórtola, and J. W. F. Valle. Neutrino oscillations refitted. *Phys. Rev. D*, 90:093006, Nov 2014.

[25] M. Apollonio et al. Limits on neutrino oscillations from the CHOOZ experiment. *Physics Letters B*, 466(2–4):415 – 430, 1999.

[26] M. Apollonio et al. Search for neutrino oscillations on a long base-line at the chooz nuclear power station. *The European Physical Journal C - Particles and Fields*, 27(3):331–374, 2003.

[27] F. Boehm et al. Final results from the palo verde neutrino oscillation experiment. *Phys. Rev. D*, 64:112001, Nov 2001.

[28] K. Abe et al. Indication of electron neutrino appearance from an accelerator-produced off-axis muon neutrino beam. *Phys. Rev. Lett.*, 107:041801, Jul 2011.

[29] H. de Kerret. First results from the double chooz experiment. LowNu 2011 Conference, November 2011.

[30] Y. Abe et al. Indication of reactor $\overline{\nu}_e$ disappearance in the double chooz experiment. *Phys. Rev. Lett.*, 108:131801, Mar 2012.

[31] A. Cucoanes, P. Novella, A. Cabrera, M. Fallot, A. Onillon, M. Obolensky, and F. Yermia. Reactor neutrino flux uncertainty suppression on multiple detector experiments. *arXiv:1501.00356*, 2015.

[32] Xiangpan Ji. Recent progress from daya bay. EPS HEP 2015 Conference, Vienna, July 2015.

[33] Seon-Hee (Sunny) Seo. New results from reno & future reno-50. EPS HEP 2015 Conference, Vienna, July 2015.

[34] F. Ardellier, I. Barabanov, J.C. Barriere, M. Bauer, Leonid B. Bezrukov, et al. Letter of intent for Double-CHOOZ: A Search for the mixing angle θ_{13}. *hep-ex/0405032*, 2004.

[35] K. Anderson, J.C. Anjos, D. Ayres, J. Beacom, I. Bediaga, et al. White paper report on Using Nuclear Reactors to Search for a value of θ_{13}. *hep-ex/0402041*, 2004.

[36] Y. Abe et al. Reactor $\overline{\nu}_e$ disappearance in the double chooz experiment. *Phys. Rev. D*, 86:052008, Sep 2012.

[37] F Beissel et al. The trigger and timing system of the double chooz experiment. *Journal of Instrumentation*, 8(01):T01003, 2013.

[38] C Aberle, C Buck, B Gramlich, F X Hartmann, M Lindner, S Schönert, U Schwan, S Wagner, and H Watanabe. Large scale gd-beta-diketonate based organic liquid scintillator production for antineutrino detection. *Journal of Instrumentation*, 7(06):P06008, 2012.

[39] International Atomic Energy Agency (IAEA). *Database of Prompt Gamma Rays from Slow Neutron Capture for Elemental Analysis*. STI/PUB/1263 (ISBN:92-0-101306-X), 2007.

[40] E. Calvo, M. Cerrada, C. Fernández-Bedoya, I. Gil-Botella, C. Palomares, I. Rodríguez, F. Toral, and A. Verdugo. Characterization of large-area photomultipliers under low magnetic fields: Design and performance of the magnetic shielding for the double chooz neutrino experiment. *Nuclear Instruments and Methods in Physics Research Section A: Accelerators, Spectrometers, Detectors and Associated Equipment*, 621(1–3):222 – 230, 2010.

[41] D Dietrich, D Greiner, J Jochum, T Lachenmaier, M Röhling, and L F F Stokes. Monte carlo aided design of the inner muon veto detectors for the double chooz experiment. *Journal of Instrumentation*, 7(08):P08012, 2012.

[42] Bernd Reinhold. *Development of a Level-1 Trigger and Timing System for the Double Chooz Neutrino Experiment*. PhD thesis, RWTH Aachen University, 2009.

[43] Y Abe, T Akiri, A Cabrera, B Courty, J V Dawson, L F G Gonzalez, A Hourlier, M Ishitsuka, H de Kerret, D Kryn, P Novella, M Obolensky, S Perasso, A Remoto, and R Roncin. The waveform digitiser of the double chooz experiment: performance and quantisation effects on photomultiplier tube signals. *Journal of Instrumentation*, 8(08):P08015, 2013.

[44] Igore Ostrovskiy. Guide tube irr. Double Chooz Internal Document, DC-doc-887-v1, June 2009.

[45] Y. Abe et al. First measurement of θ_{13} from delayed neutron capture on hydrogen in the Double Chooz experiment. *Physics Letters B*, 723(1–3):66 – 70, 2013.

[46] Abe Y. et al. Measurement of θ_{13} in double chooz using neutron capture on hydrogen with novel background rejection techniques. *Journal of High Energy Physics*, 2016(1):163, Jan 2016.

[47] V.I. Kopeikin, L.A. Mikaelyan, and V.V. Sinev. Reactor as a source of antineutrinos: Thermal fission energy. *Physics of Atomic Nuclei*, 67(10):1892–1899, 2004.

[48] Nea-1845/01 mure, 2009.

[49] O. Meplan et al. Mure: Mcnp utility for reactor evolution-description of the methods, first applications and results. European Nuclear Conference, DECEMBER 2005.

[50] Christopher Jones. *Prediction of the Reactor Antineutrino Flux for the Double Chooz Experiment*. PhD thesis, MIT, September 2012.

[51] Dragon code - polytechnique montréal.

[52] C. L. Jones, A. Bernstein, J. M. Conrad, Z. Djurcic, M. Fallot, L. Giot, G. Keefer, A. Onillon, and L. Winslow. Reactor simulation for antineutrino experiments using dragon and mure. *Phys. Rev. D*, 86:012001, Jul 2012.

[53] P. Vogel and J. F. Beacom. Angular distribution of neutron inverse beta decay, $\overline{\nu}_e + \vec{p} \; e^+ + n$. *Phys. Rev. D*, 60:053003, Jul 1999.

[54] K. Schreckenbach, G. Colvin, W. Gelletly, and F. Von Feilitzsch. Determination of the antineutrino spectrum from 235u thermal neutron fission products up to 9.5 mev. *Physics Letters B*, 160(4–5):325 – 330, 1985.

[55] F. von Feilitzsch, A.A. Hahn, and K. Schreckenbach. Experimental beta-spectra from 239pu and 235u thermal neutron fission products and their correlated antineutrino spectra. *Physics Letters B*, 118(1–3):162 – 166, 1982.

[56] A.A. Hahn, K. Schreckenbach, W. Gelletly, F. von Feilitzsch, G. Colvin, and B. Krusche. Antineutrino spectra from 241pu and 239pu thermal neutron fission products. *Physics Letters B*, 218(3):365 – 368, 1989.

[57] Patrick Huber. Determination of antineutrino spectra from nuclear reactors. *Phys. Rev. C*, 84:024617, Aug 2011.

[58] G. Mention, M. Fechner, Th. Lasserre, Th. A. Mueller, D. Lhuillier, M. Cribier, and A. Letourneau. Reactor antineutrino anomaly. *Phys. Rev. D*, 83:073006, Apr 2011.

[59] N. Haag, A. Gütlein, M. Hofmann, L. Oberauer, W. Potzel, K. Schreckenbach, and F. M. Wagner. Experimental determination of the antineutrino spectrum of the fission products of ^{238}U. *Phys. Rev. Lett.*, 112:122501, Mar 2014.

[60] David Lhuillier. Reactor plots and macros. Double Chooz Internal Document, DC-doc-3373-v1, November 2011.

[61] Anthony Onillon and Muriel Fallot. Reactor plots. Double Chooz Internal Document, DC-doc-3377-v1, November 2011.

[62] Y. Declais et al. Study of reactor antineutrino interaction with proton at bugey nuclear power plant. *Physics Letters B*, 338(2–3):383 – 389, 1994.

[63] S. Agostinelli et al. Geant4—a simulation toolkit. *Nuclear Instruments and Methods in Physics Research Section A: Accelerators, Spectrometers, Detectors and Associated Equipment*, 506(3):250 – 303, 2003.

[64] J. Allison et al. Geant4 developments and applications. *IEEE Transactions on Nuclear Sciences*, 53(1):270–278, February 2006.

[65] Michael Wurm. Technote on recomuhamid. Double Chooz Internal Document, DC-doc-4578-v1, February 2013.

[66] B. Reinhold et al. Dciii energy blessing candidates candidates (esv5). Double Chooz Internal Document, DC-doc-5603-v29, 2014.

[67] Keith Crum. *A Measurement of* $\sin^2 2\theta_{13}$ *with the Double Chooz Experiment*. PhD thesis, The University of Chicago, December 2014.

[68] Emily Conover. *Muon-Induced Backgrounds in the Double Chooz Neutrino Oscillation Experiment*. PhD thesis, University of Chicago, Illinios, June 2014.

[69] Y. Abe et al. Dc-iii analysis tech note. Double Chooz Internal Document, DC-doc-5162-v23, June 2014.

[70] Y. Abe et al. Background-independent measurement of in double chooz. *Physics Letters B*, 735(0):51 – 56, 2014.

[71] P. Adamson et al. Measurement of neutrino and antineutrino oscillations using beam and atmospheric data in minos. *Phys. Rev. Lett.*, 110:251801, Jun 2013.

[72] S. Abe et al. Production of radioactive isotopes through cosmic muon spallation in KamLAND. *Phys. Rev. C*, 81:025807, Feb 2010.

[73] Rene Brun and Fons Rademakers. ROOT — an object oriented data analysis framework. *Nuclear Instruments and Methods in Physics Research Section A: Accelerators, Spectrometers, Detectors and Associated Equipment*, 389(1–2):81 – 86, 1997. New Computing Techniques in Physics Research V.

[74] Michael Wurm. Private email communication. fluka simulation by linldey winslow (2007), March 2014.

[75] A. Ferrari, P.R. Sala, A. Fassò, and J. Ranft. *FLUKA: a multi-particle transport code*. CERN-2005-010, INFN/TC/05_11, SLAC-R-773, 2005.

[76] T.T. Böhlen, F. Cerutti, M.P.W. Chin, A. Fassò, A. Ferrari, P.G. Ortega, A. Mairani, P.R. Sala, G. Smirnov, and V. Vlachoudis. The fluka code: Developments and challenges for high energy and medical applications. *Nuclear Data Sheets*, 120:211–214, 2014.

[77] Y. Abe et al. Direct measurement of backgrounds using reactor-off data in double chooz. *Phys. Rev. D*, 87:011102, Jan 2013.

[78] Thomas K. Gaisser. *Cosmic Rays and Particle Physics*. Cambridge University Press, 1990.

[79] Bernhard Peter Heisinger. *Myonen-Induzierte Produktion von Radionukliden*. PhD thesis, Technische Universität München, June 1998.

[80] J. Beringer et al. Review of particle physics*. *Phys. Rev. D*, 86:010001, Jul 2012.

[81] M Cribier, B Pichard, J Rich, J.P Soirat, M Spiro, Th Stolarczyk, C Tao, D Vignaud, P Anselmann, A Lenzing, C Schlosser, R Wink, and J.K Rowley. The muon induced background in the GALLEX experiment. *Astroparticle Physics*, 6(2):129 – 141, 1997.

[82] T. Hagner, R. von Hentig, B. Heisinger, L. Oberauer, S. Schönert, F. von Feilitzsch, and E. Nolte. Muon-induced production of radioactive isotopes in scintillation detectors. *Astroparticle Physics*, 14(1):33 – 47, 2000.

[83] G. Bellini et al. Cosmogenic backgrounds in borexino at 3800 m water-equivalent depth. *Journal of Cosmology and Astroparticle Physics*, 2013(08):049, 2013.

[84] Richard B. Firestone, Virginia S. Shirley, Coral M. Baglin, S.Y. Frank Chu, and Jean Zipkin. *Table of Isotopes CD-ROM Edition*. John Wiley & Sons Inc., 1996.

[85] Valérian Sibille. Cosmogenic spectra generation. Double Chooz Internal Document, DC-doc-5916-v1, December 2014.

[86] Valérian Sibille. Private email communication. July 2015.

[87] Rachel Carr. *Measurements of Electron Antineutrino Disappearance in the Double Chooz Experiment*. PhD thesis, Columbia University, 2015.

[88] J B Birks. Scintillations from organic crystals: Specific fluorescence and relative response to different radiations. *Proceedings of the Physical Society. Section A*, 64(10):874, 1951.

[89] Wouter Verkerke and David Kirkby. The roofit toolkit for data modeling. *arXiv:physics/0306116*, 2003.

[90] Karim Zbiri. Physics process of cosmogenics 9li and 8he production on muons interactions with carbon target in liquid scintillator. *Nuclear Instruments and Methods in Physics Research Section A: Accelerators, Spectrometers, Detectors and Associated Equipment*, 597(2–3):219 – 221, 2008.

[91] Matt Worchester. Dogs release status. Double Chooz Internal Document, DC-doc-2312-v2, March 2011.

[92] Pau Novella. Dogs analysis framework. Double Chooz Internal Document, DC-doc-1870-v1, September 2010.

[93] Claire Thomas. Generating radioactive decay. Double Chooz Internal Document, DC-doc-992-v1, August 2009.

[94] Glenn Horton-Smith. Double chooz geant4 summary talk for march 2012 dc paris analysis live meeting. Double Chooz Internal Document, DC-doc-3805-v1, March 2012.

[95] Kenneth S. Krane. *Introduction to Nuclear Physics*. John Wiley & Sons Inc., 1988.

[96] E. Browne, J. M. Dairiki, R. E. Doebler, et al. *Table of Isotopes*. John Wiley & Sons Inc., seventh edition edition, 1978.

[97] F. P. An et al. Observation of electron-antineutrino disappearance at daya bay. *Phys. Rev. Lett.*, 108:171803, Apr 2012.